Excavation of hard deposits and rocks

On the cutting of saturated rock

Helmons, Rudy

DOI
10.4233/uuid:7a46bca3-4105-4cdc-952d-a6d9fcfced76

Publication date
2017

Document Version
Final published version

Citation (APA)
Helmons, R. (2017). *Excavation of hard deposits and rocks: On the cutting of saturated rock*. [Dissertation (TU Delft), Delft University of Technology]. https://doi.org/10.4233/uuid:7a46bca3-4105-4cdc-952d-a6d9fcfced76

Excavation of Hard Deposits and Rocks

On the Cutting of Saturated Rock

Excavation of Hard Deposits and Rocks

On the Cutting of Saturated Rock

Proefschrift

ter verkrijging van de graad van doctor
aan de Technische Universiteit Delft,
op gezag van de Rector Magnificus prof. ir. K. C. A. M. Luyben,
voorzitter van het College voor Promoties,
in het openbaar te verdedigen op woensdag 10 mei 2017 om 10.00 uur

door

Rudolfus Lambertus Jacobus Helmons

werktuigbouwkundig ingenieur
geboren te Halsteren, Nederland.

Dit proefschrift is goedgekeurd door de promotor:

Prof. dr. ir. C. van Rhee

en copromotor:

Dr. ir. S. A. Miedema

Samenstelling promotiecommissie:

Rector Magnificus,	voorzitter
Prof. dr. ir. C. van Rhee,	Technische Universiteit Delft, promotor
Dr. ir. S. A. Miedema,	Technische Universiteit Delft, copromotor
Onafhankelijke leden:	
Prof. dr. ir. M. L. Kaminski	Technische Universiteit Delft
Prof. dr. ir. L.J. Sluys	Technische Universiteit Delft
Prof. dr. rer. nat. S. Luding	Universiteit Twente
Prof. dr. C. Drebenstedt	Technische Universität Bergakademie Freiberg
Prof. dr. E. M. Detournay,	University of Minnesota

The research presented in this thesis has been financed by Agentschap NL under grant agreement IMA1100007, together with Royal Dutch Shell, Royal Boskalis Westminster, Van Oord Dredging and Marine Contractors and Royal IHC.

Keywords: Rock mechanics, Discrete Element Method, Smoothed Particle, Rock cutting

Printed by: Ridderprint

Front & Back: Resultant outflow of a lava flow under water, located near the Axial Volcano (300 miles offshore from Washington state (USA). Credit: NSF-OOI/UW/CSSF

ISBN 978-94-6186-790-2

An electronic version of this dissertation is available at
http://repository.tudelft.nl/.
http://www.researchgate.net/profile/Rudy_Helmons.

To Corine
and the little boy

Summary

As a result of the worldwide population and welfare growth, the demand for energy (oil, gas and renewable sources) and raw materials increases. In the last decades, oil and gas are produced from more and more offshore sites and deeper waters. Besides energy, the demand for diverse metals and rare earth elements increases as well. These raw materials are often at the basis of new sustainable technologies e.g. permanent magnets for wind energy and battery packs for electric cars. The availability of these raw materials is essential for a stable development of the world economy. Unfortunately, for some of the crucial raw materials, the availability is sometimes very local and in various cases there is a monopoly forming. To reduce this economic risk, investments are needed to search and extract minerals from new locations. Large, metal-rich fields are found at the bottom of the sea, such as phosphate nodules, manganese nodules, cobalt-rich crusts and vulcanic sulphide deposits (often referred to as Seafloor Massive Sulphide, SMS). These deposits are mainly located in the deep sea, at depths ranging from several hundreds of meters to several kilometers.

One of the technical challenges to enable production from these locations is the cutting or excavation process. Experiments have shown that the energy needed to excavate the material increases with water depth. Besides that, it is demonstrated that rock that fails brittle in atmospheric conditions can fail more or less in a plastic fashion when present in a high pressure environment, as would be the case at large water depths. The goal of this research is to identify the physics of the cutting process and to develop this into a model in which the effect of hydrostatic and pore pressures is included.

The cutting of rock is initiated by pressing a tool into the rock. As a result, at the tip of the tool a high compressive pressure occurs, which leads to the formation of a crushed zone. Depending on the shape of the tool and the cutting depth, shear failures might emanate from the crushed zone, which will eventually expand as tensile fractures that can reach to the free rock surface. Through this process intact rock will be disintegrated to a granular medium. Additionally, the presence of water in the pores of and surrounding the rock influences the cutting process through drainage effects. The most relevant effects are weakening when compaction and hardening when dilation occurs in shearing and tension. Deformation of the rock causes the pore volume to change, resulting in a under or over pressure. As a result, the pore fluid needs to flow. The magnitude of the potential under pressure is limited through cavitation of the pore fluid, limiting further reduction of the pore pressure. The drainage effects cause the rock cutting process in a submerged environment to show a stronger dependency of both the hydrostatic pressure as well as the deformation rate.

The numerical simulations are performed with a 2D DEM (Discrete Element

Method). In DEM, the mechanical behavior of a rock is mimicked by gluing loose particles together with brittle bonds. Such a method shows strong resemblance with sedimentary rock. In order to include the effect of an ambient pressure as a result of the water depth and to include the presence of a fluid in the pores of the rock, a pore pressure diffusion equation is added to the model. The discontinuous results obtained with DEM are interpolated to a continuum field through the use of a SP-method (Smoothed Particles). Additionally, SP is used to solve the pore pressure diffusion equation. For that reason, the methodology used in this dissertation is referred to as DEM-SP.

Thus far no direct coupling has been found between the input microscopic parameters, that define the properties of and interactions between the particles in DEM, and the resulting bulk properties of the particle assembly. For that reason, a sensitivity analysis is performed in which the effect of the micro-properties on the macroscopic behavior is investigated. Additionally it is proven that the addition of the pore pressure diffusion process to the DEM-SP model corresponds with the effective stress theory. It is also proven that when air is used as a medium in the pores, no significant changes compared to simulations without pore pressure coupling occur. Comparison of the numerical model with a set of tri-axial experiments on shale, in which the deformation rate is varied, shows that the model is well capable to describe both compaction weakening and dilatant hardening.

In order to further validate DEM-SP, several experiments from literature are simulated. A comparison of 2D cutting experiments on tiles shows a good match for the chip size, chip shape and the required cutting force. DEM-SP is used to simulated drilling experiments on marble, in which the hydrostatic pressure is varied. These results show that the simulated behavior of the cutting process matches qualitatively with the experiments, i.e. the trend of increasing cutting force with increasing hydrostatic pressure. Furthermore a series of cutting experiments for the purpose of deep sea mining has been simulated. These results match both qualitatively and quantitatively. Additionally, both the experiments and simulations show the existence of a hyperbaric effect. This means that at a hydrostatic pressure which is significantly larger than the tensile strength of the rock the cutting process shear and cataclastic failure are more dominant, while at hydrostatic pressures significantly smaller than the tensile strength the cutting process is dominated by tensile failure and chipforming.

Finally, DEM-SP is used to simulate the full cutting motion of a pick point on a rotating cutterhead, in order to investigate the applicability of the method to shallow water depths (<30 m) and to investigate the use of the method for the dredging practice. Even at shallow water depths the effect of an increased hydrostatic pressure shows significant differences. Furthermore, the simulations show a transition from cataclastic towards ductile cutting process based on the cutting depth. Additionally a transition between stick-slip friction of the cut material along the tool is observed, which is an indication for different wear processes.

It is proven that DEM-SP is capable of solving drainage related effects in deformation of saturated rock. A range of rock cutting experiments are simulated and the results match well both qualitatively and quantitatively with respect to cutting

force and hydrostatic pressure. Further improvement of the model can be achieved by extending the model towards 3D.

Samenvatting

Door de wereldwijde bevolkings- en welvaartsgroei neemt de vraag naar energie (olie, gas en herwinbare bronnen) en grondstoffen toe. In de laatste decennia worden olie en gas steeds meer uit de kust en in steeds diepere wateren gewonnen. Naast energie is er ook een toename in de vraag naar diverse metalen en zeldzame aardelementen toegenomen. Deze grondstoffen liggen veelal aan de basis van de nieuwe duurzame technologiën zoals bijvoorbeeld permanent magneten voor windmolens en accu's voor elektrische auto's. De beschikbaarheid van deze grondstoffen is essentieel voor een stabiele ontwikkeling van de wereldeconomie. Helaas is de beschikbaarheid van enkele cruciale grondstoffen soms zeer lokaal en in een aantal gevallen is er sprake van monopolie vorming. Om dit economisch risico te beperken moet er ge investeerd worden in het vinden en ontginnen van nieuwe locaties. Op de zeebodem zijn grote metaalrijke velden gevonden van o.a. fosfaatknollen, mangaanknollen, kobaltrijke korsten en vulkanische sulfide afzettingen. Deze locaties bevinden zich voornamelijk in de diepzee, op dieptes van enkele honderden meters tot meerdere kilometers.

Een van de technische uitdagingen om winning uit deze gebieden mogelijk te maken is het snij- of ontgravingsproces. Experimenten hebben uitgewezen dat de benodigde energie om het materiaal te ontginnen toe neemt met de waterdiepte. Daarnaast is gebleken dat gesteente dat bros kapot gaat bij een atmosferische druk min of meer plastisch kan bezwijken bij een hoge omgevingsdruk, zoals het geval is op grote waterdiepte. Het doel van dit onderzoek is om de fysica van het snijproces in kaart te brengen en dit uit te werken tot een model waarin het effect van de hydrostatische druk wordt meegenomen.

Het snijden van gesteente wordt geïnitieerd doordat het gereedschap in de steen gedrukt wordt, waarbij aan de punt van het gereedschap een hoge drukspanning ontstaat, wat leidt tot het ontstaan van een vergruizingszone. Afhankelijk van de vorm van het gereedschap en de snedediepte kunnen vanuit de vergruizingszone afschuivingsbreuken ontstaan, welke naar het oppervlak uitgroeien als trekscheuren. Door middel van dit proces wordt een intacte steen opgebroken tot een granulair medium. Daarnaast be invloedt de aanwezigheid van water in de pori en van en rond het gesteente het verspaningsproces door drainage effecten. De voornaamste effecten hiervan zijn verzwakking door compactie en versteviging door dilatantie bij afschuiving en trek. Vervorming van het gesteente zorgt ervoor dat het volume van de pori en verandert, waardoor een onder- of bovendruk ontstaat. Het gevolg is dat de porievloeistof zal moeten toe- of afstromen. Het grootte van de eventuele onderdruk wordt beperkt door het caviteren van de porievloeistof, waardoor verdere afname van de poriedruk wordt tegengegaan. De drainage effecten zorgen ervoor dat het steensnijproces onder water een sterkere afhankelijkheid van zowel de hydrostatische druk als de vervormingssnelheid heeft.

De numerieke simulaties zijn uitgevoerd met een 2D DEM (discrete elementen

methode) model. Hierin wordt het gedrag van gesteente nagebootst door losse korrels met behulp van brosse bindingen aan elkaar te plakken, wat een sterke analogie heeft met sedimentair gesteente. Om het effect van een omgevingsdruk ten gevolge van de waterdiepte en om de aanwezigheid van een vloeistof in de pori en van het gesteente te simuleren is een poriedruk-diffusie vergelijking aan het model toegevoegd. De discontinue resultaten van DEM is met behulp van een SP-methode (smoothed particles, letterlijk vertaald gladgestreken deeltjes) geïnterpoleerd naar een continuumsveld. Tevens is SP gebruikt om de poriedruk-diffusievergelijking op te lossen. Vandaar dan ook dat naar deze methode wordt gerefereerd als DEM-SP.

Tot op heden is er nog geen directe koppeling gevonden tussen de op te geven micro-parameters voor de eigenschappen van en de interacties tussen de korrels in DEM en de daaruit resulterende eigenschappen van de korrels als bulk. Om die reden is een gevoeligheidsanalyse gemaakt van de invloed van de micro-eigenschappen op het macro-gedrag. Daarnaast is aangetoond dat het toevoegen van een poriedruk-diffusie proces aan het DEM-SP model overeenkomt met de theorie van effectieve spanning. Tevens is bewezen dat wanneer lucht als medium in de pori en gebruikt wordt dit geen significante verschillen oplevert ten opzichte van simulaties zonder poriedruk-koppeling. Vergelijking van het numerieke model met een serie tri-axiaal proeven op schaliegesteente, waarbij de vervormingssnelheid sterk is gevarieerd laat zien dat het model goed in staat is om compactie verzwakking dilatantie versteviging te beschrijven.

Om DEM-SP te valideren zijn diverse experimenten uit literatuur nagerekend. Vergelijking van 2D snijproeven op tegels laten zien dat zowel de brokvorm, brokgrootte als de benodigde snijkracht overeen komen. Daarnaast is DEM-SP gebruikt om experimenten van het boorproces in marmer waarbij hydrostatische druk is gevarieerd te simuleren. Deze resultaten laten zien dat kwalitatief het gesimuleerde gedrag overeenkomt met de experimenten, de trend van de benodigde snijkracht t.o.v. de hydrostatische druk komt overeen. Tevens is er een serie snijproeven ten behoeve van diepzeemijnbouw, waarbij zowel de hydrostatische druk als de snijsnelheid zijn gevarieerd, gesimuleerd. Zowel kwalitatief als kwantitatief komen de resultaten overeen. Verder illustreren zowel de experimenten als de simulaties het bestaan van een hyperbaar effect. Hiermee wordt bedoeld dat bij een hydrostatische druk die significant groter is dan de treksterkte van het gesteente het snijproces wordt gedomineerd door afschuiving en vergruizing, terwijl voor hydrostatische drukken significant lager dan de treksterkte het snijproces gedomineerd wordt door falen op trek en brokvorming.

Tot slot is DEM-SP gebruikt om de volledige snijbeweging van een tand op een roterende cutterkop te simuleren en om de toepassing van de methode voor ondiepe wateren (<30 m) te onderzoeken. Ook op deze kleine waterdiepten is het effect van een verhoogde hydrostatische druk significant aanwezig. Verder tonen de simulaties een transitie van een cataclastisch naar een bros snijproces op basis van de snedediepte. Tevens is er een overgang tussen kleef-slip wrijving van het gesneden materiaal langs de beitel waargenomen, wat een indicatie geeft voor mogelijke slijtage.

Het is aangetoond dat DEM-SP in staat is om drainage gerelateerde effecten in

verzadigd gesteente op te lossen. Een scala aan rots snijproeven zijn gesimuleerd en de resultaten komen zowel kwalitatief als kwantitatief met de snijkrachten en hydrostatische druk overeen. Verdere verbetering van het model is mogelijk door het model uit te breiden naar 3D.

Contents

List of Symbols

Roman symbol	Description	Unit
A	Fictional parameter	[-]
a	Surface area	[m^2]
C_f	Rock fabric compressibility	[Pa^{-1}]
C_l	Liquid compressibility	[Pa^{-1}]
C_p	Pore fluid compressibility	[Pa^{-1}]
C_s	Compressibility of solid	[Pa^{-1}]
C_0	Constant depending on particle packing	[-]
c	Cohesion	[Pa]
$c_{1,2,...}$	Constant	[-]
D	(hydraulic) Diffusion coefficient	[m^2/s]
D	Damage parameter	[-]
d	Specimen diameter	[m]
E	Young's modulus	[Pa]
E_{sp}	Specific energy	[Pa]
E_0	Effective Young's modulus of pack of grains	[GPa]
E_{tot}	Total Energy	[J]
$\mathbf{F}$	Force	[N]
F_c	Cutting force	[N]
F_h	Horizontal component of cutting force	[N]
F_n	Normal force	[N]
F_s	Shear force	[N]
F_v	Vertical component of cutting force	[N]
f_s	Sampling frequency	[Hz]
g	Crack extension force	[N]
G	Mechanical energy release rate	[N]
h	Smoothing length	[m]
h_{tool}	Height of tool	[m]
I	Moment of inertia	[kgm^2]
$_i$	Particle index	[-]
$_j$	Neighoring particle index	[-]
K_f	Bulk modulus of fluid	[Pa]
K_{hyd}	Hydraulic conductivity	[m/s]
K_m	Bulk modulus of rock matrix	[Pa]
K_s	Bulk modulus of solids	[Pa]
K_{Ic}	Fracture toughness	[Pa]
K_1	Grain force on shear plane	[N]

Roman symbol	Description	Unit
K_2	Grain force on tool surface	[N]
k_n	Normal stiffness	[N/m^2]
k_s	Shear stiffness	[N/m^2]
l	Length	[m]
m	Particle mass	[kg]
m	Strength ratio	[-]
N	Deborah number	[-]
N_{cr}	Critical Deborah number	[-]
n	Porosity	[-]
$\mathbf{n}$	Normal vector	[-]
n_c	Number of contacting neighbors	[-]
p	Pressure	[Pa]
p_h	Hydrostatic pressure	[Pa]
p_i	Initial pore pressure	[Pa]
P_c	Cutting power	[W]
p_{undr}	Undrained pore pressure	[Pa]
Q_c	Cutting production	[m^3]
Q_r	Relieved cutting production	[m^3]
Q_u	Unrelieved cutting production	[m^3]
$\mathbf{q}$	Fluid flux	[m/s]
R	Dimensionless distance (SP)	[-]
R_0	Surface tension force	[N]
$\bar{r}$	Mean particle radius	[m]
r_{max}	Maximum particle radius	[m]
r_{min}	Minimum particle radius	[m]
S_i	Initial saturation degree	[-]
s	Specific storage capacity	[-]
s_t	Tool spacing	[m]
T	Torque	[Nm]
T_n	Normal bond strength	[N/m]
T_s	Shear bond strength	[N/m]
t	Time	[s]
$\vec{t}$	Tangential vector	[-]
t_c	Cutting depth	[m]
t_{def}	Characteristic time of deformation	[s]
t_{hd}	Characteristic time of hydraulic diffusion	[s]
t_{sim}	Simulated timespan	[s]
U_a	Surface energy	[J]
U_e	External energy	[J]
U_i	Internal energy	[J]
$\mathbf{u}$	Position vector	[m]
$\dot{\mathbf{u}}$	Velocity vector	[m/s]
$\ddot{\mathbf{u}}$	Acceleration vector	[m/s^2]
u	Unknown parameter	[-]

Roman symbol	Description	Unit
v	Gas fraction adsorbed by solids	[-]
v_c	Cutting velocity	[m/s]
W	Kernel function	[-]
W_1	Force resulting from pore under pressure on shear plane	[N]
W_2	Force resulting from pore under pressure on tool surface	[N]
w	Tool width	[m]
z	Water depth	[m]

Greek symbol	Description	Unit
α	Rake angle with respect to vertical	[°]
α_d	Numerical damping coefficient	[-]
α_{es}	Effective stress coefficient	[-]
β	Shear angle	[°]
δ	External friction angle	[°]
ϵ	Strain	[-]
$\dot{\epsilon}$	Strain rate	[1/s]
ϵ	Strain	[-]
$\dot{\epsilon}$	Strain rate	[s^{-1}]
$\dot{\epsilon}_{cr}$	Critical strain rate	[s^{-1}]
ϵ_V	Volumetric strain	[-]
ϵ_f	Strain to failure	[-]
ζ	Fluid content	[-]
η	Dynamic viscosity	[Pas]
κ	Intrinsic permeability	[m^2]
κ_0	Intrinsic permeability at zero effective stress	[m^2]
λ	Stress distribution factor	[-]
μ	Coulomb friction (grain-grain)	[-]
μ_{tg}	Coulomb friction (tool-grain)	[-]
ν	Poisson's ratio	[-]
ξ_{Pe}	Pore Peclet number	[-]
ρ	Density	[kg/m^3]
σ	Stress	[Pa]
σ_{BTS}	Tensile strength, determined as Brazilian disc	[Pa]
σ_c	Compressive strength	[Pa]
σ_{cd}	Compressive strength of specimen with diameter d	[Pa]
σ_{c50}	Compressive strength of specimen with diameter of 50 mm	[Pa]
σ_t	Tensile strength	[Pa]
σ_{UCS}	Unconfined compressive strength	[Pa]

Greek symbol	Description	Unit
σ_{UTS}	Unconfined tensile strength	[Pa]
$\sigma_{1,2,3}$	Principal stresses	[Pa]
σ'	Effective stress	[Pa]
τ_s	Shear strength	[Pa]
τ_0	Yield stress in shear	[Pa]
Φ_s	Particle sphericity	[-]
ϕ	Internal friction angle	[°]
ω	Angular velocity	[rad/s]
θ	Half top angle of tool	[°]

Abbreviation	Description
AE	Acoustic Emissions
BTS	Brazilian Tensile Strength
CRM	Critical Raw Material
CSD	Cutter Suction Dredge
DEM	Discrete Element Method
DEM-SP	Discrete Element Method-Smoothed Particle
DSM	Deep Sea Mining
EXHADERO	Excavation of Hard Deposits and Rocks
IDM	Inhomogeneous Deformations on Micro-scale
LCM	Liner Cutting Machine
PDC	Polycrystalline Diamond Compact
RQD	Rock Quality Designation
SP	Smoothed Particle
SPH	Smoothed Particle Hydrodynamics
TBM	Tunnel Boring Machine
UCS	Unconfined Compressive Strength

1

Introduction

"There are no such things as applied sciences, only applications of science."

Louis Pasteur

This chapter gives an introduction to deep sea mining and its technological challenges, one of them being the excavation process of rock like materials from the sea bed. The work in this thesis also considers rock cutting applications for drilling and dredging (shallow water). Development of a modeling approach to simulate the rock cutting process of a single tool is the main topic of this dissertation.

1

1.1. Background

Currently, the demands for raw materials increase. It is expected that these demands continue to increase in the near future. This expectation is based on several trends on a global scale.

The world population keeps growing. At the end of the year 2015, the world population already consists of more than seven billion people. Prospects of the United Nations on the world population show that it is expected that the world population will increase to nine billion people within the next 30 years (Population Division of the Department of Economic and Social Affairs of the United Nations Secretariat, 2015) . Together with the growth of the population, the demand for food will increase as well. Artificial fertilizers become almost a necessity to obtain a sufficient food supply. These fertilizers are based on phosphorous material, which is extracted from terrestrial mines. However, with the growing world population, the current production rate will not suffice.

Another trend is that developing countries get more and more developed in economical terms. Due to their development their demand for energy (mostly fossil fuels) and raw materials increases. While developed countries are trying to become less dependent on fossil fuels for their energy supplies, it is expected that the demand for fossil fuels will not decline in the near future.

The development and production of new technologies such as wind turbines, computers, televisions, mobile devices, solar cells and electric cars requires large amounts of energy and raw materials, including rare earth elements. Currently these are extracted from terrestrial mines. Production from these mines may not suffice in the future.

The European Commission has created a list of critical raw materials (CRMs). CRMs are defined as those materials that combine a high economic importance to the EU and a high risk associated in their supply assurance (EU Commission, 2015). The supply risk is based on indicators like accountability, political stability, government effectiveness and regulatory quality. In figure 1.1 an overview of the main CRMs suppliers. Special notice is made on the resources located in China, which might be of a significant influence on the development of the world economy and geo-political relations. Especially because for several types of raw materials China has (almost) a monopoly position, especially for antimony, magnesium, rare earth elements and tungsten. Besides that, some of the locations are situated in political unstable regions (e.g. cobalt in central Africa).

In order to reduce the dependence on the supply of raw materials by these countries, other deposits and means of producing the raw materials are needed. Recycling can help to supply in the demand of the raw materials needed. However, it is expected that recycling will is not sufficient, and other mining locations are needed to meet the demand. Besides mining sites on land, asteroid mining and deep sea mining are considered an option.

In the deep sea, various types of metal rich deposits have been found, e.g. phosphorous nodules, manganese nodules, volcanic sulphide deposits, metal-rich crusts. Most of these deposits are found on the seafloor of the Pacific and Indian ocean. These deposits are especially interesting of because they contain many of the mate-

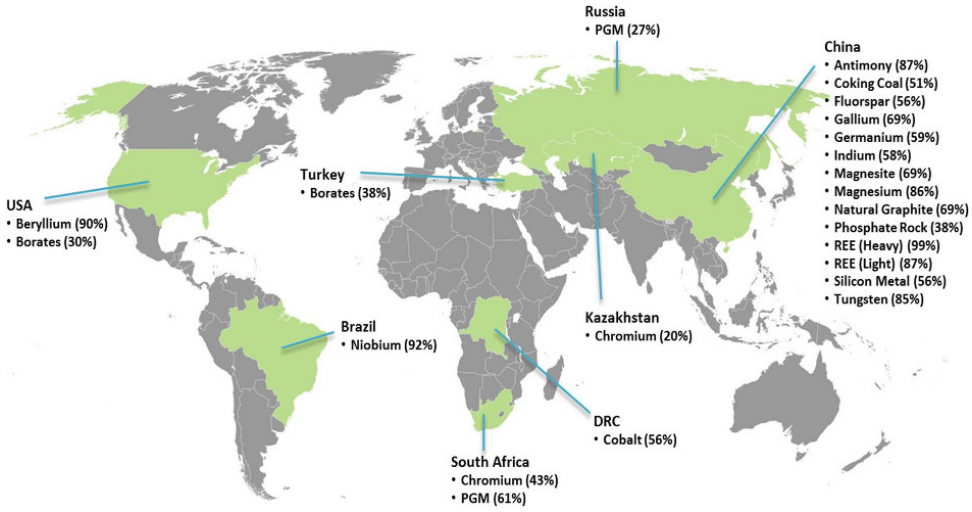

Figure 1.1: Overview of highest production per country on critical raw materials, taken from EU Commission (2015)

rials that are needed for development of the newer technologies, like for use in battery packs, permanent magnets, etc. Table 1.1 gives an overview of the prospected resources of the Prime Crust Zone, an area of metal-rich crust in the Pacific of approximately the size of the United States. A remark has to be made, the total bulk of materials prospected in the Prime Crust Zone is the total amount of material expected to be found in that area, not necessarily being economically viable.

In this context, the perspective of deep sea mining is being considered. Besides the environmental impact that deep sea mining can have, several technological challenges still have to be solved or are investigated. First of all, the material needs to be excavated, which is investigated in this thesis. At large water depths, the hydrostatic pressure can be of substantial influence on the excavation process, (Zijsling, 1987). This is especially the case for rock-like materials. It is expected that rock that fails in a brittle fashion at ambient pressure, might fail in a more ductile way in a high pressure environment. Besides the change in failure mode, it is expected that the cutting forces increase with increasing hydrostatic pressure as well. To what extent this change in behavior occurs and what the implications will be is not yet fully understood.

Furthermore, the excavated material needs to be transported to the surface, where it can be further processed. Various ideas exist on how to transport the materials, one of these ideas is investigated at our group of dredging engineering, i.e. vertical hydraulic transport through a riser with a series of booster stations based on centrifugal pumps (van Wijk, 2016). In vertical hydraulic transport, approximately 80% of the pumped volume will be water. In order to lower the environmental impact of an offshore mining operation, it is required that the water that acts as carrier fluid in the vertical transport system has to be deposited near the seabed

Table 1.1: Estimated metal contents in cobalt crust compared with global land-based reserves and resources, after World Ocean Review (2014). Metal contents in millions of tonnes

Elements	Cobalt crusts in the Prime Crust Zone (PCZ)	Global reserves on land (economically minable deposits today)	global reserves and resources (including subeconomic deposits)
Manganese (Mn)	1714	630	5200
Titanium (Ti)	88	414	899
Rare earth oxides	16	110	150
Nickel (Ni)	32	80	150
Vanadium (V)	4.8	14	38
Cobalt (Co)	50	7.5	13
Tungsten (W)	0.67	3.1	6.3
Niobium (Nb)	0.4	3	3
Arsenic (As)	2.9	1	1.6
Bismuth (Bi)	0.32	0.3	0.7
Yttrium (Y)	1.7	0.5	0.5
Platinum group	0.004	0.07	0.08
Tellurium (Te)	0.45	0.02	0.05
Thallium (Tl)	1.2	0.0004	0.0007

in the vicinity of the mining operation. Besides filtration, no other treatments are carried out on the seawater before it is returned to the seafloor. Fine sediments remain in the water and during deposition of the return flow, sediment plumes can occur that can travel for over tens of kilometers. Such a plume may be harmful for the ecosystems in the region of a mining site. Near and far-field models will be developed to allow for assessment of the environmental impact of such a mining operation (Ortega, 2014; de Wit, 2015; van Grunsven et al., 2016).

The cutting of saturated rock is of interest in several fields of industry. Some examples are addressed:

Example 1: Deep Sea Mining

Several of the mineral rich deposits in the deep sea, such as Seafloor Massive Sulfide (SMS) deposits and ferro-manganese (Fe-Mn) crusts require rock cutting equipment to retrieve the materials contained in these structures. SMS deposits are typically located in water depths greater than 1 km and are in close proximity to tectonic plate boundaries and submarine volcanic activities, e.g. the Solwara 1 SMS deposit is located at a water depth of 1600 meter. Fe-Mn crusts form at water depths of about 400-7000 m, with the thickest and most metal-rich crusts occurring at depths of about 800-2500 m (World Ocean Review, 2014). There is limited data about the mechanical properties of the crusts and the deposits. The typical range of mechanical properties that have been found are presented in tables 1.2 and 1.3.

Table 1.2: Range of mechanical properties in SMS deposits, after Yamazaki and Park (2003).

Parameter	Min	Max
Wet bulk density [kg/m^3]	$2.4 \cdot 10^3$	$4.0 \cdot 10^3$
Solid density [kg/m^3]	$3.6 \cdot 10^3$	$5.5 \cdot 10^3$
Porosity [-]	0.15	0.53
Unconfined compressive strength [MPa]	3.1	38
Tensile strength [MPa]	0.14	5.2
Typical water depths [m]	> 1000	

Table 1.3: Range of mechanical properties in Fe-Mn crusts, after Chung (1996)

Parameter	Min	Max
Wet bulk density [kg/m^3]	$1.65 \cdot 10^3$	$2.17 \cdot 10^3$
Porosity [-]	0.43	0.74
Unconfined compressive strength [MPa]	0.5	16.8
Tensile strength [MPa]	0.1	2.3
Shear strength [MPa]	1.7	2.5
Typical water depths [m]	400	7000

In 2005 Nautilus Minerals Inc. started exploring the SMS deposits in the Exclusive Economic Zone of Papua New Guinea. In 2010 several drilling trials in the Solwara 1 project in Papua New guinea showed the presence of high graded copper deposits. For the excavation of the SMS deposit, Nautilus designed to use three Remotely Operated Vehicles. An auxiliary cutter will be used deal with rough terrain and creates benches for the other machines to work on. The bulk cutter is designed to have a higher cutting capacity, but is limited to working on benches. Both machines will leave the cut material on the seafloor, which will be later collected by the collecting machine that is connected to the vertical transport system. Due to the relatively high hydrostatic pressure (with respect to the tensile strength of the rock), tensile failure of the rock is less likely to occur and it is expected that shear failure of the chips will be the dominating failure mechanism. Mining at the Solwara 1 project site is expected to start within a couple of years from 2016. Various companies have comparable design concepts for deep sea mining operations, e.g. Royal IHC, Bauer, Soil Machine Dynamics. An impression of the concept design of Royal IHC is presented in figure 1.2.

Example 2: Dredging

Whether it is for the construction of new ports or the deepening of canals, in dredging often densely compacted sand, clay or rock have to be excavated. For these kind of excavation projects, often a Cutter Suction Dredge (CSD) is used. The CSD is a stationary dredger equipped with a cutter device, most often a crown cutter, which excavates the soil before it is sucked up by the flow of the dredge pumps. While operating, the dredger moves around a spud pole by pulling and slacking of the two

Figure 1.2: Preliminary designs of deep sea mining vehicles, courtesy of Royal IHC

side wires. The cutter head is installed at the end of the ladder, which is used to position the cutter head.

CSD's are typically used in water depths up to 30 m and have installed cutter powers of 50 kW up to 8.5 MW. Most of the dredging works deal with rocks with compressive strength up to 20 MPa where rock cutting is economically the most preferable method of excavation. Tougher rocks, with a UCS of 60 - 80 MPa, can be excavated with a CSD if blasting is not an option because of its environmental impact. An example of a CSD is presented in figure 1.3a and an impression of a crown cutter head is shown in figure 1.3b. When excavating rock with a CSD cutterhead, the rock cutting process is dominated by brittle failure and chips are generated by brittle shear and tensile failures. One of the market trends is that the CSD's will be used more and more on tougher types of rock.

(a) Cutter Suction Dredger Athena

(b) Cutterhead for cutter suction dredges, IHC lightduty rock

Figure 1.3: Cutter suction dredge equipment.

Example 3: Drilling

In petroleum well drilling, the polycrystalline diamond compact (PDC) bits have become one of the most common drilling tools. PDC-bits are composed by multiple cutters that are positioned on fixed blades, see figure 1.4 for an example. The bits are positioned at a negative rake angle, meaning that the bit 'drags' through the

rock. Due to the design of the bit, the small cutting depth (up to a few millimeters) and the high hydrostatic pressure that is applied, PDC drilling works by shearing the formation.

The typical rock properties with respect to drilling almost cover the whole range of rocks that can be found, with UCS values ranging up to 200 MPa. The drilling process often takes place in high pressure conditions (> 10 MPa). Special interest is shown towards the drilling process of low permeable rocks (e.g. shale) at great depths (Zijsling, 1987). Besides that, the drilling industry is interested in the application of fluid flow with other fluids than water (e.g. non-Newtonian, drilling fluid) through the pores of the rock considered.

Figure 1.4: Drill head with PDC bit inserts

1.2. Research objective

In engineering practice very often the information obtained from the field about what kind of rock has to be cut is very limited. It is quite common that both the number of samples as well as the number of measured rock parameters is very limited. It happens quite often that only the UCS value and the type of rock are known, all other parameters might have to be estimated based on empiricism (Zijsling, 2013).

In the industries, many questions about the cutting process of saturated rock-like materials still remain. Especially on how to optimize and develop (new) excavation and drilling equipment and how to predict the cutting forces. A proper understanding of the behavior of saturated rock, the failure mechanisms and their interactions is essential to answer these questions.

The main objectives of this PhD-study are:

- To describe the physical phenomena that occur during the cutting of saturated rock, with an emphasis on the fluid pressure effects.
- To develop a physical and implement a mathematical model to predict the rock cutting process, in which the hydrostatic and pore pressure effects are incorporated.

The wide range of applications with respect to rock properties, ambient conditions and tool design, more or less implies the need for a generic modeling approach. For that reason, the emphasis of the model is on an approach that will be generally applicable towards the cutting of saturated rock, independent of the type of rock and tool that are considered.

To meet the objectives, several steps are defined:

- **Step 1**: Identification of the significant physical phenomena and parameters for the cutting of saturated rock
- **Step 2**: Setup of physical and mathematical model to simulate the rock cutting process. Furthermore, the numerical implementation of the models needs to be verified
- **Step 3**: The developed model has to be validated. Validation cases and test cases are simulated for various tool-rock interactions, e.g. tile cutting, drilling, seabed mining and dredging.

1.3. Outline of this thesis

In chapter 2 the different processes influencing the behavior of saturated rock are introduced. How these processes work together and affect the rock cutting process is elaborated upon in chapter 3. The state of the art of rock cutting models is discussed in this chapter as well.

Chapter 4 elaborates on the modeling approach, setup and implementation of the physical model in a mathematical model. The methodology is tested for several numerical cases to prove that the mathematics of the model are calculated correctly. In chapter 5 validation cases for the methodology with respect to material tests of the saturated rock are presented. Validation and test cases of the methodology with respect to tool-rock interactions are investigated in chapter 6.

Each chapter contains conclusions and recommendations concerning that specific topic. The overall conclusions and recommendations are presented in chapter 7. These are subdivided in the topics saturated rock, rock cutting models and the numerical modeling approach developed within this project.

2

Physics of Rock in Relation to Rock Cutting Process

"The first step to be taken, is to study carefully the fundamental phenomena above described, and to examine all the various circumstances under which they present themselves."

Jean-Baptiste Biot

The different processes influencing the mechanics, deformation and failure of rocks are introduced and some characteristic properties of deformation and failure of saturated rock are discussed. In this chapter the emphasis is on the phenomena and effects that are related to (saturated) rock mechanics. First the most common characteristics of properties that are of interest to the cutting of dry rock. This is followed by an overview on how the presence of a pore fluid can influence the mechanical response of the rock. Tool-rock interactions will be treated in chapter 3.

2.1. Introduction

In all rock cutting processes, the material response of rock is essential. The presence of a pore fluid can significantly affect the mechanical response of the rock. How the mechanical behavior can be affected by a fluid is analyzed in detail in this chapter. To start with, some basic definitions are given and a brief overview of the type of rocks that are of special interest within the industrial practice is presented. This is followed by an overview of the mechanical response of dry rock, with an emphasis on the most relevant aspects of the mechanical behavior of the rock with respect to the cutting process. Thereafter the influence of a pore fluid on the mechanical behavior of a rock is analyzed. Although the main focus of this research is on fluid saturated rock, most of the research carried out in the field of rock cutting concerns dry rock. A pore fluid can affect the mechanical behavior of a rock through physico-chemical effects (independent of time scale) and through hydro-mechanical effects (dependent on time scale of experiments). First an overview of the physico-chemical effects is presented to show what changes can occur when comparing dry and saturated rock samples. This will be followed by an analysis on which hydro-mechanical coupling effects can have a significant influence on the rock deformation process.

The topic of this dissertation covers several fields of research and engineering, each with their own sign conventions. To avoid confusion, the following sign conventions are used throughout this dissertation.

- Compressive direction is positive, tensile direction is negative.
- Vectors are denoted in bold face, e.g. $\mathbf{F} = m\ddot{\mathbf{u}}$.

There are three general types of rocks, igneous, metamorphic and sedimentary. Although all types of rocks can be found in abundance, sedimentary rock is the most common kind within the drilling, dredging and seabed mining industries that are considered in this dissertation. In several cases in this dissertation the data presented in the references does not provide sufficient information, the estimations for these missing material properties are based on empirical data and rules of thumb, these are presented in appendix A.

As stated in the research objective, see section 1.2, there is a need to investigate the rock cutting process in general. Due to the fact that the industries have to deal with a wide range of rocks and detailed rock properties often lack in practice, emphasis is put on modeling the rock cutting process for a generic type of rock. For that reason, the work presented in this chapter is restricted to the most relevant physical phenomena and trends observed in literature.

2.2. Rock Failure Mechanics

2.2.1. Failure modes

At the micro-scale, several failure mechanisms can be distinguished in practical rock mechanics tests (e.g. uni-axial compression, tri-axial compression, Brazilian splitting tests):

- Tensile failure (brittle).

- Shear failure (brittle).
- Compressive failure (ductile).

Which failure mechanism will occur depends on the rock properties and the stress conditions applied on the specimen. The strength ratio m is often used to distinguish the dominant failure mechanisms in a rock. The strength ratio is defined as

$$m = \frac{\sigma_{UCS}}{\sigma_{UTS}} \tag{2.1}$$

with uni-axial compressive and uni-axial tensile strength, respectively σ_{UCS} and σ_{BTS}. Low values of the strength ratio are typical for 'ductile' rock types (e.g. shale ($m = 6 \pm 2$), chalk ($m = 7 \pm 2$), gypsum ($m = 8 \pm 2$)), high values are typical for brittle rock types (e.g. granite ($m = 32 \pm 3$), quartzite ($m = 20 \pm 3$)). The values of m are presented here are from Hoek and Brown (1997), for an overview of more typical values for m, see appendix A.

An overview of the macro-scale failure modes that occur with changes in confining stress is presented in figure 2.1. Tensile failure is associated with the separation of grains. It can also occur as axial splitting, which can occur in uni-axial compressive tests and tri-axial compressive tests with low confining stresses for rock specimens with a high strength ratio. In this failure mode the specimen splits along the axis of the highest principle stress. Specimens with low strength ratios will not fail in axial splitting or even in tensile failure at zero confining stress. At higher confining stresses, the sample will fail along a shear plane. Further increase of the confining stress can result in shear bands. At sufficiently high confinement, the sample will fail in a compressive ductile fashion. In the extreme case this results in barreling of the specimen. This failure mode is especially of interest to high porous rocks, where the porous structure of the rock collapses as a result of high mean stress, resulting in densification of the rock.

2.2.2. Brittle Failure Modes

There are three modes of brittle deformation that can occur in a three-dimensional body, (Lawn, 1993). These modes are shown in figure 2.2. In tensile fracturing (mode I), the fracture surfaces open with respect to each other after fracturing has taken place. The energy needed for creation of the surface is provided by tensile strain energy. In the shearing mode (mode II), the fracture acts along the fracture surface and parallel to the propagation direction of the fracture. The energy required for the fracture to propagate is provided by shear strain relative to the fracture plane ate the tip. The tearing mode (mode III) also acts along the fracture surface, but perpendicular to the propagation direction of the fracture. This is due to a torsional component applied to the fracture front. In fracture mechanics, often combinations of these three modes occur. Rock cutting processes, dependent on the conditions, are dominated by failure modes I and II, as far as brittle failures are concerned.

Linear Fracture Mechanics

Linear elastic fracture mechanics (LEFM) help to interpret the opening and propagation of fractures in a linear elastic continuum.

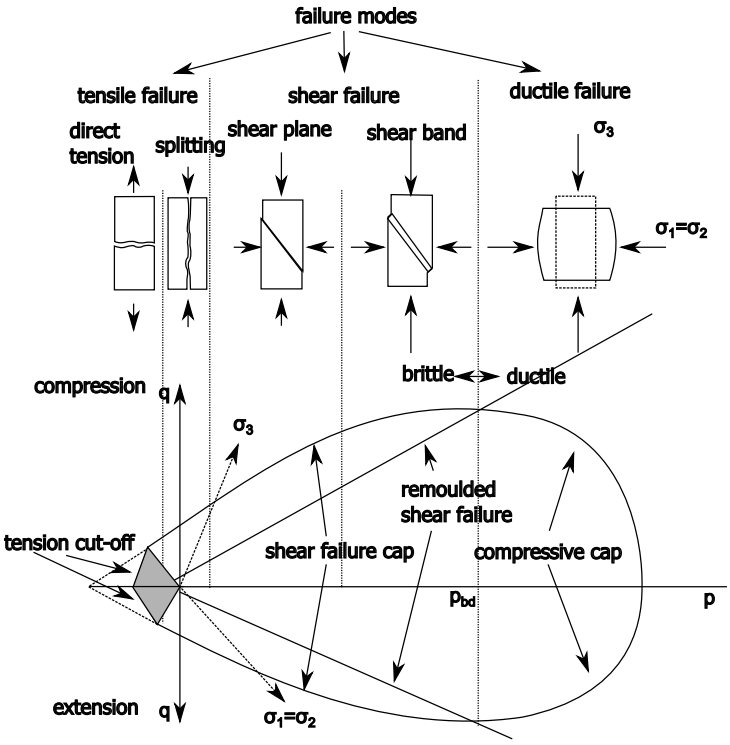

Figure 2.1: Overview of the range of deformation modes for rock with increasing confining stress, after Winterwerp and van Kesteren (2004).

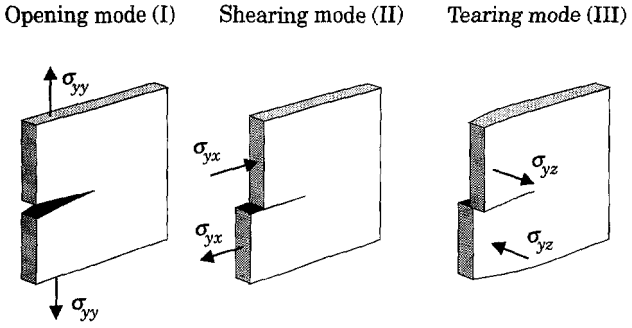

Figure 2.2: Definition of the deformation modes.

The first law of thermodynamics can be used to determine whether a crack will propagate. In order for a crack to propagate, the total amount of mechanical energy that is supplied to a material volume per unit of time must be transferred into internal energy, surface energy, dissipated energy and kinetic energy. Internal

energy is the stored energy. The surface energy changes when a new free surface is generated (i.e. when a crack propagates). The kinetic energy is the result of material velocity. The dissipation may occur in various ways, but is mostly due to friction and plastic deformation, which results in temperature changes. According to Griffith (1921), the propagation of a crack is determined by the transfer of internal and external energy into surface energy, as in

$$\frac{dU_e}{da} - \frac{dU_i}{da} = \frac{dU_a}{da} \tag{2.2}$$

with external energy U_e, internal energy U_i, surface energy U_a and change in surface da. The propagation of a crack is then determined by

$$\begin{aligned} \frac{dU_e}{da} - \frac{dU_i}{da} < \frac{dU_a}{da} \quad &\rightarrow \quad \text{no crack growth} \\ \frac{dU_e}{da} - \frac{dU_i}{da} > \frac{dU_a}{da} \quad &\rightarrow \quad \text{unstable crack growth} \\ \frac{dU_e}{da} - \frac{dU_i}{da} = \frac{dU_a}{da} \quad &\rightarrow \quad \text{critical crack length} \end{aligned} \tag{2.3}$$

An unstable crack growth corresponds to a brittle macroscopic failure. Like in many physical processes, the total free energy of a system will be maximized. Based on this, the direction of propagation of a crack is favored in the orientation that maximizes the decrease in total system free energy. In an isotropic system this corresponds with seeking a maximum of the mechanical energy release rate G. In other words, the crack-extension force $g = G - R_0$ is maximized, (Lawn, 1993, p.45) with surface tension force R_0. However, Lawn also mentions that the entire propagation history of a crack is predestined by the existing stress state before fracture has even begun.

2.2.3. Brittle-Ductile Transition

There is a large variety of the potential deformation mechanisms in the ductile field, and thus for the brittle-ductile transition as well. The nature of brittle-ductile transitions at relatively low temperatures (as is the case for rock cutting), two extreme cases of ductile deformation mechanisms are considered, purely cataclastic and purely crystal plastic. Although the purely cataclastic ductile behavior is most likely to occur in rock cutting processes, purely crystal plastic ductile behavior has been observed in drilling experiments as well (Zijsling, 2013).

According to Paterson and Wong (2005), the brittle-ductile transition in case of cataclastic failure can be explained by a lower stress dependency of the fracture stress with respect to the frictional sliding stress. The cross-over of these two stress trends is where the brittle ductile transition occurs, as depicted in figure 2.4a. However, this transition is based on a macroscopic observation, on a microscopic scale, the following occurs. With increasing confining stress not only the growth of micro-cracks becomes more difficult, the growth of the cracks at high confining stresses tends to be more stabilized. This eventually leads to fragmentation or disintegration

of the specimen by a rapid increase in the number of stable micro-cracks, resulting in a cataclastic failure mode. Francois and Wilshaw (1964) explained, based on dislocation models for the nucleation of cracks, that because the additional stress from a confining stress is small compared to the local stresses near the dislocations, the stress for microfracture initiation will be nearly independent of the confining stress while crack propagation depends on the confining stress.

The cataclasis can mainly result in two different types (Paterson and Wong, 2005). In compact rock and strongly cohesive rock, stabilization of the micro-cracks leads to the occurrence of more micro-cracks as the loading increases, eventually leading to the coalescence of the cracks, resulting in the breaking down of the rock into a granular mass. In weakly cohesive porous rock, cataclasis is more a result of grain crushing, (Zhang et al., 1990; Wong et al., 2004).

Deformation by crystal plasticity occurs when an increase of the confining stress on a specimen raises the brittle fracture strength to a level that exceeds the yield stress for crystal plastic flow, see figure 2.4b. Depending on the type of rock, it will be possible that before the crystal plastic flow occurs, first a cataclastic flow regime exists (Wong et al., 2004).

2.2.4. Ductile failure mode (cataclasis)

The macroscopic compressive failure of rocks can be caused by three different types of failure at the micro-scale (van Kesteren, 1995), especially for sedimentary rock:

- Failure of the bonds between particles
- Failure of the particles (often referred to as particle crushing)
- Failure of the skeleton (often referred to as pore collapse)

All three failure mechanisms have a similar effect, i.e. they increase the mobility of particles within the rock fabric. Based on the Inhomogeneous Deformations on Micro-scale (IDM) theory (van Kesteren, 1995) it follows that this mobility on micro-scale is obtained through heterogeneous shear deformation between particles (i.e. sliding and/or rolling of particles) in order to allow for homogeneous isotropic plastic deformation on the macro-scale. A visual representation is presented in figure 2.3. For that reason, quasi-ductile behavior requires mobility of (components within) the rock skeleton to allow the plastic shear strain within the skeleton. In general, this mobility is created by failure of the bonds between grains or failure of the grains themselves.

2.2.5. Post-failure

The brittle-ductile transition can also be observed with respect to the post-failure behavior of a rock specimen. The maximum stress before failure increases with increasing confining stress and the amount of strain softening decreases. At low confining stresses, when approaching the peak strength, strain softening will occur weakening the specimen with increasing strain. Further strain will tend to be inhomogeneous and it concentrates in the weaker elements of the rock that have already

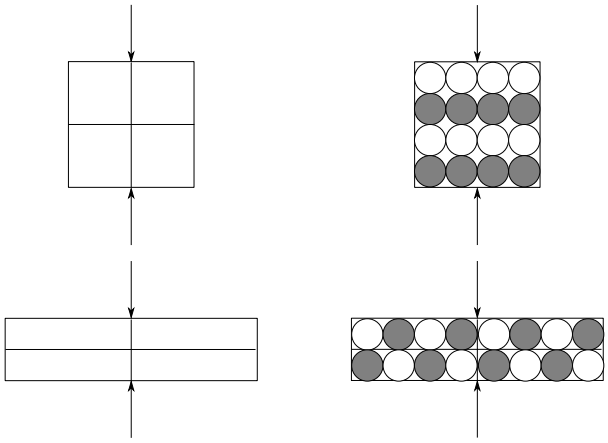

(a) Continuum based (b) Particle based

Figure 2.3: Homogeneous deformation paradox, based on Winterwerp and van Kesteren (2004).

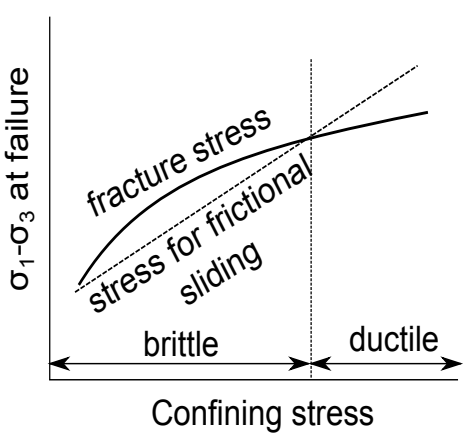

(a) Transition to cataclastic flow.

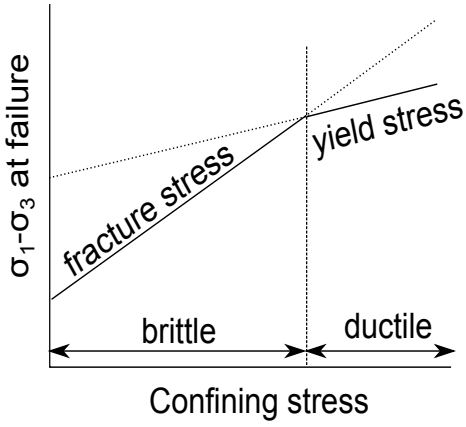

(b) Transition to plastic flow, through crystal plasticity.

Figure 2.4: Simple models for the brittle-ductile transition, after Paterson and Wong (2005).

been subjected to the largest amount of strain. Following peak stress, these zones of concentrated strain or shear planes develop as large cracks throughout the specimen.

In the case of strain-hardening deformation, specimens of rock become stronger as they deform. As a consequence, the strain tends towards homogeneity throughout the confined specimen, since those elements of the rock which have strained most will be stronger than those that have strained less, (Farmer, 1983, p.85). See figure 2.5 for an illustration of the effects with respect to an increase in confining pressure.

Wawersik and Fairhurst (1970) classified rocks according to their post peak behavior as class 1 and 2.

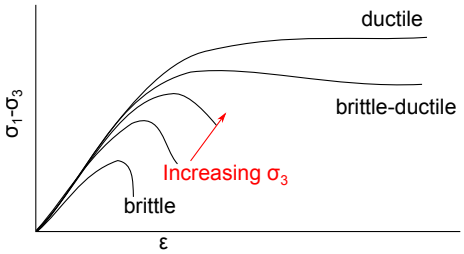

Figure 2.5: Illustration of brittle to ductile transition with increasing confining pressure σ_3.

1. Rock can absorb more energy and continue axial deformation after the peak load

2. Energy needs to be extracted from the rock sample and axial displacement needs to be reduced for a class 2 rock if a quasi-static rock behavior is to obtain.

Class 1 type of rocks are most common to be found. Gowd and Rummel (1980) found that for porous rocks, the brittle-ductile transition is characterized by an abrupt change from dilative behavior at low pressures to compaction during inelastic axial strain at high pressures. This abrupt change they found in experiments on sandstone from SW-Germany. In low porosity rocks (e.g. Carrara marble with 1% porosity) dilation persists well into the ductile regime (Edmond and Paterson, 1972). The compaction that occurs during ductile deformation in porous rocks at high confining pressures is due to pore collapse and the rearrangement of the grains to allow for a denser packing.

Nearly all rocks, as well as concrete, become dilatant prior to fracture in compression, even under high confining pressure(Brace and Martin III, 1968). Dilation represents an increase in porosity, and changes in porosity can lead to changes in pore pressure. Although pore pressure within their samples could have changed.

In experiments on the failure strength of mica, Obreimoff (1930) noted that the confining pressure is of influence on the crack propagation velocity. In the experiment a glass wedge is inserted into a crack. It was observed that the crack did not grow immediately to its equilibrium length: in air (atmospheric pressure) equilibrium was reached within seconds, whereas in a vacuum the crack continued to creep for several days. Thus the confining stress can also be of influence on the time scale of the mechanical behavior of a rock.

2.2.6. Grain size effects

The size and shape effects of the component minerals in the rock are of significant effect, i.e. in general a smaller grain size leads to a tougher rock. Additional features of the micro-structure that influence the mechanical response of the rocks is the degree of interlocking of the grains. Fracture is more likely to occur along the grain boundaries instead of through the grains and therefore fracture propagation

is more difficult in an irregular structure. Onodera and Kamura (1980) found that a linear relationship exists between compressive strength and grain size for granite, i.e. strength increases with decreasing grain size.

In many sedimentary rocks the bond between the grains is provided by cement rather than the interlocking of grains. The amount and type of cement is important as it not only influences the strength and elasticity of the rock, but density, porosity and permeability as well.

2.2.7. Strain rate effects

Li et al. (2013) performed direct tension tests with dry materials and confining pressures. In these tests they varied both the strain rate and the confining pressures on samples of gypsum. They varied the strain rate in the range of 10^{-5} to $3.0 \cdot 10^{-2}$. In case of no confining pressure, the tensile strength increases from 1.72 MPa to 3.57 MPa from low to high strain rates. They compare this result with BTS tests with varying strain rates as well, which gives comparable results. Furthermore, they measured that with increasing side confinements, the strengthening effect due to increasing strain rates decreases. They noted the same phenomenon for granite.

2.2.8. Specimen size effects

Experimental results show that the rock strength decreases significantly with increasing sample size. Hoek and Brown (1980) suggested that the UCS of a specimen with a diameter of d mm is relates to the UCS value of a specimen with a 50 mm diameter, based on published data, through

$$\sigma_{cd} = \sigma_{c50} \left(\frac{50}{d} \right)^{0.18} \tag{2.4}$$

with σ_{cd} as the compressive strength of a sample with diameter d and compressive strength of a specimen with diameter of 50 mm σ_{cd}. Medhurst and Brown (1996) found that with decreasing specimen size not only the UCS value increases, but also the internal friction angle increases. Hoek and Brown (1997) suggest that the reduction in strength with increasing specimen sizes is due to the larger opportunity for failures to occur. When the specimen size is sufficiently large, the strength of the sample reaches a constant value.

2.3. Fluid Saturated Rock

Unless stated otherwise it is assumed that the fluid in the rock is a liquid. The presence of a pore fluid in rock can have effects on the mechanical response of the rock. This can either be the result of one or a combination of two possible effects (Duda and Renner, 2013):

1. Physico-chemical interactions between solid constituents of rocks and pore fluids are controlled by mineralogical composition, pore fluid chemistry and micro-structural features.

2. Hydro-mechanical effects, also often referred to as drainage effects. Volumetric deformation of the local pore volumes result in a change of the local pore

pressure. When the deformation process is more rapid than that the pore fluid can flow, the local pore pressure gradients will affect the mechanical response of the rock as well.

This thesis focuses on the hydro-mechanical effects of a pore fluid on the rock cutting process. Physico-chemical effects might be of interest when comparing dry and saturated conditions of the same type of rock. Such a comparison is beyond the scope of this research, as rock will be cut when it is submerged by seawater or drilling fluid, that . For sake of completeness, a brief overview of the physico-chemical effects is presented here.

2.3.1. Physico-chemical effects

Most of the research towards physico-chemical effects of a pore fluid in rocks uses water as the pore fluid. The effect of water on the strength of rock is highly variable across different types of rocks, as is shown in table 2.1. This is understandable, as the physico-chemical interactions between water and the constituent of rock grains are largely influenced by mineralogical composition, pore volume and shape, grain size and other micro-structural properties, which vary greatly between different rock types. However, the effect of water is more pronounced in clay-rich rocks and siliceous rocks (Atkinson, 1984; Reviron et al., 2009) than in quartz-rich rocks. Clay minerals in water-saturated rock weaken its strength by two mechanisms; chemical reactions with water (Cook, 1999) and reducing the frictional coefficient of rock (Byerlee, 1978; Morrow et al., 2000).

Table 2.1: Ratio of unconfined compressive strength at saturated condition to that of dry conditions, after Zhang et al. (2005).

$\frac{\sigma_{c(sat)}}{\sigma_{c(dry)}}$	Rock type	Originally published in
0.50	Shale and Quartzitic sandstone	(Colback and Wild, 1965)
0.76	Penrith sandstone	(Dyke and Dobereiner, 1991)
0.75	Bunter sandstone	(Dyke and Dobereiner, 1991)
0.66	Waterstone	(Dyke and Dobereiner, 1991)
0.97	Oolitic limestone	(Lashkaripour and Ghafoori, 2002)
0.62	Sandstone and sandy limestone	(Lashkaripour and Ghafoori, 2002)
0.81	Oolitic limestone and limy sandstone	(Lashkaripour and Ghafoori, 2002)
0.52	Shale	(Lashkaripour and Ghafoori, 2002)
0.76	British sandstone	(Vasarhelyi, 2003)
0.66	Miocene limestone	(Vasarhelyi, 2005)

Vutukuri (1974) used various pore fluids (e.g. water, glycerine, alcohols) to test their effects on the tensile strength of Indiana limestone. The results suggested that with increasing dielectric constant and surface tension of the liquid, the tensile strength of the limestone increases as well. Swolfs (1972) found that with aluminum and ferric iron salt solutions in water react with the surface structure of quartz and silicates. Resulting in a reduction in surface energy, surface cohesion and breaking

strength of the rock. However, the coefficient of internal friction remains the same.

2.3.2. Hydro-mechanical effects

The flow and pressure of a pore fluid can significantly affect the mechanical response of a rock. Depending on the field of application it is referred to as hydro-mechanical coupling (e.g. rock mechanics), or drainage mechanisms (e.g. dredging industry). Hydro-mechanical coupling is mainly caused by the combination of (local) volumetric deformation of the pores and fluid flow. The analysis starts with a discussion of the concept of permeability and to what extent the permeability can change due to deformation of the rock, and thus affecting the flow of the fluid. This is followed by a discussion on how the hydro-mechanical coupling affects the mechanical response of a rock.

Effective stress

Drainage mechanisms control the effective stress in a rock. Pore pressures work as a counteracting effect on the normal stress in a rock, which is expressed by Terzaghi's law of effective stress Terzaghi (1943). The effective stress law is defined as

$$\sigma' = \sigma - p \tag{2.5}$$

with effective (particle-particle) stress σ', total stress σ and pore fluid pressure p.

Several corrections on the effective stress for rock were proposed by Skempton (1960), which were experimentally verified by Nur and Byerlee (1971). According to them the effective stress in rocks is given by

$$\sigma = \sigma' + \alpha_{es} p = \sigma' + \left(1 - \frac{C_s}{C_f}\right) p \tag{2.6}$$

with α_{es} the effective stress factor, C_s compressibility of the solids (i.e. of a single grain) and C_f compressibility of the fabric (i.e. solid skeleton, bonded grains). It must be noted that the influence of porosity is considered indirectly in (2.6) in the parameter for the compressibility of the skeleton. When considering a material with high porosity, the skeleton is far more compressible compared to the individual grains $C_s \ll C_f$, i.e. $\alpha_{es} \approx 1$. In the limit of a material with very low porosity, the compressibility of the skeleton is almost comparable to the compressibility of the individual grains ($\alpha_{es} \approx 0$), where the effect of the pore pressure is negligible. It is mentioned by van Kesteren (1995) that (2.6) has limitations on its applicability. He states that the correction is only applicable when only deformation of the skeleton is considered. Van Kesteren therefore suggests the use of pore pressure dissipation. In the perfectly undrained case, the limit pressure of the pore-water that can be generated with respect to the total/effective stress, which is then given by:

$$\frac{\sigma}{p_{undr}} = 1 + n \frac{C_p - C_s}{C_f - \alpha_{es} C_s} \tag{2.7}$$

van Kesteren (1995) mentions that the compressibility of the pore-water is influenced by the presence of a gaseous phase in the pore-water. When the dissolution

of the gas is negligible (e.g. the loading is sufficiently fast) the compressibility of the pore-water is given by Cools (1984):

$$C_p = \frac{1-v}{u} + \left(C_l - \frac{1}{p}\right)\left(1 - v - (1 - S_i - v)\,\frac{p_i}{p}\right) \tag{2.8}$$

with compressibility of the pore water C_p, initial saturation degree S_i, initial pore-fluid pressure p_i and the gas fraction adsorbed by solids v. Due to the very high pressures in deep sea applications and at the tool tip, it is assumed that the compressibility of the pore-water is equal to pure water.

Brady and Brown (2005) show that the influence of pore water pressure on the behavior of porous rock in tri-axial compression tests is strongly dependent on the 'effective' confining pressure (similar to Terzaghi's principle): A series of tri-axial compression tests was carried out on a limestone with a constant value of $\sigma_3 = 69MPa$, but with various levels of pore pressure in the range $u = 0 - 69MPa$ applied. There is a transition from ductile to brittle behavior as u is increased from 0 to $69MPa$. In this case the mechanical response is controlled by the effective confining pressure, $\sigma_3' = \sigma_3 - u$, calculated using Terzaghi's classical effective stress law. For less permeable rocks than this limestone, it may appear that the classical effective stress law does not hold, as is stated by Brace and Martin III (1968) concerning the dilatancy hardening effect.

Permeability of rock

The permeability of a porous material is a measure for its capability to transmit a fluid. The term permeability might lead to confusion, in practice two permeability related parameters are used, i.e. the permeability coefficient and the intrinsic permeability. The permeability coefficient (or hydraulic conductivity) K_{hyd} is defined as a discharge velocity through a unit area under a unit hydraulic gradient and is dependent on the properties of the porous medium as well as the fluid, e.g. density and viscosity. The intrinsic permeability κ is a property of only the porous medium itself and thus independent of the fluid properties. The two are related (in the case of hydraulic conductivity with water properties) through

$$K_{hyd} = \kappa \frac{\rho g}{\eta} \tag{2.9}$$

with fluid density ρ, gravitational acceleration g and dynamic viscosity η. The intrinsic permeability is used in this dissertation, because it is independent of the fluid properties. According to Darcy's law, the quantity of flow through a porous medium is determined by

$$\mathbf{q} = -\frac{\kappa}{\eta}\nabla p \tag{2.10}$$

where $\mathbf{q}$ is fluid flux.

Various empirical relations relate the intrinsic permeability with porosity, or grain size (Schön, 1996). Both correlations can be used to estimate the permeability of a rock.

The intrinsic permeability of a rock can change due to the loading that is applied to the rock. There are various ways to describe such a change in permeability. In a

direct way, the effective stress state can be linked to the permeability of intact rock. Various researchers found an empirical relationship based on a negative exponent, a negative power law or Hertz theory to describe the relationship between effective stress and the permeability at zero effective stress (Tiller, 1953; Louis et al., 1977; Gangi, 1978):

$$\kappa = c_1 \sigma_{eff}^{-c_2} \qquad (\sigma' > \sigma_{threshold}) \qquad \text{Tiller (1953)} \tag{2.11}$$

$$\kappa = \kappa_0 e^{-\sigma'} \qquad \text{Louis et al. (1977)} \tag{2.12}$$

$$\kappa = \kappa_0 \left(1 - C_0 \left(\frac{\sigma' + \sigma_i}{E_0}\right)^{2/3}\right)^4 \qquad \text{Gangi (1978)} \tag{2.13}$$

with constants A and m, effective stress σ_{eff}, threshold stress above which the equation is valid $\sigma_{threshold}$, permeability at zero effective stress κ_0, constant depending on the packing C_0, equivalent pressure due to permanent deformation and cementation of the grains and the effective elastic modulus of the grains E_0. In a less direct way, the permeability can change due to deformation of the matrix of the porous material. The deformation can be described linked to a change in porosity. As an example, the Carman-Kozeny relation describes the relation between porosity and permeability for a packed bed of solids.

$$\kappa = \frac{\Phi_s^2 d_p^2 n^3}{180\,(1 - n^2)} \tag{2.14}$$

with particle sphericity Φ_s, particle diameter d_p and porosity n. Due to the asymptotes that occur near the limits of zero porosity or full porosity (0-1), close to those boundaries the validity of the Carman-Kozeny relation is doubtful. For a graphical representation and the asymptotic limits, see figure 2.6.

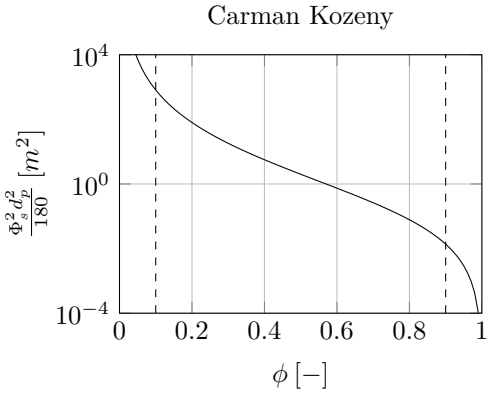

Figure 2.6: Carman Kozeny relation for permeability.

Although the permeability depends on the deformation or effective stress state of the rock matrix, the resulting change in permeability while the rock is still intact

results in a permeability of the same order of magnitude, which is already close to the accuracy of the measured permeability that is used in the industrial applications for rock cutting. Besides, the change in permeability due to deformations strongly depends on the micro-structure of the rock matrix. In the case of damaged rock, it can no longer be assumed that the permeability is isotropic and homogeneously distributed throughout the specimen and the use of more advanced porosity and permeability models might be required (e.g. dual porosity/permeability, large discontinuities).

Drainage response

When considering the compressive strength of a rock, the effective stress law is only valid below a critical strain rate, below which effective drainage of the sample is achieved Brace and Martin III (1968). A sample is considered to be effectively drained when the local pressure differences due deformation rate are significantly smaller than the compressive and/or tensile strength of the rock, i.e. $\Delta p \ll \sigma_c, \sigma_t$. However, at higher deformation rates, the local pressure differences can contribute to the strength of the rock, an example of such a phenomenon is dilation hardening with respect to compressive strength Brace and Martin III (1968). Another effect that might occur is compaction weakening. Which effect is more likely to occur depends on the micro-structure of the rock. It is reasonable to assume that similar trends are valid for tensile strength (if it is tested at a sufficiently high hydrostatic pressure, to allow for a significant pressure difference to build up without having the fluid to cavitate). As a result, the observed material behavior can change with deformation rate and total hydrostatic pressure to which it is subjected.

Bulk compaction is related to the collapse of the rock matrix, which causes a reduction in pore volume. This reduction leads to an increase in pore pressure, which can lead to a decrease in effective stress, resulting in a reduction in compressive strength Bernabe (1987). During dilation, the porosity increases due to the creation of new and the extension of existing micro-cracks. As a result, the pore pressure of an effectively undrained sample drops locally, resulting in an increase of the effective stress and thus an increase in compressive strength, which is often referred to as dilatancy hardening Brace and Martin III (1968). The effect of dilatancy hardening is associated with a critical strain rate $\dot{\epsilon}_{cr}$ and strongly depends on the hydraulic properties of a rock. At strain rates above $\dot{\epsilon}_{cr}$, the apparent strength of a rock increases more compared to that of a drained or dry sample.

Two mechanisms can limit the effect of dilatancy hardening, i.e. cavitation and grain failure (Zijsling, 1987). When during dilation the pore pressure decreases to the vapor pressure of the pore fluid, the fluid will vaporize and the fluid bulk modulus and viscosity both decrease by several orders of magnitude. As a result the pore pressure in the cavitated region does not decrease anymore. In the case of grain failure, the contact stresses at the grain boundaries can exceed the strength of the grain. As a result, grains will fail, giving rise to a smoother surface and reducing the amount of dilation needed before grains can slide along each other and thus effectively a smaller drop in pressure in the dilating region. A schematic representation of the dilatancy hardening effect and its limits is shown in figure 2.7.

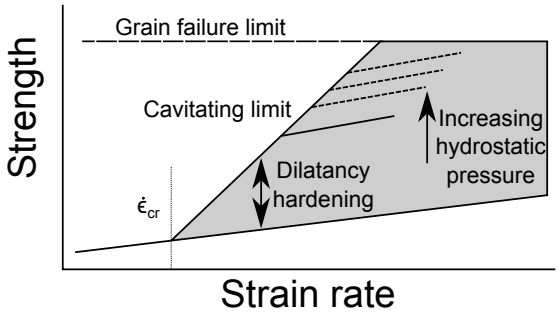

Figure 2.7: Phenomenon of dilatancy hardening and its limitations, based on Brace and Martin III (1968)

Analysis of Rudnicki and Chen (1988) on data of Martin III (1980) shows that slip-induced dilation coupled with the flow of pore fluid can stabilize rapid slip. Only a small amount of dilation, corresponding to uplift of the order of a few percent of the slip is needed. However, the stabilizing effect decreases with decreasing pore fluid bulk moduli. As a result, when instabilities in the pore pressure occur due to cavitation or the dissolution of gases from the pore fluid, ultimately lowering the resistance towards dilation.

Even in the absence of dilation, strengthening occurs when local fluid motion is restricted, because of the coupling between elastic deformation and pore fluid movement around the crack tip. Rice and Cleary (1976) analyze propagation of shear cracks in porous elastic media, and they find a dependence of the energy release rate on the velocity of propagation of the crack. This effect arises from the elastic distortion of the material around the crack and means that higher driving forces are required at higher crack velocities. In other words, the undrained response at the tip of the crack has a higher stabilizing effect with respect to drained response.

Rutter (1972) performed experiments with varying strain rates and effective stresses on Solenhofen limestone saturated with water. Several trends are distinguished by Rutter, i.e. the ductility decreases (more significant strain softening) and the yield strength increases with increasing strain rates; both the yield strength and ductility increase with increasing confining stress.

Brace and Martin III (1968) show that the law of effective stress does not always apply for low porosity (0.001-0.03) rock, for deformations above a critical strain rate, Brace and Martin measured an increase in strength beyond the failure criterion. They showed that the validity of the law of effective stress depends on the strain rate, the intrinsic permeability and the pore-fluid viscosity (note that it also depends on the fluid compressibility, but the compressibility of the fluids used by Brace and Martin were too similar to distinguish this effect). Something similar has been observed by Rutter (1972); due to dilation hardening, the observed effective stress in the specimen is higher at the moment of failure compared to that of the initial state of the experiment.

Swan et al. (1989) observed a much larger effect of the increase of the compressive

strength with increasing strain rates for saturated shale from Kimmeridge Bay, Dorset, U.K. They noticed an increase in both strength and strain to failure of the order of four and seven times respectively over three orders of increasing strain rates.

The hydro mechanical behavior of saturated rock is directly related to the amount of drainage allowed by the applied deformation, which is often referred to as the Deborah number (here N). According to Duda and Renner (2013), for compression tests this can be characterized by the ratio

$$N = \frac{t_c}{t_{def}} \tag{2.15}$$

of the characteristic time of hydraulic diffusion t_c to the characteristic time of deformation t_{def}. The characteristic times are defined as

$$t_c = \frac{l^2}{D} \tag{2.16}$$

with characteristic length scale l and hydraulic diffusion coefficient D, and

$$t_{def} = \frac{\Delta\epsilon}{\dot{\epsilon}} = \frac{0.1\epsilon_f}{\dot{\epsilon}} \tag{2.17}$$

with strain ϵ, strain to failure ϵ_f and strain rate $\dot{\epsilon}$. In a similar fashion to Duda and Renner (2013), it is assumed that the characteristic strain should be one order of magnitude smaller than the strain to failure ϵ_f. The Deborah number shows strong resemblance with the pore Peclet number that is used in dredging applications, which will be treated in section 3.1.6. The transition between drained and undrained behavior occurs at $N_{cr} \approx 1$. Duda and Renner derived the critical strain rate above which the effective internal drainage is lost, with respect to compression tests. The critical strain rate is given by

$$\dot{\epsilon}_{cr} \approx 0.1\frac{N_{cr}\epsilon_f D}{l^2} \tag{2.18}$$

with critical strain rate $\dot{\epsilon}_{cr}$, strain to failure ϵ_f, hydraulic diffusion coefficient D, and specimen length l. The hydraulic diffusion coefficient is determined based on the specific storage capacity

$$D = \frac{\kappa}{\eta s} = \frac{\kappa}{\eta\left(C_f - \alpha C_s + n\left(C_p - C_s\right)\right)} \tag{2.19}$$

with intrinsic permeability κ, fluid viscosity η, specific storage capacity s, coefficient for solid compression α, porosity n, compressibility of the rock matrix, solid grains and fluid, respectively C_m, C_s and C_f (cf. Duda and Renner (2013); van Kesteren (1995)).

Another explanation for the change in mechanical response beyond the critical strain rate is given by Swan et al. (1989), which is that since only localized fluid movement is allowed at high strain rates, the nucleation and growth of a crack in one part of a specimen does not affect the pore pressure distribution in the bulk. Thus

when one crack is formed and subsequently strengthened, it is easier for another crack to grow elsewhere in the specimen than it is to continue to grow the original crack. This process of stabilization is repeated for each crack that forms, so that the deformation becomes de-localized, linkage of cracks is suppressed and the strain to failure increases.

Some other qualitative observations on the influence of the strain rate on the rock mechanics were observed by Masuda et al. (1987) in experiments on granite, i.e. the AE rate is accelerated at a stress level closer to the failure stress as the strain rate decreases. In other words, slow strain rate results in a more perfect macro-crack. Furthermore, Masuda et al. (1987) observed that the strength of the rock linearly increases as the logarithm of the strain rate increases and that the strain rate dependence is enhanced at high confining stresses.

2.4. Conclusions

To summarize, the most relevant physical phenomena that can have a significant influence on the rock cutting process are identified. Only physical effects that directly affect the rock cutting process should be considered, assuming that the in-situ conditions are reasonably recreated in lab tests. In dry rocks, a distinct effect is noticeable with the presence of a confining stress. That is, with an increase in confining stress the compressive strength of the rock increases. Furthermore, a transition from brittle to ductile failure might occur.

In the case of saturated rock, one should also consider the effects of dilation hardening, compaction weakening, cavitation, bulk stiffening, together with a more profound strain rate dependency of the mechanical properties. Due to differences in mechanical response through physico-chemical effects, one has to be cautious when comparing mechanical properties of dry and saturated bulk material with respect to the rock cutting process.

3

Rock Cutting Process

"... once a theory appears on the question sheet of a college examination, it turns into something to be feared and believed, and many of the engineers who were benefited by a college education applied the theories without even suspecting the narrow limits of their validity"

Karl von Terzaghi

In this chapter the current state of the art of the knowledge concerning the rock cutting process is discussed. Starting with the phenomena that occur when cutting saturated rock, with an emphasis on dredging, seabed mining and drilling tools. Various rock cutting models concerning the use of different kinds of equipment and different types of rocks are presented. These models can be useful to aid the design of excavation equipment. However, due to the simplifications and assumptions that are made to develop these models, their use for research into the cutting process itself have their limitations.

This chapter starts with an overview of the cutting mechanisms and the phenomenological models for (saturated) rock cutting in general is presented. This is followed by an overview of the most relevant cutting parameters and how these affect the cutting process itself. Many researchers have developed analytical and/or semi-empirical models for rock cutting. Within this dissertation, the focus is on the models for drilling and dredging/seabed mining. Although these models can be powerful tools for the engineering and design of equipment, they are less suited to investigate the rock cutting process itself. The assumptions and limitations of these models are discussed as well.

3.1. Phenomenological rock cutting model

3.1.1. General concepts

The drilling and dredging/deep sea mining processes show many similarities. In all cases saturated rock is cut at a higher hydrostatic pressures, although the increase in hydrostatic pressure with respect to the strength of the rock is rather limited for dredging applications. The most significant differences between drilling and dredging/mining are the rake angle and the typical thickness of the layer being cut. In drilling the rake angle is often negative while in dredging applications a positive rake angle is more common. The definitions used in literature vary. For that reason, in this work, a positive rake angle is defined as the cases where the cutting edge precedes, and in the case of a negative rake angle the cutting edge follows in the direction of motion, see figure 3.1 for clarification. The typical cutting thicknesses are within the range of sub-millimeter to several millimeters for drilling, while in dredging often layers of several centimeters thick are excavated in a single motion.

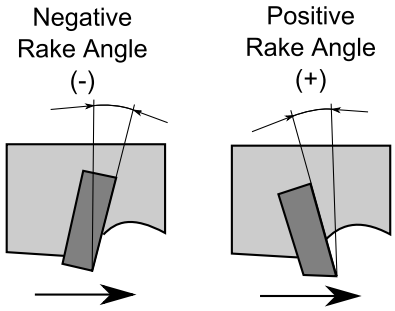

Figure 3.1: Definition of positive and negative rake angles.

Similar to the failure mechanisms that result in macro-scopic failure of a rock specimen, the same failure mechanism can dominate the rock cutting process given the tool, rock properties, environmental conditions, etc. These can be divided into either continuous (ductile) plastic, discontinuous shear (brittle) dominated or discontinuous tensile dominated (brittle) cutting, as depicted in figure 3.2. These characteristic failure mechanisms are often used as a basis for the various rock cutting models, which are treated in section 3.2.

The rock cutting process is a complex process to model, as it concerns the transition of intact rock, through fragmentation towards granular media.

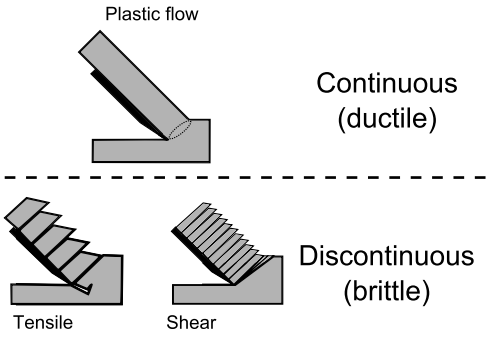

Figure 3.2: Dominant failure types in rock cutting.

A measure that is often used to compare rock cutting equipment is the specific energy E_{sp}, which is a property of the cutting process itself. Specific energy is defined as the amount of energy that is needed to excavate a certain volume of rock, which can be calculated as

$$E_{sp} = \frac{\int_0^T P_c dt}{\int_0^T Q_c dt} \qquad \text{which is often simplified to} \qquad \frac{F_c v_c}{t_c w v_c} = \frac{F_c}{t_c w} \tag{3.1}$$

with total time T, power of equipment that is used to excavate the rock P_c, the excavation production Q_c, the cutting force F_c, the cutting velocity v_c, cutting depth t_c and width of the tool w. Note that the dimension of E_{sp} is often noted as Pa, which is identical to J/m^3. In general, the E_{sp} increases when the cutting process enforces the rock to fragment into smaller pieces.

3.1.2. Dredging and seabed mining

van Kesteren (1995) developed a phenomenological model which explains the chip formation process in terms of the critical state theory of rock failure, see figure 3.3. First the tool moves towards the rock, resulting in penetration of the rock. At this stage, the rock directly underneath the tool undergoes crushing in compression, creating a crushed zone. In the crushed zone (I), the stress state is beyond the volumetric cap. At the boundary of the crushed zone (II), the stress state is on the volumetric cap, near the brittle-ductile transition stress (BD). When the tool moves further into the intact rock, the boundary of the crushed zone will move further into the rock. The growth of the crushed zone is proportional to the penetration depth of the tool. Just outside the crushed zone, shear failure will occur (III). Further away in the intact rock, the stress state will be below the brittle-ductile transition and the isotropic stress decreases. The decrease in stress results in a shear crack that bifurcates into a tensile crack (IV). After bifurcation unstable crack growth will result in chip formation. As is shown in figure 3.3 intact rock is subjected to failure mechanisms along the complete failure envelope. To what extent each of

the mechanisms contributes to the cutting process depends on the rock properties, environmental conditions (e.g. ambient pressure, surrounding fluid) and the tool (geometry, machining conditions).

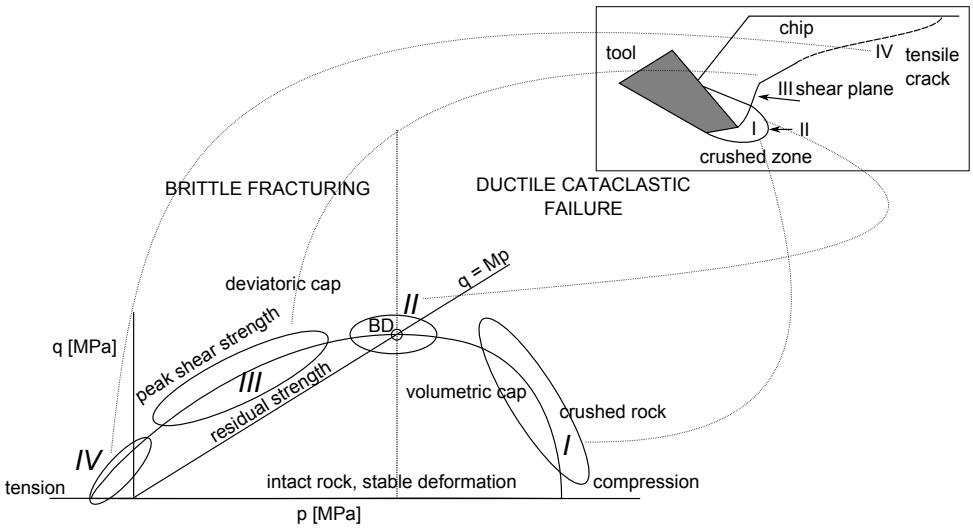

Figure 3.3: Failure during rock cutting involves the entire failure envelope, given in a hydrostatic-deviatoric stress diagram. Figure is based on Verhoef (1997). ($p = 1/3(\sigma_1 + 2\sigma_3)$ and $q = \sigma_1 - \sigma_3$)

3.1.3. Drilling

In drilling engineering, the cutting process is somewhat different. The main differences are the rake angle, which is in general negative for drilling purposes, and the characteristic cutting depth. In drilling, cutting depths are in the range of (sub-)millimeter scale compared to range of several centimeters for dredging applications. Both due to the smaller cutting depth and the negative rake angle, the failure mechanisms mainly consist of the crushing of the rock along the whole cutting depth and that the removal of material is in the ductile regime. Brittle failures still can occur, but due to the negative rake angle mostly brittle shear occurs. Tensile failures are less likely to occur because the negative rake angle has the tendency to constrain the propagation of tensile cracks by forcing them to close. A resultant of the crushed zone is the heavily damaged and plastic deformed layer that is left behind after the tool has passed. In industry this is often referred to as filter cake. An overview is given in figure 3.4.

3.1.4. Effect of geometry

Many aspects of the cutter geometry can have an influence on the rock cutting process. Here only the most important geometrical parameters are discussed, being the rake angle, cutting depth, wear flat and tool spacing.

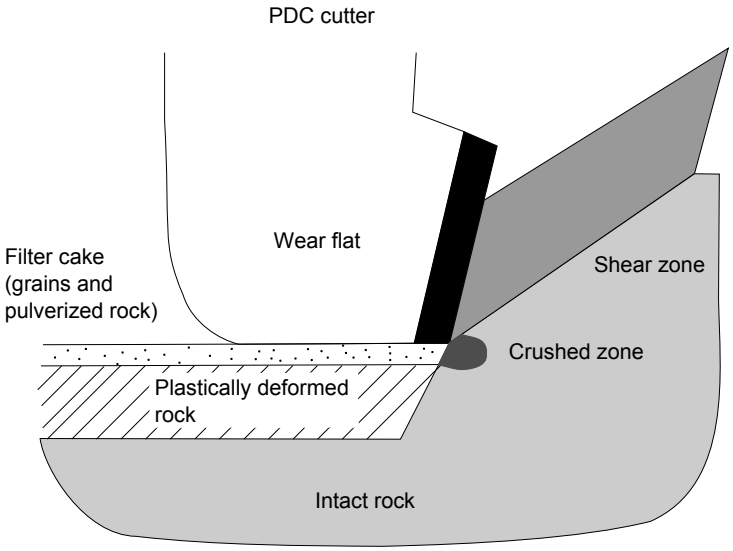

Figure 3.4: Conceptual model of a boundary layer underneath a blunt drill bit, after Dagrain and Richard (2006).

Cutting depth

Two modes of failure can be identified depending on the cutting depth (Richard et al., 2012). At small cutting depths, (typically larger than the grain size and less than 1 mm in sandstones), rock fails in a ductile mode, which looks like a continuous plastic flow of crushed rock. The cutting mode is also often referred to as scratching or grinding. As the cutting depth increases beyond a threshold the cutting mode transitions towards a brittle chipping mode. The differences in behavior are noticeable on force measurements as well. In measurements in the ductile regime, the force signal looks more like white noise, while for measurements in the brittle regime, the force signal behaves more like a saw -tooth pattern with peaks and valleys corresponding to the chip formation (Verhoef, 1997; Huang, 1999). Chaput (1991) made similar observations on the failure mechanism in rock cutting. Chaput also noted that the critical cutting depth at which the brittle-ductile transition occurs decreases with increasing uni-axial compressive strength of the rock. Based on measurements of the cutting force with respect to cutting depth on Berea sandstone, Richard et al. (1998) suggest that the critical depth at which the brittle-ductile regime occurs scales according to

$$t_{c,crit} \propto \left(\frac{K_{Ic}}{\sigma_c} \right)^2 \tag{3.2}$$

with critical cutting depth $t_{c,crit}$ and fracture toughness K_{Ic}. The ductile regime is associated with cohesion or compressive strength. Therefore the mean cutting force

in the ductile regime scales according to (Richard et al., 1998)

$$\frac{F_c}{w} \propto \sigma_c t_c \tag{3.3}$$

with cutting force F_c and width of the cutting tool w. In the brittle mode the formation of cracks dominates the process. Therefore scaling of the brittle regime is according to

$$\frac{F_c}{w} \propto K_{Ic}\sqrt{t_c} \tag{3.4}$$

For a graphical representation of the scaling properties, see figure 3.5 Similar observations to the brittle-ductile transition with respect to cutting depth are observed by Liefferink (2013); Motzheim (2016) in cutting experiments on frozen clay, although in a different tool configuration, i.e. positive rake angle of 22°, cutting depths ranging from 5 to 25 mm.

In discrete element simulations of He and Xu (2015), in which the micro-structure of the simulated rock is varied, similar trends are observed. Rock cutting simulations of intact homogeneous rock are compared with a heterogeneous rock simulation based on a clustered particle assembly. Various simulations are performed with varying cutting depths. The obtained results show that the clustered particle assembly has a less steep increase in cutting force compared to the homogeneous rock. Additionally it is observed that in cutting simulations on the heterogeneous sample failure occurs along the cluster boundaries when the cutting depth is of similar size or larger than the characteristic length scale of the clusters. Both simulated rocks have a similar compressive strength (155 MPa), although the tensile strength of the heterogeneous sample is significantly lower (36 vs. 16.5 MPa), so the less steep increase in cutting force for the heterogeneous sample might be as well a result of the significant difference in tensile strength, but this was not tested by He and Xu (2015). In rock cutting, the importance of the tensile strength of the rock is too often neglected, while tensile failure can have a significant influence on the cutting process.

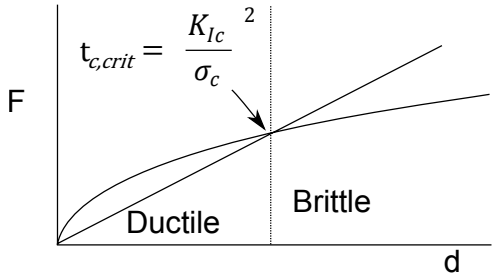

Figure 3.5: Scaling of cutting force with respect to cutting depth, based on Richard et al. (1998).

.

In scraper tests studied by Deketh (1995), in a setup similar to a turning machine. In these experiments, Deketh observed a transition in cutting forces and cutting regimes. However, instead of a cutting force that increases monotonously with

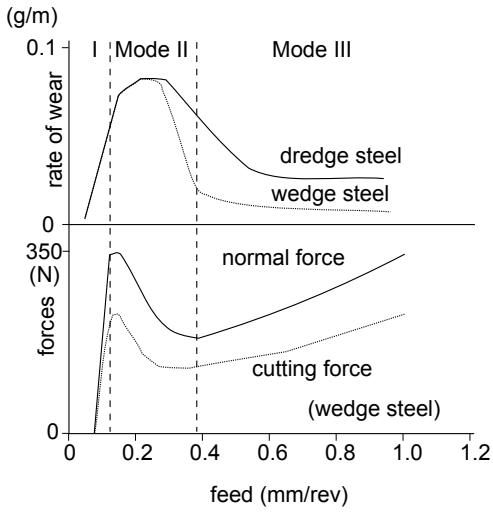

Figure 3.6: Scaling of cutting force with respect to cutting depth and rate of wear with respect to cutting depth, based on Deketh (1995).

.

respect to the cutting depth, as would have been expected based on the experimental results of Richard et al. (1998), a significant peak is observed at the transition from ductile cutting (scraping) to chipping, see figure 3.6. The difference in trends for the cutting force with respect to the cutting depth between the experiments of Deketh (1995) and Richard et al. (1998) is most likely due to the setup that has been used. There are two explanations to why both set of experiments show different behavior at the brittle ductile transition.

Both do scratching tests on cylindrical specimens, but the direction of the scratch/cutting differs. Richard et al. (1998) performed the experiments in axial direction (milling) of the specimen while Deketh (1995) did experiments in which the main cutting direction is tangential along the cylindrical specimen (turning). Besides, the difference in behavior between the two sets of experiments might as well be caused by the difference in rake angle, being a positive rake angle in the case of Deketh (1995) and a negative rake angle in the case of Richard et al. (1998). Furthermore, the experiments of Deketh are performed on many different types of mortar in which specific parameters are compared to see the effect of it in the scraper test. Not all mortars have shown this type of behavior, based on the results of Deketh there is no direct relation between material parameter(s) and this phenomenon.

Rake angle

Obviously, there is a large distinction to be made between positive and negative rake angles. In general, negative rake angles are more often used in drilling and at smaller cutting depths (in the range up to a few millimeters) and in tougher rocks, while positive rake angles are typical for dredging and seabed mining applications,

with typically large cutting depths (in the range of several centimeters) and is often applied in weak rock (with UCS up to 20 MPa). Unfortunately, not many experimental results for cutting experiments on saturated rock with varying rake angles are published. This can either be due to the lack of the existence of such experimental data, or that the existence of such data is kept as confidential within the industry, this is especially the case for tools with a positive rake angle.

One of the few datasets with varying rake angles is that of Bilgin (1977), in which small negative rake angles are used for cutting experiments on limestone and granite, respectively having compressive strengths of 127 MPa and 179 MPa. The tensile strength of these rocks are not presented by Bilgin, however, based on the rules of thumb as given in appendix A, the tensile strengths of these rocks are estimated as respectively as 12-16 and 6-10 MPa. See figure 3.7 for the peak cutting forces with respect to the rake angle.

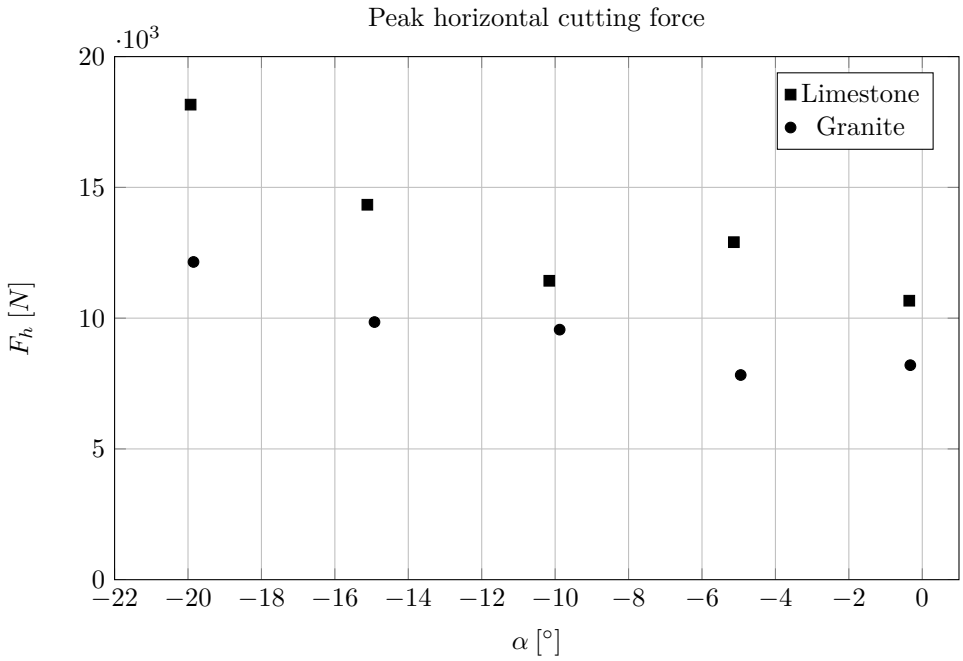

Figure 3.7: Effect of rake angle on peak cutting force, data from Bilgin (1977).

Detournay and Defourny (1992) propose, based on the rigid plasticity, three types of flow regimes based on the (negative) rake angle, namely a forward flow regime, a backward flow regime and a flow regime with a build-up edge, see figure 3.8. The intermediate regime with a build-up edge involves a static wedge of dead material in contact with the tool, in which case both backward and forward flow take place simultaneously. This has also been observed by Zijsling (1984) and Adachi et al. (1996). Similar observations with respect to the occurrence of a build-

up edge are made for metal (Eggleston et al., 1959), dry sand (Hettiaratchi and Reece, 1967; Hatamura and Chijiiwa, 1975) and saturated sand (He and Vlasblom, 1998; Miedema and Frijters, 2003; Miedema, 2014). In the experiments of He and Vlasblom (1998) vertical bars of colored sand were implemented in the sand cutting setup. The observed deformation of these bars during the cutting experiment indicate that the occurring wedge of built-up material is not static, grains in the wedge are transported relative to the tool. However, the transport velocity of grains in the wedge is significantly lower than that of the layer cut. See figure 3.9 for an impression of the transport of grains through the build-up edge. Numerical analysis of the built-up edge has been performed by Huang (1999); Huang et al. (2013) through the use of the discrete element method.

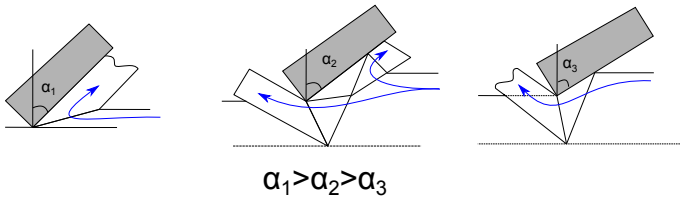

Figure 3.8: Flow regimes: forward flow, backward flow and flow with a build-up edge, all after Detournay and Defourny (1992). Note that because of the definition of the rake angle used in this thesis, $\alpha_1 > \alpha_2 > \alpha_3$ is valid.

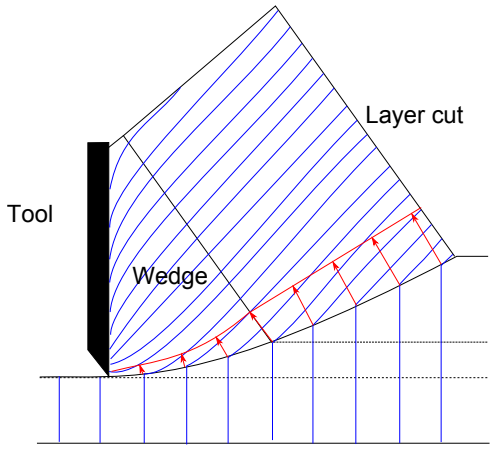

Figure 3.9: Flow lines in the dynamic wedge when cutting sand, after Miedema (2014).

Wear flat

Various researchers have investigated the wear of rock cutting tools (e.g. Deketh (1995); Verhoef (1997); Dagrain and Richard (2006)). In general, the emphasis in these studies is on the abrasive wear of the tool (catastrophic failure or breakage of the tool is disregarded). Most studies distinguish abrasive and non-abrasive wear,

based on the combination of tool material and rock. Most of the rock cutting tools have the shape of a wedge, e.g. PDC-bit, dredging pick-point, dredging chisel. In linear cutting processes, wear results in the removal of a prism of tool material from the cutting edge of the bit.

Although the wear rate is an interesting topic for the research and development of cutting tools, it is the change in shape of the tool that determines the rise in forces. If a tool is able to maintain its shape while wearing down, it would result in a less significant change in cutting force. Some rock cutting tools are designed in such a way they are self-sharpening while during wear. Such a design property can be used in closed form cutting processes like in drilling (Feenstra, 1988) or tunnel boring (Buchi, 1984). Although there are some patents for dredging equipment claiming that they describe self sharpening tools, e.g. (van Opstal, 2015), but the cutter head is filled with bits instead of chisels or pick points.

Experience in practice reveals that the use of sharp tools is merely limited to a short time before the tools become blunt by wear. In linear cutting processes, a wear flat is generated. In drilling, the cutting depth per cutter typically ranges between 0.05 to 2 mm, which shows that PDC bits rarely can be considered as perfectly sharp tools (Dagrain and Richard, 2006). Field and laboratory tests indicate that the drilling response of a blunt bit is characterized by two distinct regimes, see figure 3.10. At low applied W, weight on bit (WOB), the drilling forces with respect to the depth of cut (or rate of penetration (ROP)) is dominated by the frictional processes taking place across the wear flats, as the effective contact area increases with W. Once the maximum forces admissible on the wear flats are mobilized, the evolution of the drilling forces is solely controlled by the cutting process taking place ahead of the cutting faces. Obviously, the first regime is far less efficient.

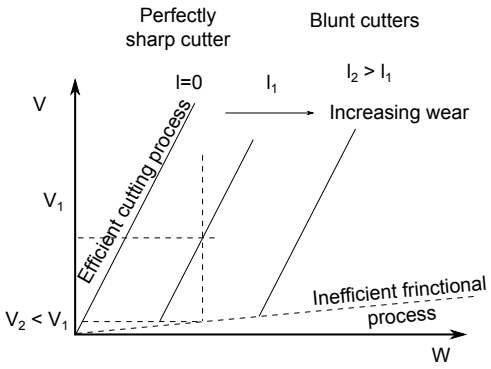

Figure 3.10: Rate of penetration versus weight on bit curves, based on Dagrain and Richard (2006).

Tool spacing

Thus far, the cutting process is only considered with respect to a single cutting tool. Depending on the cutting tool, geometry and rock properties the cross-sectional area of the groove that is cut by a single cutter is often larger than the projection of the tool in that groove. Experiments of Alvarez Grima et al. (2015) clearly show that

the shape of the groove is strongly influence by the operating conditions. In their experiments, hydrostatic pressure and cutting velocity were varied. Figure 3.11 gives an impression to what extent the shape of the groove can be influenced by the operating conditions.

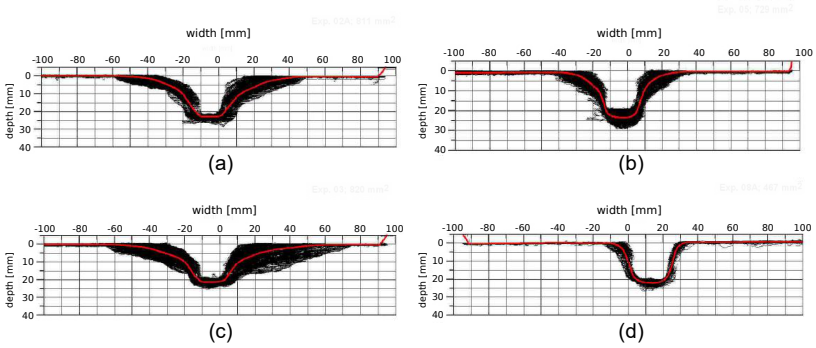

Figure 3.11: Composition of laser scan cut geometry, a) $p_h = 0.1$ MPa and $v_c = 0.2$ m/s b) $p_h = 18$ MPa and $v_c = 0.2$ m/s, c) $p_h = 0.1$ MPa and $v_c = 2.0$ m/s and d) $p_h = 18$ MPa and $v_c = 2.0$ m/s. Each black line represents a single laser scan, the red lines represent the mean groove shape. Data from Alvarez Grima et al. (2015).

Based on the knowledge of the shape of the groove that will be cut, the distance between two consecutive tools can be adjusted to obtain a minimum in energy required to cut the bulk of the rock. Research into the effect of cutter spacing is investigated by Roxborough and Phillips (1975) for applications in TBM's. Roxborough observed the influence of the spacing and penetration of a disc cutter with respect to the magnitude of the cutting forces and specific energy from a liner cutting machine (LCM) test, which is a test on full scale. See figure 3.12 for an overview of the observations made by Roxborough and Phillips (1975). Similar tests were performed by Roxborough and Sen (1986) for the use of picks.

At a tool-spacing of 0, the second tool will move exactly in the shadow of the tool producing the relieving groove, hence the forces and yield are 0. As spacing increases so do the cutting forces and the yield. The maximum in yield is obtained when the grooves have sufficiently distant that they create their own grooves, but still have interaction with the groove that is closest by. Lateral cracks from the two neighboring grooves combine to remove the ridge that would have otherwise existed. As the spacing further increases, the grooves lose the interaction with neighboring grooves, resulting in purely unrelieved cutting. See figure 3.13 for an overview, where Θ is the edge angle of the cutter disc. Here yield ratio is defined as the ratio of relieved (Q_r) to unrelieved (Q_u) rock cutting.

Various researchers have investigated what the optimum distance between the cutting tools should be used in the design of the equipment. Evans (1972) estimates that the optimum spacing for chisel shaped tools, by using the width of the chisel

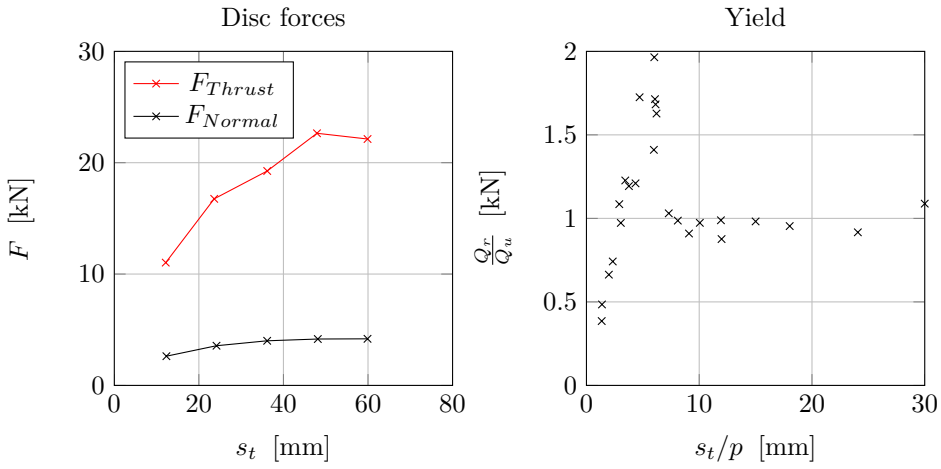

(a) Disc forces

(b) Yield ratios for relieved cutting

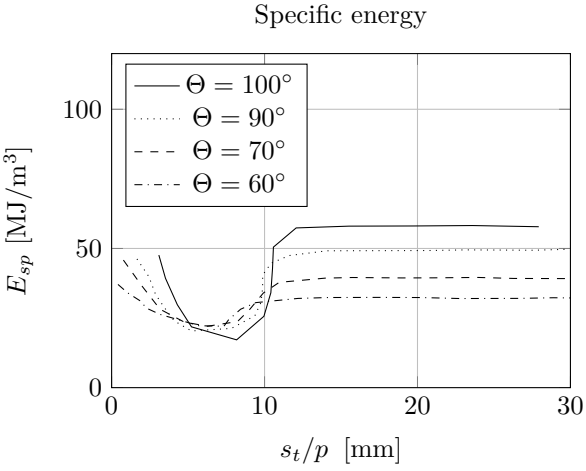

(c) Specific energy

Figure 3.12: Effect of spacing on various parameters, from Roxborough and Phillips (1975).

and the cutting depth, is determined as

$$s_t = 0.001\frac{w}{2}\left(1+\sqrt{\left(1+\frac{20t_c^2}{w^2}\right)}\right) \tag{3.5}$$

with optimum spacing s_t, width of the tool w and depth of cut t_c. For pick-points, Evans (1984) found the following approximate relation

$$s_t = 2t_c\sqrt{3} \tag{3.6}$$

For roller discs, Roxborough and Phillips (1975) determine the optimum spacing

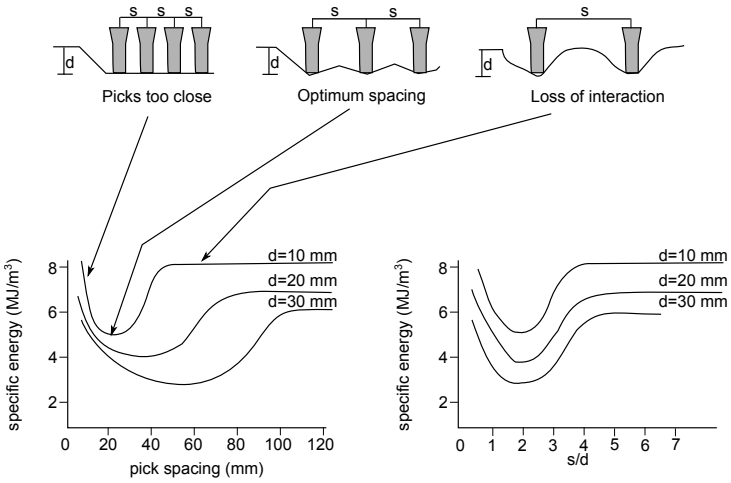

Figure 3.13: Effect of pick spacing on specific energy (Roxborough and Sen, 1986).

based on the rock properties to be

$$\frac{s_t}{t_c} = \frac{\sigma_{UCS}}{\tau_s} \tag{3.7}$$

with the rock's unconfined compressive strength σ_{UCS} and the rock's simple shear strength τ_s. Snowdon et al. (1982) shows that there is a constant $\frac{s_t}{t_c}$ ratio for minimum tool specific energy. However, they explain that there is no simple relation between the optimized $\frac{s_t}{t_c}$ ratio and any combination of rock strength parameters. Rostami and Ozdemir (1993) postulate that there are three different chipping patterns in terms of specific spacing, being too close, optimum spacing and loss of interaction due to a too large space between the tools, see figure 3.13.

3.1.5. Effect of rock properties

Verhoef (1997) makes a distinction between brittle and ductile cutting to explain differences in wear rate with respect to the type of rock being cut, Verhoef makes this distinction based on the rock properties. Verhoef's definition of ductile cutting might lead to misinterpretation, it is more accurate to refer to this as brittle shear dominated or cataclastis dominated cutting. In such a case, the stress state in the crushed zone reaches well above the brittle-ductile transition, resulting in a large crushed zone near the tool tip. In the case of brittle cutting the stress level in the crushed zone is slightly above the brittle-ductile transition, resulting in a relatively smaller crushed zone.

Furthermore, the distinction between brittle tensile and brittle shear dominated cutting processes can be made depending on the strength ratio as well. Unfortunately, there is no clear consensus on what values of m the failure regimes occur. Natau et al. (1991) states the criteria for the application of roadheaders (tunnel boring) and Verhoef (1997) states the criteria for use in dredging applications, while

both state that their criteria are based on Gehring (1987) (which is an internal report of Voest Alpine Zeltweg). The criteria are presented in table 3.1

Table 3.1: Characteristics of strength ratio for rock cutting

Failure mode	Natau et al. (1991) Roadheader	Verhoef (1997) Dredging
Brittle shear	$m < 7$	$m < 9$
Intermediate	$7 < m < 9$	$9 < m < 15$
Brittle tensile	$9 < m$	$15 < m$

Cools (1993) performed large-scale cutting experiments to measure the temperatures developing at the wear flat of a dredger cutting tooth during the cutting of rock, see figure 3.14 for the geometry of the chisel that was used. In these experiments, two 2.5 meter long blocks were cut, one block of limestone (UCS 25.2 MPa, BTS 1.5 MPa) and one block of sandstone (UCS 19.5 MPa, BTS 1.7 MPa). High normal forces were measured indicating that during cutting the normal stress beneath the machined wear flat amounted approx. 300 MPa in the limestone test, and approx. 130 MPa in the sandstone test. Tri-axial test results indicated that the brittle-ductile transition occurred at confining-maximum stress set ($\sigma_3 - \sigma_1$) of 23-96 MPa for the limestone and 41-119 MPa for the sandstone. Although the sandstone is more abrasive, the experiments of Cools show that the wear rate of the limestone cutting is significantly higher than that of the sandstone. He explains this by the increase in temperature of the tool during cutting, in the sandstone temperatures up to 550° C are measured, which is too low to cause thermal softening of the wear flat. Temperatures measured in the limestone reached up to 800° C, high enough to cause softening of the steel of the tool in a fraction of a mm thin zone at the wear flat, leading to higher wear rate. With respect to the rock, Cools and Verhoef both explain that this is caused by a large ductile crushed zone that occurs around the chisel, based on the large normal stresses that have been measured.

Majidi et al. (2011) performed drilling experiments with varying hydrostatic pressures and varying RPM on Carthage marble and Indiana limestone. They observed that in case of atmospheric pressure, above a critical RPM, the Carthage marble did not fail in a chipping mode, but the marble got crushed. In this crushed regime they also observed that the required cutting force is actually lower than in the chipping regime. When they increased the hydrostatic pressure, they noticed that the reduction in required cutting force with respect to lower RPM was lost. Their explanation for the disappearance of this reduction is that the friction of the crushed material along the bit face is higher due to the low pore pressures at the bit face. However, they do not give an explanation for the transition from chipping to crushed cutting. A possible explanation for the transition from chipping to crushed cutting could be that with increasing cutting velocity the rock behaves in an undrained fashion, leading to compaction weakening of the rock. Elevated hydrostatic pressure might prevent the compaction weakened material to dilate, resulting in no significant difference in failure mechanism with respect to low and high

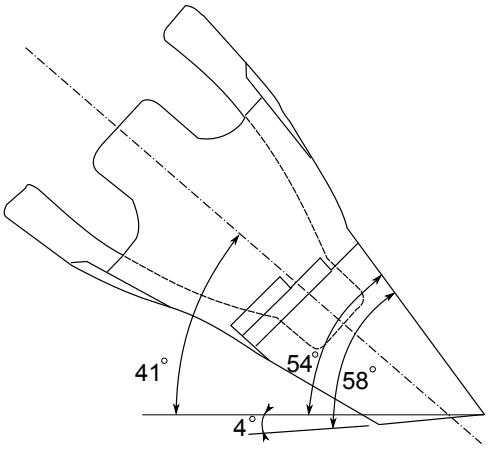

Figure 3.14: Chisel geometry as used in the experiments of Cools (1993).

velocity cutting.

3.1.6. Effect of cutting speed

Most of the experimental results for coal and rock cutting (in dry conditions) indicate that the cutting force is not affected by the cutting velocity in its practical range of applications (Potts and Shuttleworth, 1958; O'Dogherty and Burney, 1963; Roxborough, 1973). For example, tensile fractures in coal propagate at a speed of more than 500 m/s, which is more than 100 times faster than in practical rock cutting applications. However, it is noted that the cutting velocity can have a significant influence on the tool life, once the cutting velocity is above a critical velocity (Kenney and Johnson, 1976; Hurt and MacAndrew, 1985; von den Driesch, 1994).

Velocity effects might be of relevance when cutting saturated rock. van Kesteren (1995) describes two limit conditions, drained and undrained. In the drained conditions, flow of the pore fluid due to the pressure gradients in the pore fluid is possible without affecting the mechanical behavior of the rock skeleton. In the undrained case, deformation of the rock skeleton is that rapid that the pore fluid cannot flow sufficiently to relieve the pore fluid pressure gradients. As a result, the pore fluid contributes to the mechanical response of the rock skeleton. In a similar fashion to the rate dependent effects as described in section 2.3.2, van Kesteren (1995) distinguishes these two limit conditions based on the pore Peclet number, which shows a strong resemblance to the Debora number in equation (2.15). The pore Peclet number is given by

$$\zeta_{Pe} = \frac{v_c t_c}{D} = \frac{v_c t_c \eta \left(C_f - \alpha C_s + n\left(C_p - C_s\right)\right)}{\kappa} \tag{3.8}$$

According to van Kesteren (1995), the drained response is valid when $\zeta_{Pe} < 1$ and undrained behavior will occur when $\zeta_{Pe} > 10$. Detournay and Atkinson (2000) independently defined a similar dimensionless number to distinguish drained and

undrained behavior. However, the criteria they use, based on the form as in equation (3.8), are drained behavior when $\zeta_{Pe} < 0.004$ and undrained behavior when $\zeta_{Pe} > 40$. No direct comparison is made between the two criteria, the difference between the two criteria is likely due to the differences in cutting processes, i.e. a negative rake angle at small cutting depths in the case of Detournay and Atkinson (2000) and a positive rake angle at large cutting depths in the case of van Kesteren (1995).

In the experimental program that Van Kesteren uses as a basis for his theory, it is explained that the drained/undrained conditions are more directly concerned with the size of the crushed zone (Combinatie Speurwerk Baggertechniek, 1984). In the drained case, fluid can flow sufficiently away from the crushed zone and as a result the crushed zone shows significant compaction, resulting in a large crushed zone. On the other hand, in the undrained case the crushed zone is significantly smaller. This is because the fluid cannot flow sufficiently from the crushed zone and as a result the fluid in the crushed zone will be compressed, effectively increasing the bulk modulus of the rock in the crushed zone, resulting in a lower critical strain that is needed until chipping of the rock will occur.

Uittenbogaard (1980) and Luger (1981) performed indention tests with large cones on saturated rock to investigate the influence of a pore fluid (water) on rock deformation and its relation to velocity and length scales. The experiments are performed on St. Lieu limestone and WL II, an artificial type of rock developed by Delft Hydraulics for dredging research (Uittenbogaard, 1980; Luger, 1981; van Kesteren, 1995). The intrinsic permeability of the two rocks is respectively $3 \cdot 10^{-14}$ and 10^{-17} m^2. The cone has a top angle of 60° and is used to penetrate to depths up to 32 mm. The range of velocities is chosen in such a way that both drained and undrained cases are tested. At low velocity (0.01 m/s), the pore fluid is allowed to flow out of the porous system. In a zone around the cone the rock is compacted to a level that balances the penetrated volume of the cone. At a larger penetration rate, the penetrated volume cannot be balanced anymore by pure compaction of the rock matrix. As a result, the elevated fluid pressure in the rock will lead to shearing towards the free surface, eventually resulting in chips. At a velocity of 1 m/s the cone penetration occurs in an undrained regime. Due to the high porefluid pressures, the crushed rock is liquefied and squeezed out of the specimen along the cone face. See figure 3.15 for an overview of these failure phenomena.

Crack initiation and propagation are influenced by a pore fluid as well. The growth of the macro-crack and the micro-cracks in the shear zone is determined by the flow of the pore fluid towards the dilating zone. The resulting pressure gradient prohibits dilation and reduces the stress concentrations at the crack tips. Depending on the applied strain rate and (initial) pore pressure, the pore pressure gradient can result in a higher apparent shear or tensile strength.

3.1.7. Effect of hydrostatic pressure

Alvarez Grima et al. (2015) performed rock cutting experiments on saturated Savonnieres limestone at elevated hydrostatic pressures and large cutting depths (ca 20 mm). Their work focuses on the effect of a high hydrostatic pressure (to which they refer as hyperbaric pressure) and cutting velocity with respect to the cutting process

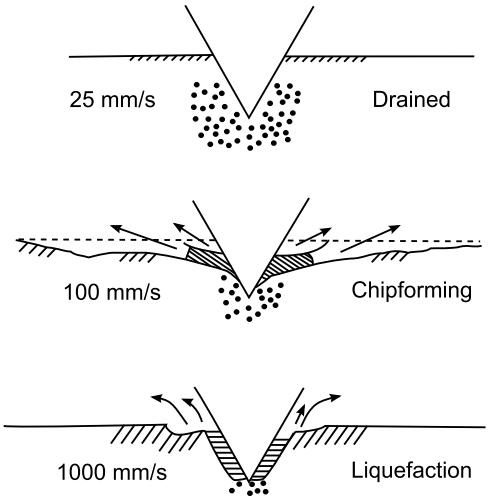

Figure 3.15: Failure mechanisms in cone indention tests in saturated st. Leu limestone ($\kappa = 3.6 \cdot 10^{-14}$ m^2), with varying penetration velocity, after van Kesteren (1995).

with a positive rake angle. In these experiments, the hydrostatic pressure ranges from 0-18 MPa, compared to the rock strengths σ_c = 7.92-10.64 MPa and σ_t = 0.86-1.13 MPa. The tests were executed in a hyperbaric tank and were performed on a 1:1 scale. In total, test results of fifteen experiments are presented, in which the hydrostatic pressure varies between 0, 1.5, 3, 6 and 18 MPa and the cutting velocity varies between 0.01, 0.2, 0.6, 1.2 and 2.0 m/s. The cutting experiments are performed with a positive rake angle of 22 ° with respect to the vertical axis, a wear angle of -10°, a chisel width of 21 mm and a cutting depth of 20 mm.

The average cutting force in horizontal direction with respect to hydrostatic pressure and cutting velocity is respectively shown in figures 3.16 and 3.17. The experimental results clearly show that with increasing hydrostatic pressure (water depth) the cutting forces increase as well. Besides that, the cutting force increases with cutting velocity as well. It seems that there are two regimes that can be distinguished based on these experiments, after p_h = 6 MPa, the cutting force seems to increase more rapidly for experiments with high cutting velocity. Alvarez Grima et al. (2015) explain that in rapid deformations the hydrostatic pressure acts as an additional resistance to deformation of the rock. The extent to which this can contribute to resist deformation of the rock is limited by cavitation (similar to the dilatancy hardening concept as explained in 2.3.2). It is expected that the size of the crushed zone increases, the shear failure at the edge of the crushed zone occurs later and that bifurcation of the shear crack towards a tensile crack is postponed. As a result, the cutting forces will increase and the average chip size will reduce. See figure 3.18 for a visualization of this explanation.

Particle size distributions of the debris and measurements of the groove that is created by a single cut support this theory. With an increase in hydrostatic pressure, the side breakout angle of the chips becomes more steep and the averaged cross-

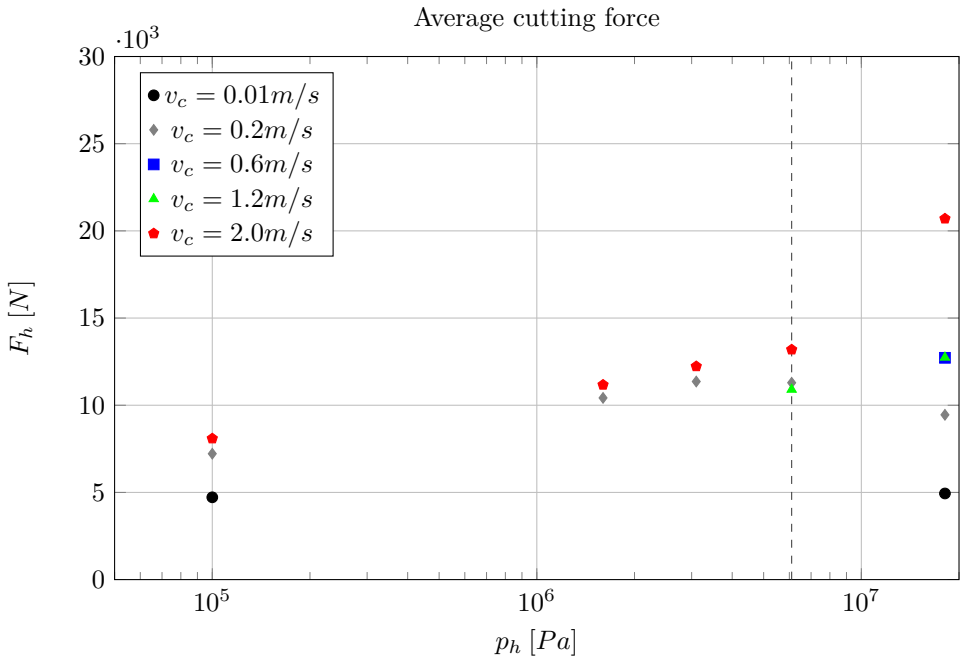

Figure 3.16: Average cutting force with respect to hydrostatic pressure, data from Alvarez Grima et al. (2015).

sectional area of the groove significantly reduces, as is already shown in figure 3.11 in section 3.1.4.

The drilling industry was, until the early 1950's, unaware of the effect of downhole pressure on the rock and thus the drilling process. Kuhne (1952) suggested that downhole pressure strengthens the rock and that a Mohr-Coulomb criterion may be used for taking the effect of strengthening into account. Through experiments, Cunningham and Eenink (1959) point out that it is not the effective stress that determines the strengthening of the rock matrix, but that the differential pressure (the difference between borehole pressure and the pore pressure). Furthermore, the experiments of Cunningham and Eenink (1959) also show that differential pressure had a more profound effect on the rate of penetration than would be expected by the increase in strength as a result of a Mohr-Coulomb material and that there had to be other mechanisms at work. Garnier and van Lingen (1958) suggested this to be the phenomenon of "chip hold down". Chip hold down refers to the force that the drilling fluid may exert on a cutting, or a bed of crushed material, due to the differential pressure.

Additionally, the industry also recognized that the permeability of the intact rock can have a significant influence on the differential pressure (Feenstra and van Leeuwen, 1964). When a drill bit shears rock, the rock will dilate, causing the pore

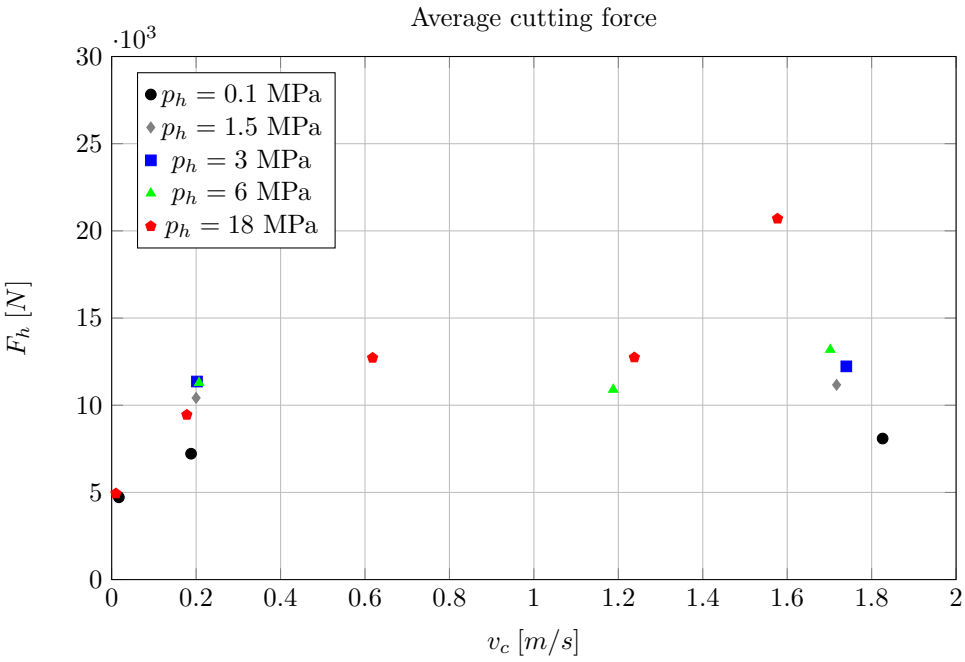

Figure 3.17: Average cutting force with respect to cutting velocity, data from Alvarez Grima et al. (2015).

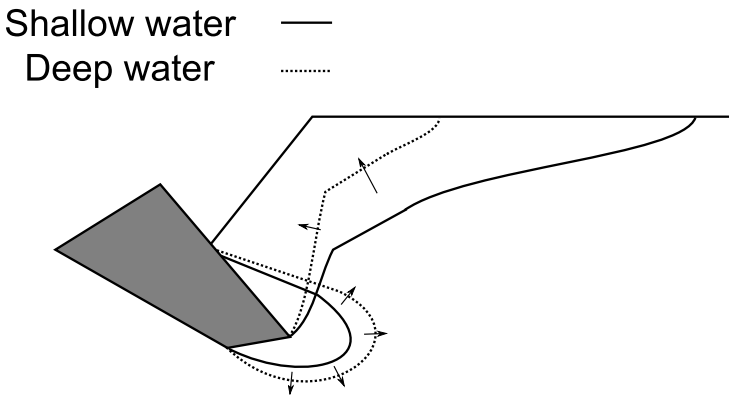

Figure 3.18: Trend of change in failure type with increasing water depth, after Alvarez Grima et al. (2015). An increase in water depth leads to larger cutting forces, larger crushed zone and smaller cuttings, resulting in a larger specific energy.

volume to increase. At low permeabilities this will cause a reduction of the pore pressure, that increases the differential pressure and ultimately strengthening the rock. This effect is documented in several laboratory experiments concerning the

cutting of shales, (Zijsling, 1987; Cook et al., 1991; Andersen and Azar, 1993; Gray-Stephens et al., 1994), as well as it is studied analytically, (Kolle, 1996; Detournay and Tan, 2002).

Full scale experiments of Black et al. (2008) and Judzis et al. (2009) have shown that the strengthening of the rock due to shear dilation only partly explains the reduction in efficiency and rate of penetration (ROP) when cutting rock under pressure. In the experiments of Judzis et al. (2009) a significant reduction in the penetration rate is noted. They explain that this is due to the unproductive work that is done on the crushed material that is held in place on the hole bottom by the local differential pressures. This effect is also known as a filter-cake, which acts as a layer of lower permeability, restricting the inflow of drilling fluid into the virgin rock. As a result, the pressure difference between the bottomhole pressure and the pore pressure remains larger, and thus requires more energy to actually cut a second time through a completely disintegrated rock.

In drilling experiments on Mancos shale, Zijsling (1987) observes that the cutting force is proportional to the total bottomhole pressure. Furthermore, the conditioning pressures do not have a significant effect on the cutting forces, implying that the bottomhole pressure rather than the overbalance (and thus the pore pressure level in the sample) governs the cutting process of a PDC in Mancos shale, see figure 3.19. In similar tests on Pierre shale, Zijsling observes a significant effect of the conditioning process of the shale samples on the cutting forces, see figure 3.20. The effect of the total bottomhole pressure on the cutting process is apparent at pressure levels in excess of 20 MPa, at which the cutting forces no longer increase with increasing total bottomhole pressure. Zijsling gives two arguments that can explain the lower effect of bottomhole pressure on the Pierre shale samples. First of all, it is expected that it has a less pronounced effect of dilation during shearing due to its higher porosity. Secondly, the dilation is governed by relatively weak clay particles sliding across each other. These particles will fail if the contact stress, which depends on the bottomhole pressure, exceeds the strength of the particles. As a result, the skeleton fails and the cavitation limit is not reached, thus a lower pressure difference needs to be overcome to cut through the rock.

To analyze the rock-drilling process from an energy point of view, Simon(1963) and Teale (1965) use the concept of mechanical specific energy E_{sp}. In their experiments they find that the E_{sp} for drilling rocks under atmospheric conditions strongly correlates with the UCS of the rock. Pessier and Fear (1992) questioned whether the same comparison could be done under pressurized conditions using the confined compressive strength instead of the UCS. However, in all their experiments, even under ideal hydraulic conditions, the E_{sp} they have measured was much higher than the confined compressive strength of that rock under the same confining pressures.

3.1.8. Identification of other parameters

Mishnaevsky Jr (1995) states that probably up to 90 % of the energy for cutting is spent in the crushing of the rock near tool tip. Analysis of Mishnaevsky also shows that the confining stresses near the tool tip can be very high, high enough to exceed the brittle-ductile transition in rock. This explains why rock can be cut in a

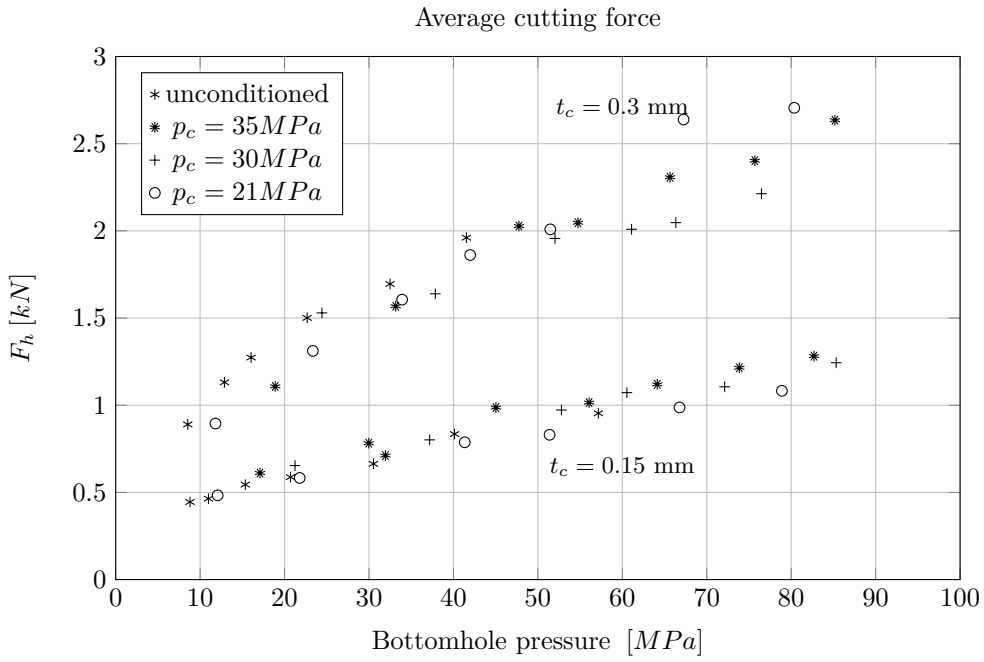

Figure 3.19: Cutting forces in Mancos shale with respect to bottomhole pressure and borehole depth, data from Zijsling (1987).

ductile mode. Based on rock cutting experiments, Chiaia (2001) concludes that the cutting performance of a tool can be significantly improved by reducing the crushing component and enhancing the chipping ability of the tools.

On the basis of test results, the ratio of peak to mean cutting force is reported as 5-7 in coal cutting (Pomeroy, 1963). In rock cutting, more dispersed values are reported, 1.4-7.7 for the wedge shaped bit (Muirhead and Glossop, 1968; Roxborough, 1973) and 1.6-3.0 for pick points (Kenney and Johnson, 1976; Hurt, 1980; Goktan and Gunes, 2005)

3.2. Analytic rock cutting models

Various rock cutting models exist in literature. An overview of the existing rock cutting models will be presented. These models can be distinguished into two groups, i.e. analytic and semi-empirical. Due to the different assumptions and parameters, a direct comparison between these models is difficult. Several dominating failure processes are identified (Helmons and Miedema, 2013), as is already shown in figure 3.2. In general a distinction can be made between continuous and discontinuous failure mechanisms. In a continuous failure, the cut material moves as a plastic flow along the tool (or it can ball up over a portion of the tool length). This typically occurs for cutting in cohesionless materials (e.g. sand, Miedema (1987)) and it can

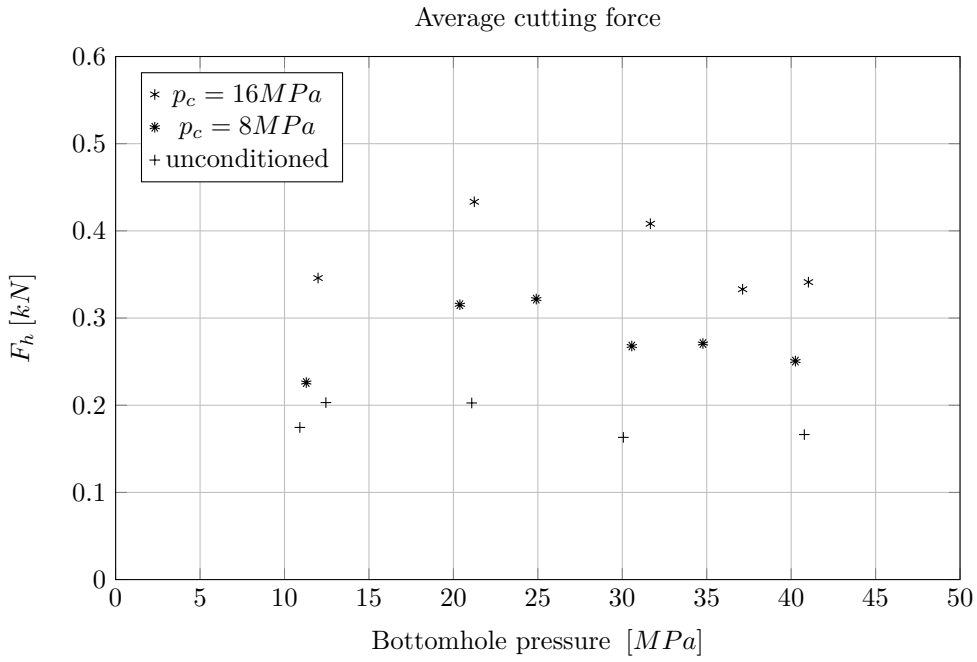

Figure 3.20: Cutting forces in Pierre shale with respect to bottomhole pressure and borehole depth at cutting depth of 0.3 mm, data from Zijsling (1987).

occur in drilling processes, as is the case in the experiments of Zijsling (1987) on Mancos and Pierre shale. The other group of cutting processes is based on discontinuous cutting processes. Within this group a distinction can be made between tensile and shear dominated failure processes. These failure mechanisms are used for the basis of the analytical models.

In literature, various analytic rock cutting models exist. Due to the complexity of the rock cutting process, these analytical models are often limited to a certain dominant failure mechanism. Note that the way the models are described here might differ from the exact form that is described in the original work of the authors. Here all models are adjusted to be applicable in the same frame of reference, that is with respect to rake angle, compressive forces and stresses are positive, tensile forces are negative.

Evans

The cutting model of Evans (1965) is specifically for tensile failure dominated cutting processes. His model is based on the following assumptions:

- The process is two dimensional.
- No velocity effects are considered.

- Movement is in horizontal direction.
- The crack to separate the chip occurs instantly.
- The penetration of the wedge is small compared to cutting depth.

A schematic representation of Evans (1965) model is given in figure 3.21. It is assumed that along the curve C-D, tensile strength of the rock occurs simultaneously. The exact shape of C-D is determined by a minimizing the required energy to generate the chip with respect to the shear angle β. In the original model assumes symmetry, resulting in zero total vertical cutting force. The total horizontal cutting force and the vertical cutting force per side of the tool are given by respectively

$$F_{h,Evans} = \sigma_t t_c w \frac{2\sin(\theta+\delta)}{1-\sin(\theta+\delta)} \tag{3.9}$$

$$F_{v,Evans} = \sigma_t t_c w \frac{\cos(\theta+\delta)}{1-\sin(\theta+\delta)} \tag{3.10}$$

with tensile strength σ_t, cutting depth t_c, cutting width w, half top angle of the tool θ and external friction angle (tool-rock) δ.

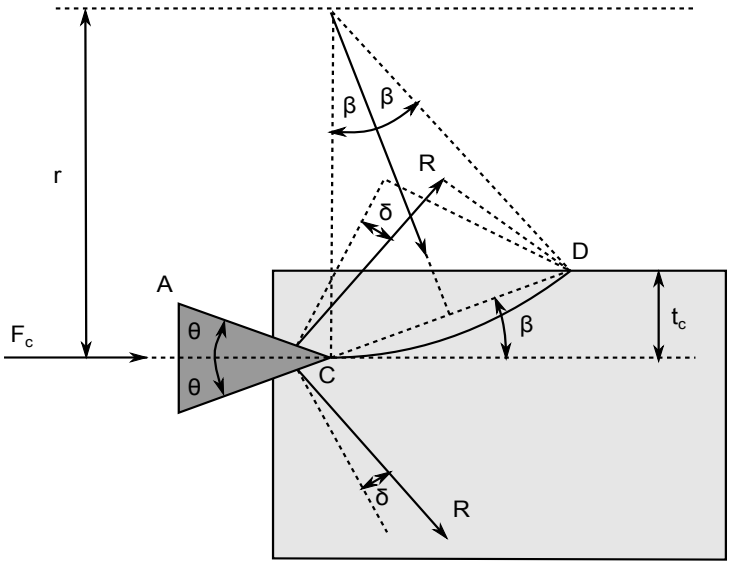

Figure 3.21: Rock cutting model of Evans (1965) for tensile chipping.

Evans (1984) presents an improvement of the cutting model for the use of conical pick points. In the case of conical picks, the assumption of a 2D model is not valid anymore. Total cutting force

$$F_{c,Evans-pickpoint} = \frac{16\pi\sigma_t^2 t_c^2}{\sigma_c \cos^2(\theta)} \tag{3.11}$$

Goktan (1997) made some suggestions to improve the theory of Evans (1984), resulting in a cutting force calculated by

$$F_{c,Evans-Goktan} = \frac{4\pi\sigma_t t_c^2 \sin^2(\theta+\delta)}{\cos(\theta+\delta)} \tag{3.12}$$

resulting in elimination of one of the shortcomings identified by Evans himself, that the cutting force does not reduce to zero when $\theta = 0°$ for a frictionless tool ($\delta = 0°$) and Goktan eliminated the compressive strength in the model for tensile failures, see equation (3.11). A semi-empirical model is derived by Goktan and Gunes (2005), by fitting equation (3.12) to experimental data, resulting in

$$F_{c,Goktan} = \frac{12\pi\sigma_t t_c^2 \sin^2\left(45-\frac{\alpha}{2}+\delta\right)}{\cos\left(45-\frac{\alpha}{2}+\delta\right)} \tag{3.13}$$

Furthermore, Goktan found that the mean cutting force is about one third of the peak cutting force as defined in equation (3.13). A similar observation is made by Ranman (1985).

Vlasblom (in (Miedema, 2014)) presents an extension of the Evans model for the use of worn chisels, by assuming that the tool can enter the rock under an angle ε, here chosen to have the same value as θ, and that it has a wear flat, as presented in figure 3.22. Here the direction of the cutting velocity is still horizontal. The cutting force, decomposed in horizontal and vertical components, are respectively given by

$$F_{h,Evans-wearflat} = \sigma_t t_c w \left(\frac{2\sin(\theta+\delta)\cos(\theta)+\cos(\delta)}{1-\sin(2\theta+\delta)}\right) \tag{3.14}$$

$$F_{v,Evans-wearflat} = \sigma_t t_c w \left(\frac{2\sin(\theta+\delta)\sin(\theta)+\sin(\delta)}{1-\sin(2\theta+\delta)}\right) \tag{3.15}$$

Merchant

Most of the (semi-)analytical rock cutting models are adaptations of the Merchant (1945) cutting model for metals. The model is based on plastic deformation of the metal and a continuous chip formation. In this theory, and in the extensions to this theory, the following assumptions are made

- Tool width is much larger than the depth of the cut, i.e. plane strain.
- Tool moves with constant velocity over a constant depth.

An overview of the geometry and parameters of the Merchant cutting model and its corresponding extensions is presented in figure 3.23.

Furthermore, the following assumptions are specifically for Merchant's model

- Constant stress state.
- Coulomb friction acts along tool-chip surface.
- Plastic yield of the metal is based on Mohr-Coulomb criterion.

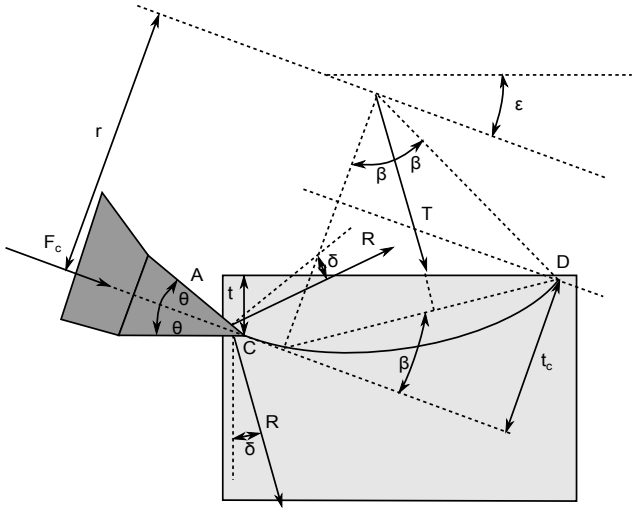

Figure 3.22: Extension of Evans' model with wear flat and tool entrance under an angle, according to Miedema (2014).

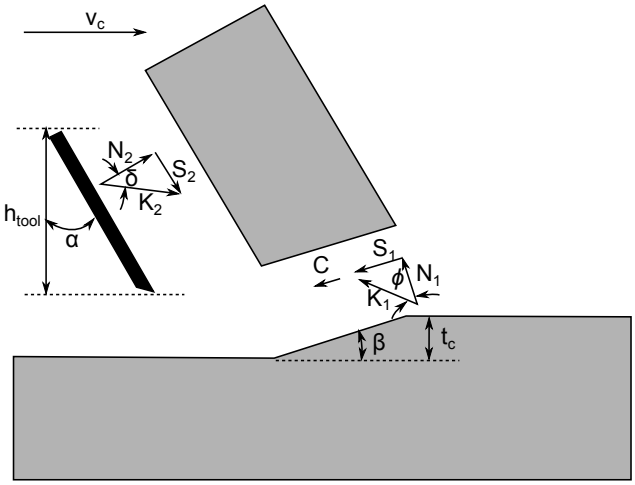

Figure 3.23: Model definition of Merchant (1945), combined with the extensions based on Miedema's model.

- Failure stress acts along the whole shear plane.

Based on these assumptions and through equilibrium of forces, the cutting force is derived as

$$F_{h,Merchant} = \tau_0 t_c w \frac{\cos(\alpha - \delta)}{\sin(\beta)\cos(\alpha - \beta - \delta)} \tag{3.16}$$

$$F_{v,Merchant} = \tau_0 t_c w \frac{\cos(\alpha - \delta)}{\sin(\beta)\cos(\alpha - \beta - \delta)} \frac{1}{\tan(\delta - \alpha)} \tag{3.17}$$

with yield stress in shear τ_0, rake angle α and shear angle β. Note that the shear angle β is a parameter that is not directly known. In order to obtain β, the minimum energy principle is used. Minimization of the cutting force with respect to β gives

$$\beta = \frac{\pi}{4} + \frac{\alpha - \delta}{2} \tag{3.18}$$

By determining the minimum of the cutting force with respect to β, one finds meaning that the minimum in cutting force is determined with respect to β.

Nishimatsu

The model of Nishimatsu (1972) is specifically for brittle shear failure dominated rock cutting. This model is based on the Merchant model, with the following assumptions:

- Brittle shear failure occurs according to a linear Mohr envelope.
- Failure through indention of the tool is neglected, i.e. no crushed zone.
- Stress distribution along the shear plane distributed as $\sigma = \sigma_0 \left(\frac{t_c}{\sin(\beta)} - \lambda \right)^n$. Where n represents a stress distribution factor, λ is the distance from tool tip along the shear plane to the surface.

A graphical representation of the geometry used in Nishimatsu's model is shown in figure 3.23 as well. The cutting force according to the Nishimatsu model, decomposed in horizontal and vertical component, respectively given by

$$F_{h,Nishimatsu} = \frac{1}{1+n} \frac{2ct_c w \cos(\phi) \cos(\alpha - \delta)}{1 + \sin(\alpha - \delta - \phi)} \tag{3.19}$$

$$F_{v,Nishimatsu} = \frac{1}{1+n} \frac{2ct_c w \cos(\phi) \sin(\alpha - \delta)}{1 + \sin(\alpha - \delta - \phi)} \tag{3.20}$$

where n stands for the stress distribution along the shear plane. Nishimatsu states that n depends on the rake angle, based on the empirical relation

$$n = 11.3 - 0.18\alpha \tag{3.21}$$

This empirical relation is based on experiments of Nishimatsu (1972) in the range of $\alpha = 10 - 40°$. Note that beyond this range, the validity of this equation can be questioned, especially for rake angles larger than 68° where the sign of n changes. In that case, the cutting force changes sign as well and unrealistic results will occur.

Detournay and Atkinson

In the case of drilling, the problem definition differs from the models described before. Detournay and Atkinson (2000) derive a model based on the facts that the rock now is saturated with a pore fluid at p_0, the surface of the rock is exposed to a constant hydrostatic pressure p_h, caused by mud pressure, and the rock is considered to be shear dilatant. Detournay and Atkinson introduce additional assumptions to extend Merchant's model:

- The effective normal stress and $(\sigma_n - p)$ and the shear stress σ_s across the failure plane satisfy the Mohr-Coulomb criterion

$$|\sigma_s| = c + (\sigma_n - p)\tan\phi \tag{3.22}$$

- The effective normal stress and shear stress across across the tool-rock interface are related by the frictional law

$$|\sigma_s| = (\sigma_n - p)\tan\delta \tag{3.23}$$

  where δ is the contact friction angle.

- The interstitial fluid pressure along the cutter/rock interface is equal to p_h
- The pore pressure variation in the intact rock is governed by pore pressure diffusion equation.

Based on these assumptions, the cutting forces are given by

$$F_{h,Detournay} = t_c w \frac{2\cos\phi\cos(\delta-\alpha)}{1-\cos(\phi+\delta-\alpha)}\lambda\left(c + (p_m - p_b)\tan\phi\right) \tag{3.24}$$

$$F_{v,Detournay} = t_c w \frac{2\cos\phi\sin(\delta-\alpha)}{1-\cos(\phi+\delta-\alpha)}\lambda\left(c + (p_m - p_b)\tan\phi\right) \tag{3.25}$$

with cavitating limit factor λ. In the case of a fully cavitating cutting process $\lambda = 1$, in the limit that the cutting process is infinitely slow, the fluid pressure component does not contribute at all to the cutting force, and thus in such a case $\lambda = 0$. The corresponding angle of the shear plane with respect to the direction of motion of the cutter is given by (Detournay and Atkinson, 2000)

$$\beta = \frac{\pi}{4} - \frac{\alpha + \phi + \delta}{2} \tag{3.26}$$

The expression for β indicates that the Merchant failure mechanism can only be constructed when

$$\alpha < \frac{\pi}{2} - (\phi + \delta) \tag{3.27}$$

When the rake angle approaches the upper bound given by (3.27), another flow mechanism may occur. This flow mechanism involves the presence of a wedge of material sticking to the cutting face (Detournay and Defourny, 1992). They suggest the existence of three flow regimes (all considering negative rake angles): forward flow at small rake angles (sub-vertical cutter), flow with a build-up edge at intermediate rake angles and backward flow at large rake angles (sub-horizontal). In the experiments of Zijsling (1984); Adachi et al. (1996) a built-up edge of crushed material in front of the PDC-cutter is observed, supporting the claims of Detournay and Defourny (1992).

The pressure drop that can be attained in the dilating shear zone depends on the pore Peclet number (as is discussed in 3.1.6). At low pore Peclet numbers the pressure difference will be insignificantly small, resulting in a simplified form of equations (3.24) and (3.25), which is similar to Nishimatsu's model.

Miedema

The cutting model of Miedema (2014) finds its origin as an adaptation of Merchant's model to be applicable to the cutting of (saturated) sand (Miedema, 1987). Later on, Miedema extended this model to be applicable to the cutting of clay and rock by incorporating brittle tensile and brittle shear failure criteria in the cutting model. Furthermore, Miedema's model has been extended to incorporate effects of hydrostatic pressure and to cases where the crushed zone reaches the surface of the rock (drilling). Miedema (2014) gives an extensive derivation for all the different cases and adjustments, here only the most relevant aspects of this model are presented. Besides the basic assumptions of Merchant's model, the following additional assumptions are made:

- Failure occurs instantly.
- Hydrostatic pressure (water depth) and pore pressure of virgin rock are in equilibrium.
- The rock is shear-dilatant.
- Two zones with underpressure are assumed 1) along the shear zone between the cut layer and the virgin rock and 2) between the cut layer and the tool.

The model follows a similar structure for each failure mechanism, the forces as depicted in figure 3.23 acting on the cut material and through that on the seabed and the tool are calculated and again equilibrium of forces is assumed. The resultant force between the cut material and the tool K_2 is given by

$$K_2 = \frac{W_2 \cos(\alpha - \beta - \phi) + W_1 \sin(\phi) + C \cos(\phi)}{\cos(\alpha - \beta - \phi - \delta)} \tag{3.28}$$

with pore pressure force acting along the shear plane W_1, pore pressure force acting along the tool W_2, cohesive force C. The maximum pore pressure forces for the cavitating (maximum) and non-cavitating are respectively given by

$$W_1 = \frac{\rho_f g (z + 10) t_c w}{\sin(\beta)} \quad \text{or} \quad W_1 = \frac{p_{1m} t_c w}{\sin(\beta)} \tag{3.29}$$

$$W_2 = \frac{\rho_f g (z + 10) h_{tool} w}{\cos(\alpha)} \quad \text{or} \quad W_2 = \frac{p_{2m} h_{tool} w}{\cos(\alpha)} \tag{3.30}$$

and the cohesive force is given by

$$C = \frac{c t_c w}{\sin(\beta)} \tag{3.31}$$

resulting in the total cutting force given by

This results in the horizontal and vertical cutting forces, respectively given by

$$F_{h,Miedema} = -W_2 \cos(\alpha) + K_2 \cos(\alpha - \delta) \tag{3.32}$$

$$F_{v,Miedema} = -W_2 \sin(\alpha) + K_2 \sin(\alpha - \delta) \tag{3.33}$$

Note that in shallow water conditions (low hydrostatic pressure with respect to the strength of the rock), the pore pressure terms W_1 and W_2 are negligible. However, the cutting model underestimates the cutting forces measured in experiments of Alvarez Grima et al. (2015) significantly. Therefore an empirical correction factor is used, which is of the form

$$c_{corr} = \left(1 - \frac{c_1}{z + 10}\right)\left(1 + \frac{c_2}{z + 10 + c_3}\right) \tag{3.34}$$

with values $c_1 = 3.33$, $c_2 = 200$ and $c_3 = 400$. Care must be taken when using this correction, as it is only based on one set of experiments. Additionally, the correction factor they use is to correct for the upper limit (with respect to cutting velocity) of the mean rock cutting forces, while the model derivation is based on the peak cutting forces. Furthermore, it can be argued whether the pore pressure force W_2 is actually valid in the case of brittle cutting processes. The debris of the experiments of Alvarez Grima et al. (2015) still show rather large chips (up to several cm's in size) even for cutting experiments at $p_h = 18$ MPa. How the debris moves along the tool during cutting is unclear, since it was not possible to visualize due to the pressure tank.

3.3. Discussion rock cutting models

The analytical rock cutting models can be used as a means to design and engineer the equipment used to cut through rock. However, one must be careful when using these models because of the simplifications that are made and the limited range of applicability of these models. Basically all of the described models have similar problems, that to some extent can be corrected for.

First of all, all the models that are applied for brittle rock failure (both shear and tensile) can only be used to determine the peak value of the cutting forces, not the mean cutting force. Furthermore, all models essentially assume 2D cutting processes, while in practice rock cutting is almost always a 3D process. In 2D, the cut layer can only move directly along the tool (or curling/balling up might occur, (Zijsling, 1987; Miedema and Zijsling, 2012)), neglecting the possibilities of sideways movement of the cut material. Furthermore, it can be argued whether the assumption that the debris acts as a plastic layer moving along the tool surface can be true. The assumption could be valid, because of the crushed material that is generated in the crushed zone is forced to move along the tool surface. However, it might as well be the case that the crushed material is not forced along the tool surface but that it moves along with the generated chips. Unfortunately, such observations are not described in the work of Alvarez Grima et al. (2015). Furthermore, it is observed that the size of the crushed zone significantly differs in 2D tile cutting experiments (Uittenbogaard, 1980; Luger, 1981) compared to 3D cutting experiments (Combinatie Speurwerk Baggertechniek, 1984). Additionally, the break-out shape of the groove cut by one chisel and the beneficiary effects of tool spacing are not considered.

All the presented rock cutting models are linear with respect to the cutting depth, while in experiments of Richard et al. (1998), Liefferink (2013) and Motzheim (2016) a transition is observed, at small cutting depths the cutting force scales as $F_c \propto t_c$, while for larger cutting depths the cutting force scales according to $F_c \propto \sqrt{t_c}$.

A large amount of the equipment used in dredging and seabed mining is based on circular motion (e.g. cutterhead, roadheader, drumcutter), while the cutting models that are used for engineering of the equipment are based on linear cutting models. The movement from a small cutting depth towards a large cutting depth or vice versa might result in different behavior than that would be expected of the linear cutting models because the assumption that the velocity of the tool is parallel to the surface of the rock is not met, it actually changes during the movement of the tool. Besides the lack of capturing the brittle-ductile transition with cutting depth, differences might occur as well in e.g. friction, specific energy, wear rate.

Basically all analytic cutting models are based on peak force estimations, while in practice averaged cutting forces are of interest as well. Average to peak cutting forces are thus far estimated based on empiricism. Besides, all models are based on constant parameters over time and assume rigid body movements of the tool. As a result, effects like oscillations on the cutting motion (e.g. percussion) or inertia effects of the complete cutting tool are neglected.

3.4. Conclusions

It is shown that the cutting of rock is a complex process. All failure types along the failure envelope can occur in a single cut. Many parameters can have a significant influence on the cutting process itself, e.g. rake angle, cutting depth, rock properties, ambient conditions, pore fluid, tool geometry, velocity.

The (empirical-)analytical models can be a powerful tool to aid the design of the rock cutting equipment. However, most of the models require the failure process to be identified a priori, while it is desired to have this as a result rather than an input parameter. If one wants to be able to investigate the effect of hydrostatic pressure and pore fluid pressure on the rock cutting process, beyond the level of rock cutting forces, a more detailed approach compared to the presented rock cutting models is necessary. Furthermore, variations in time like inertia, oscillations and a more complex shape of the cutting tool are not captured with these cutting models.

Numerical techniques are powerful tools to aid in the research of the rock cutting process. What simulation techniques already exist and have been used to simulate rock cutting processes, as well as the modeling approach that is used within this dissertation, will be discussed in the next chapter.

4

Modeling Approach

"If the facts don't fit the theory, change the facts."

Albert Einstein

As presented in previous chapters, the combination of the physical phenomena, together with the fact that the whole range of failure mechanisms occurs in the cutting process, make it that the cutting of fluid saturated rock is a complex process to model and simulate. At the start of this research, there was no methodology available that was sufficiently capable to model the cutting of saturated rock. First an overview is presented on the state-of-the-art of rock cutting simulations and what attempts have been made to incorporate fluid pressure effects in rock deformations. Furthermore the ideas and the approach on how the rock cutting process is modeled within this research is presented.

Simulating the rock cutting process of a single tool requires a model that is capable of capturing the transition from intact rock through (micro-)cracking to fragmented rock, ultimately leading to a granular flow. Additionally, the failure mechanisms that need to be considered should be able to cover the whole failure envelope, ranging from the brittle tensile and shear fractures towards cataclastic failure.

4.1. Numerical modeling of rock cutting

In general, a distinction can be made between continuum based and discontinuum based modeling techniques.

4.1.1. Continuum based modeling

Several attempts have been made to model the rock cutting process with the use of a continuum based method, e.g. the Finite Element Method (FEM), e.g. (van Kesteren, 1995; Liu et al., 2002) . However, in the case that such a methodology is used, several problems arise. First of all, for continuum based problems one needs to use a set of equations that is capable of describing the desired physical model. The more complex the physical problem is, the more difficult it will be to find, derive and solve the required set of equations. In the case of rock cutting, it is especially difficult because it has to deal with the whole range from intact rock to granular flow, also combined with fluid pressure.

Secondly, mesh-based continuum methods, like FEM, have difficulties with the large deformations that are applied in the cutting process. In the case of brittle failures it requires that the elements through which the cracks occur can be split. If too much distortion is applied to the underlying mesh, remeshing might become necessary. For that reason, various researches avoid this problem by investigating the chip forming process until the chip has formed, stopping the simulations when remeshing becomes a necessity (van Kesteren, 1995; Liu et al., 2002; Yu, 2005). An option to allow the simulations to continue beyond this point would be to use an element deletion routine (Cho et al., 2010; Pittino et al., 2015), i.e. when tensile failure occurs in an element, it will be immediately eliminated. When modeling the cutting process involved in a single cutter such a simplification is prone to modeling errors. The generated debris is completely neglected while its presence can result in significant stresses. Another disadvantage is that mass is not conserved.

A different solution could be to use remeshing techniques based on the combination of discrete and finite elements, (Mahabadi et al., 2004; Oñate and Rojek, 2004; Zárate and Oñate, 2015). In such an approach, finite elements are used to model the behavior of intact rock. The nodes of the elements are treated as discrete elements, which become active when a crack occurs through the element boundary. This way it is possible to allow large deformations of the mesh, by making adapting the discretisation from a continuum base to a discontinuum base.

4.1.2. Discontinuum based modeling

The discrete element method (DEM) is often used to simulate the rock cutting process of a single tooth bit, e.g. (Huang, 1999; Lei and Kaitkay, 2003; Rojek et al., 2011). The unique feature of the DEM is that it can be used to model solids as a collection of particles consisting of arbitrary shapes (most often simple shapes like discs, spheres and polygons are used because of their mathematical simplicity). The particles can move independently from one another and they interact through the contacts or interfaces between them. In contrast to the continuum based methods, the DEM is not limited to specific failure modes, it can deal with cataclastic damage and brittle failure mechanisms simultaneously. These phenomena occur as a generic consequence of the effects that occur on the micro-scale, being tensile and or shear failure, resulting in particle separation and sliding.

The use of the DEM in geomechanics originates from the study of granular materials (Cundall and Strack, 1979). Especially in the last decade, due to the increased computational power that is available, the interest in the DEM has increased. Nowadays it finds its use in a wide range of applications, e.g. granular flow (Guo and Curtis, 2015), solid-liquid mixtures (Robinson et al., 2014), pedestrian flows (Lohner et al., 2016) and rock failure (Potyondy, 2015). Various researchers have used the DEM to model tool-rock interactions, like indention and cutting. Interests in using DEM for rock cutting simulations started with the PhD thesis of Huang (1999), focusing on 2D simulations of rock indention and rock cutting tests. Especially within the last few years, the DEM has gained popularity to do rock cutting simulations, using it for a wide range of applications. A brief overview of the work that has been done is presented in table 4.1.

To summarize, the distinction between the continuum and discontinuum-based modeling approaches results in a shift in where the complexity of the modeling approaches will reside. For continuum based models the equations that need to be solved increase in complexity and have a rather simple geometry, while the opposite is true for the DEM. The physical models that are solved are simple on a microscopic level, but the complexity of the model comes from the complexity of the geometry. Furthermore, the cutting process concerns the transition from intact rock towards a discontinuous assembly of grains and chips. That is why a discontinuous approach is more favorable to adequately model the rock cutting process.

4.2. Hydromechanical coupling

The DEM has been useful to model tool-rock interactions, however, without considering fluid-pressure effects. Several approaches have been developed to incorporate, to some extent, fluid pressure effects in rock. The first group are methods that are based on a discontinuum approach by modeling the flow of the pore fluid along the element contacts/bonds (Shimizu et al., 2011; Zhang and Wong, 2013; Wang et al., 2014). The aperture between two neighboring particles is used to determine the width of the pore channel, allowing to adapt to a change in permeability due to the occurrence of opening (micro-)cracks, see figure 4.1 for an overview. These methods are often used to model the hydraulic fracturing process, with typically mode-I (tensile) failures as the dominant failure phenomena. In case of large defor-

Table 4.1: Research on rock cutting simulations using DEM.

Publication	Application	Special interests
Huang (1999)	PDC bit, wedge	2D, indention and cutting tests
Lei and Kaitkay (2003)	PDC bit, drilling	2D, confining stress on top layer
Ledgerwood III (2007)	PDC bit, drilling	2D, confining stress on top layer
Alvarez Grima et al. (2011)	pick point, DSM	2D, confining stress on top layer
Moon and Oh (2011)	disc cutter, TBM	2D, tool spacing
Rojek et al. (2011)	pick point, roadheader	2D/3D, comparison differences between 2D and 3D
Su and Akcin (2011)	PDC bit	3D
Huang et al. (2013)	PDC bit	2D, improved on work of Huang (1999)
Huang and Detournay (2013)	wedge indention	2D, improved on work of Huang (1999)
Mendoza Rizo (2013)	PDC bit, drilling	2D, confining stress on top layer, crushable particles
Carrapatoso et al. (2014)	PDC bit, drilling	3D, effect of chamfer, sharp vs blunt tool
Rojek (2014)	pick point, dredging	2D, heat distribution and wear rate analysis
van Wyk et al. (2014)	PDC bit, drilling	3D, tribology effects
Tropin et al. (2014)	PDC bit, drilling	3D, confining stress on top layer
He and Xu (2015)	PDC bit, drilling	2D, comparison single particles and clustered particles, brittle-ductile transition based on cutting depth
Liu et al. (2015)	disc cutter, TBM	2D, effect of tool spacing and confining stress
Li et al. (2016)	disc cutter, TBM	2D, effect of cutting velocity and confining stress

mations, occurrence of new contacts or significant distortion of the contact network (i.e. "mesh") of the fluid, it will be necessary to remesh the discretisation of the fluid phase. This will be problematic for the cases concerning the transition from intact

rock to moving fragments of rock, as remeshing will be too frequently necessary.

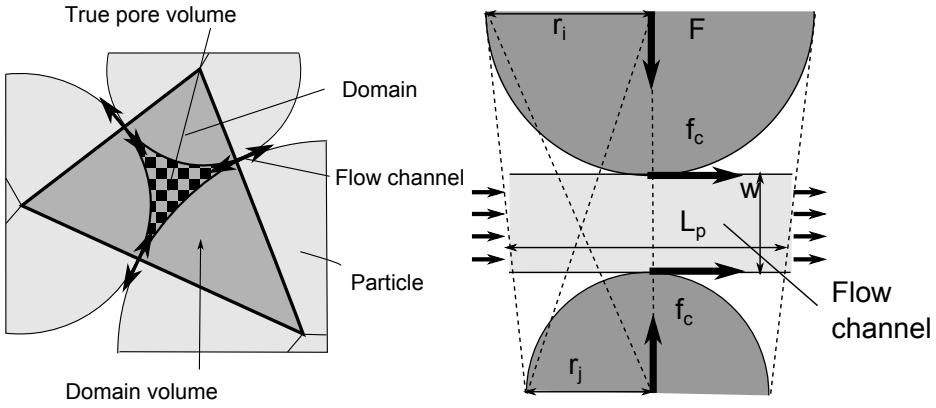

(a) Channel-domain model (b) Fluid flow in a channel

Figure 4.1: Pore channel model, taken from Shimizu et al. (2011).

The second group of hydro-mechanical coupling methods are those that apply an adaptive confining pressure boundary condition (Lei and Kaitkay, 2003; Ledgerwood III, 2007; Mendoza Rizo, 2013; Tropin et al., 2014). It is considered adaptive in the sense that it allows the boundaries to deform, in contrast to the servo-controlled walls that are sometimes used in bi/tri-axial tests (Potyondy and Cundall, 2004). Various algorithms exist to determine which particles are part of the free surface and which are not. Lei and Kaitkay (2003); Ledgerwood III (2007); Alvarez Grima et al. (2011) all identify the boundary particles based on the chain of contacting particles along the boundary, see figure 4.2. Starting with particles A and B which are located based on a geometric criteria. Then the algorithm works counterclockwise from particle B to locate all the other boundary particles, moving on to the particle that makes the smallest angle with the vector of BA is identified as a boundary particle, etc.

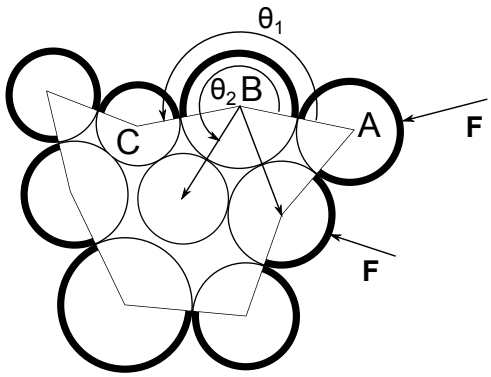

Figure 4.2: Boundary detection method as suggested by Lei and Kaitkay (2003).

In the approach of Mendoza Rizo (2013) the boundary is identified by an algorithm that loops over through the particles within a window and identifies the nearest particle with respect to a frame of reference, see figure 4.3. A somewhat similar approach is used by Tropin et al. (2014) in what they call the shining light method. Each particle that can be directly 'seen' from a plane is identified as a boundary particle. Because such a method is only applicable to a static boundary, they also make use of an α-shape algorithm based on Delauny triangulation, which is based on the work of Edelsbrunner and Mücke (1994).

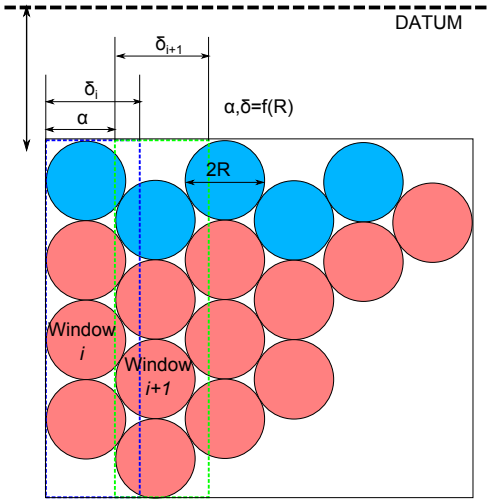

Figure 4.3: Boundary detection method as suggested by Mendoza Rizo (2013).

In all of the mentioned boundary detection methods, a force is applied to each boundary particle based on the confining stress and its weighted contribution to the boundary. Although these approaches mimic the effect of a confining stress, they do not consider the pores of the rock to be filled with a fluid.

DEM-SP coupling

In this research, the DEM is extended with fluid pressure effects. These fluid effects are based on a Smoothed Particle (SP) approach, which is a meshless Lagrangian particle based method used to solve continuum based problems. SP finds its origin in astrophysical problems Lucy (1977), nowadays it is used in many fields, e.g. hydrodynamics (SPH) Monaghan (2012), applied mechanics (SPAM) Hoover et al. (1994). Various researchers have used the combination of DEM and SP techniques in the field of rock mechanics. These can be distinguished into two groups.

The first group of methodologies are those in which DEM and SP are used to model the two phases fully separated, particles represent either solid or fluid (Lagrangian-Lagrangian model description). Such methods are used for problems like hydraulic fracturing Komoróczi et al. (2013), rock blasting Fakhimi and Lanari (2014), boudinage Komoróczi et al. (2013). Besides, such a two phase description for fluid rock interactions, it is often used in modeling of multi-phase flows and/or

fluid structure interactions as well, for example Potapov et al. (2001); Cleary et al. (2006); Sun et al. (2013).

The other group of methods are based on methods that treat the DEM and SP particles in a co-located fashion, meaning that the properties of both fluid and solid phases are based on the same particles and these properties are transported with the same particles as well. Thus far, the use of these kind of approaches is rather limited due to a strong but necessary assumption, transport of the two phases should be almost similar. However, it can be used to relate the discontinuous properties of DEM to a continuum field, e.g. heat, stress. A strongly simplified approach similar to SP that describes the stress state of DEM particles is used in SDEM (stress-based DEM) (Egholm, 2007; Egholm et al., 2007). In SDEM, the calculated stress is used as a failure criterion for the DEM. SDEM is too simplified in the sense of number of neighboring particles, only the direct neighbors are considered, and the interpolation kernels that are used are insufficient to properly model a continuum. As a result, their application is limited to an interpolation scheme for the DEM.

4.3. Modeling Approach

As presented in section 4.1.2, the DEM is a powerful method that is well capable and accepted to model the cutting of dry rock and therefore the DEM can be used as a basis for modeling the cutting of saturated rock. The large deformations of the rock require to model the fluid effects on a continuum level to avoid expensive remeshing of the fluid phase. The Smoothed Particle method is a particle based method that is used to solve problems based on a continuum field. That way, the SP can be used to interpret the discontinuous properties of the DEM to a continuum level.

The research objective of this dissertation, modeling the cutting of rock for shallow and deep water applications, is a research area with a rather small academic and industrial community. This, together with the complexity of the cutting process, makes it that a pragmatic approach is desirable. In the industrial practice very little is known about the rock that has to be cut, which is often limited to the UCS, the type of rock (e.g. limestone, sandstone) and water depth. Several other mechanical properties of the rock are often estimated based on empiricism, some of these relations are presented in A. In order to stay close to the industrial application, the model is set up according to the following design choices:

1. Emphasis is on the influence of the fluid pressure on the cutting process for a generic type of rock.
2. Limit the number of required input parameters.
3. Aim for those effects that can be validated based on existing experimental data.
4. The characteristic domain size should resemble the cutting process of a single tool. As a result, the computational domain is required to be in the order of 0.1-2 m. Acceptable computation time is approximately one day per cutting simulation.

The methodology is developed within the author's own implementation, written in C++ and CUDA (C++ environment of NVIDIA to support GPU programming). The implementation of the DEM and SP model are described in next section. In this study, the algorithms and simulations are set up in 2D to limit the computational expense. Besides, first the suitablity of the technique needs to be proven before further investments will be made into extension to 3D. Luckily, extension to 3D is rather straightforward.

4.4. Solid Modeling - Discrete Element Method

The translational and rotational motion of a particle is governed by the standard equations for rigid body mechanics

$$m_i \ddot{\mathbf{u}}_i = \mathbf{F}_i \tag{4.1}$$

$$I_i \dot{\omega}_i = \mathbf{T}_i \tag{4.2}$$

where $\mathbf{F}$ and $\mathbf{T}$ are the sums of all forces and moment, m the particle mass, I the particle moment of inertia, $\mathbf{u}$ the particle centroid displacement in a fixed coordinate frame, ω the angular velocity, which are all applied to particle $_i$. The vectors $\mathbf{F}_i$ and $\mathbf{T}_i$ are calculated through

$$\mathbf{F}_i = \mathbf{F}_i^{ext} + \sum_{j=1}^{n_i^c} \mathbf{F}_{ij}^{cont} + \mathbf{F}_i^{damp} + \mathbf{F}_i^{\nabla p} \tag{4.3}$$

$$\mathbf{T}_i = \mathbf{T}_i^{ext} + \sum_{j=1}^{n_i^c} \mathbf{s}_{ij}^c \times \mathbf{F}_{ij}^{cont} + \mathbf{T}_i^{damp} \tag{4.4}$$

where $\mathbf{F}^{ext}$ and $\mathbf{T}^{ext}$ are external loads, $\mathbf{F}_{ij}^{cont}$ the contact interactions with neighboring particles $j = 1, ..., n_i^c$, with n_i^c the number of contacting neighboring elements, numerical damping loads $\mathbf{F}^{damp}$ and $\mathbf{T}^{damp}$, $\mathbf{s}_{ij}^c$ is the vector that connects the center of mass of particle $_i$ with the contact point with particle $_j$ and $\mathbf{F}_i^{\nabla p}$ the coupling force resulting from the fluid pressure gradient over the particle. The numerical damping is defined by

$$\mathbf{F}_i^{damp} = -\alpha |\mathbf{F}_i^{ext} + \mathbf{F}_i^{cont}| \frac{\dot{\mathbf{u}}_i}{|\dot{\mathbf{u}}_i|} \tag{4.5}$$

$$\mathbf{T}_i^{damp} = -\alpha |\mathbf{T}_i^{ext} + \mathbf{T}_i^{cont}| \frac{\dot{\omega}_i}{|\dot{\omega}_i|} \tag{4.6}$$

where α is the numerical damping coefficient. The numerical damping is similar to what is first used by Potyondy and Cundall (2004). Their definition of numerical damping is included in the commercial DEM-code PFC (Particle Flow Code) developed by Itasca and it is included in DEMPack (Rojek et al., 2011), developed by CIMNE.

The equations of motion (4.1) and (4.2) are integrated in time by using the explicit velocity Verlet scheme.

$$\mathbf{u}_i^{n+1} = \mathbf{u}_i^n + \dot{\mathbf{u}}_i^n \Delta t + \frac{1}{2}\ddot{\mathbf{u}}_i^n \Delta t^2 \tag{4.7}$$

$$\dot{\mathbf{u}}_i^{n+1/2} = \dot{\mathbf{u}}_i^n + \frac{1}{2}\ddot{\mathbf{u}}_i^n \Delta t \tag{4.8}$$

$$\ddot{\mathbf{u}}_i^{n+1} = \frac{1}{m_i}\sum \mathbf{F}_i^{n+1} \tag{4.9}$$

$$\dot{\mathbf{u}}_i^{n+1} = \dot{\mathbf{u}}_i^{n+1/2} + \frac{1}{2}\ddot{\mathbf{u}}_i^{n+1} \Delta t \tag{4.10}$$

The advantage of the velocity Verlet scheme is that it only requires to sum all particle interactions once per time step, it is fully reversible and has no artificial damping in itself. Because the scheme is an explicit integration scheme, the timestep is limited by

$$\Delta t_{crit} = \min \sqrt{\frac{m_i}{\sum_{n^c} k_n}} \tag{4.11}$$

4.4.1. Constitutive model

Models of contact interactions $\mathbf{F}_{ij}^{cont}$ are based on the decomposition of $\mathbf{F}_{ij}^{cont}$ into normal and tangential components, respectively

$$\mathbf{F}^{cont} = F_n^{cont}\mathbf{n} + F_s^{cont}\mathbf{t} \tag{4.12}$$

where $\mathbf{n}$ is the normal vector with respect to the particle surface at the contact point, $\mathbf{t}$ is the unit tangent vector aligned with the tangent force, F_n^{cont} and F_s^{cont} are the scalar quantities that are obtained by projection of $\mathbf{F}^{cont}$ on the base vectors. See figure 4.4 for an overview.

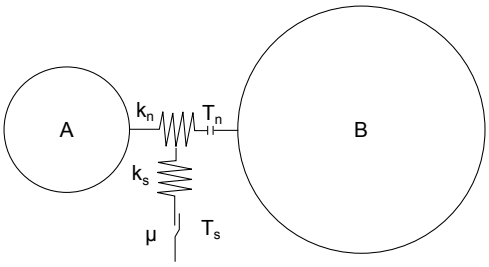

Figure 4.4: Contact interaction model

The interaction force between a pair of particles can either consist of a bond type or a collision type of interaction. At the beginning of each simulation, the particles that are in contact are bonded together. These bonds are modeled with an elastic perfectly brittle model. The interaction between two particles is modeled as a collision when either their bond is broken or never a bond has existed between

these contacting particles. The interaction models are in the form of

$$F_n^{cont} = k_n u_n \tag{4.13}$$
$$\Delta F_s^{cont} = k_s \Delta u_s \tag{4.14}$$

where k_n is stiffness in normal direction, k_s stiffness in shear (tangential) direction, u_n normal relative displacement which is positive in compressive direction and negative in tensile direction and u_s tangential relative displacement. Here compressive forces are considered to be negative (overlapping particles), and tensile forces positive (distance between particles). Note that the shear force is calculated in an incremental form, because it is less prone to drift in this form. Bonds fail instantaneously when either the shear strength (tangential direction) or the tensile strength (normal direction) is exceeded. Bonds remain intact when

$$F_n \geq T_n \tag{4.15}$$
$$|\mathbf{F}_s| \leq T_s \tag{4.16}$$

with tensile strength of the bond T_n and shear strength of the bond T_s. Although a compressive interaction force between the particles does not result in bond breakage, on a macroscopic scale compression is properly represented by allowing the shear and tensile breakage of the bonds on the micro-scale.

In case of a collisional interaction between particles, the tangential force is evaluated assuming the Coulomb model of friction, that can either inhibit stick and slip conditions:

$$|\mathbf{F}_s| = \min \begin{cases} \mu_{Coulomb} F_n \\ k_s |\mathbf{u}_s| \end{cases} \tag{4.17}$$

with friction coefficient $\mu_{Coulomb}$. A graphical representation of the bond model and its failure criteria is shown in figure 4.5.

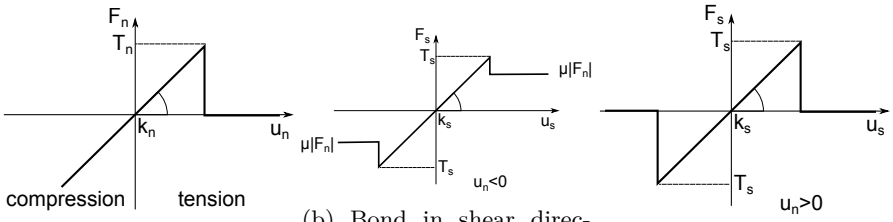

(a) Bond in normal direction.

(b) Bond in shear direction, with contact.

(c) Bond in shear direction, without contact.

Figure 4.5: Bond models

In this research, it is opted to use some of the simples DEM interaction models for both bonds and collisions. The main reasons to do this is that often the introduction of more advanced models requires more input parameters, while the experiments on which the validation of this research is based have rather limited detail on the mechanical properties of the tested rock. Addition of more input-parameters does

not help to improve the understanding of the rock cutting process, although it might improve the results. In a later stage of the research, one might think about on using more advanced bond and collision models to improve the results. Some of the most interesting improvements are the parallel bond model (Potyondy and Cundall, 2004), or one can add viscous or history terms to the bond model as is done in powder sintering models, e.g. (Luding, 2011), (Rojek et al., 2017).

Particle Geometry

Dilative, compactive and frictional (post-failure) effects are likely to be misinterpreted when using disc-shaped particles. To improve on these effects, besides tuning the particle size distribution of the generated mesh, complex particle shapes are often used. Although beyond the scope of this research, due to the introduction of new variables, several options to improve on these effects are suggested in literature:

- Rolling resistance: Besides the stick/slip behavior that is modeled for the tangential interaction force, an additional resistance that restricts the rolling of the particle can be included. This rolling resistance is a commonly accepted method to adjust for the non-sphericity of the particles (Luding, 2008).

- Particle clusters: Particles are combined to create arbitrarily shaped particle clusters. The micro-models of the inter- and intra-cluster interactions differ. Often the intra-cluster interactions have a higher stiffness and strength compared to the inter-cluster interactions. For example, see the work of Thomas and Bray (1999) and Potyondy and Cundall (2004).

- Particle clumps: Similar to particle clusters, except for now the particles are allowed to overlap. The overlapping particles act as a rigid body clump, see (Cho et al., 2007).

- Grain interlocking: When the initial geometry is set up, particles are allowed to have a small overlap. When installing the bonds, these bonds are installed with an equivalent distance in such a way that the initial state of the rock can be stress free. However, this method has its limitations, the initial overlap cannot be larger than the break-up length for tensile failure, i.e. when a particle fails in tensile direction, the particles must not have contact. See (Scholtès and Donzé, 2013).

However, the disadvantage of these improvements is that each of them introduces one or multiple parameters extra. In chapter 5 an analysis on the parameters and the parameter sensitivity will be presented. The improvements on particle geometry as mentioned before are not implemented in the model of this dissertation. The main reason to not do this is that the suggested improvements only give rise to slightly different types of rocks, but are expected to have little influence on the hydro-mechanical coupling of the pore fluid. However, these improvements might be included in a later phase of the research if it is needed for a specific type of rock.

4.5. Fluid Modeling - Smoothed Particle

Due to the low permeability of rock-like materials, the contribution of hydro mechanical effects of a fluid to the mechanical properties of a rock is dominated by the generated pressure gradient. The effect of fluid velocity on the mechanical behavior of rock is in that range negligible. For that reason, the fluid phase can be simplified in such a way that velocity of the fluid is not fully solved. This can be achieved through a pore pressure diffusion equation Coussy (2004). This equation is based on the combination of mass conservation, Darcy flow and a constitutive equation for the compressibility of the pore fluid, given respectively by

$$\frac{D\zeta}{Dt} + \nabla \cdot \mathbf{q} = \gamma \tag{4.18}$$

$$\mathbf{q} = -\frac{\kappa}{\mu}\left(\nabla p - \mathbf{f}\right) \tag{4.19}$$

$$p = M\left(\zeta - \alpha\epsilon_V\right) \tag{4.20}$$

with pore fluid content ζ, fluid flux $\mathbf{q}$, fluid source/sink γ, intrinsic permeability κ, pore pressure p, body force $\mathbf{f}$, Biot modulus M, effective stress coefficient α and volumetric strain ϵ_V. By combining the equations (4.18), (4.19) and (4.20), the pore pressure diffusion equation is obtained.

$$\frac{Dp}{Dt} - M\nabla \cdot \left(\frac{\kappa}{\mu}\nabla p\right) = -\alpha M\frac{D\epsilon_V}{Dt} + M\left(\gamma - \frac{\kappa}{\mu}\nabla \mathbf{f}\right) \tag{4.21}$$

The right hand terms respectively describe the volumetric strain (dilation/compaction of pore volume), fluid source/sink and a gradient in an external force. The last two terms are of negligible effect on the rock cutting process considered in this thesis. Here purely mechanical effects and deformations are considered, effects of jetting or pumping are beyond the scope of this research. Furthermore, it is assumed that thermal effects are negligible with respect to the fluid pressure effects and therefore the models is assumed to be iso-thermal as well.

Due to the discontinuum properties of DEM, it is not possible to directly solve a continuum equation, like equation (4.21). The discontinuous data of DEM needs to be interpolated towards continuum properties, which can be achieved by applying an interpolation technique based on the smoothed particle (SP) approach, which weighs each close neighbouring particle contribution to an interpolation point based on a kernel function. In this research, the interpolation points of SP are collocated with the particle centers of the DEM particles. These interpolation points will also move along with the movement of the DEM particles. The advantage of using SP in combination with DEM is that the structure of both algorithms is identical, except the particle interactions differ.

A proper kernel function is consistent, has small support and is sufficiently smooth. Small support means a small domain of influence, which is desirable to limit the computational expense of the simulation. The integral of the kernel function within its domain of influence should be equal to unity, and the integral of the kernel gradient should be equal to zero. A smoothing function with smoother value

of the function and derivatives usually yields better results. Using a sufficiently continuous kernel function makes the algorithm less sensitive to particle disorder and the errors in approximating the integral interpolants are small provided that the particle disorder is not too extreme. Here the Wendland C2 kernel function (Wendland, 1995) is used, because of its consistency, small support and smoothness properties. The kernel is given by

$$W = \begin{cases} \frac{7}{\pi}\left(1-R\right)^4\left(4R+1\right) & \text{if} \quad R \leq 1 \\ 0 & \text{if} \quad R > 1 \end{cases} \tag{4.22}$$

where

$$R = \frac{|\mathbf{r}_i - \mathbf{r}_j|}{h} \tag{4.23}$$

with smoothing length h and dimensionless relative distance R.

In the DEM-SP model, the discretized particles are taken from a particle size distribution and randomly stacked together. The unstructured positions and random size and mass of the particles can easily cause stability issues. Close to the boundaries of the domain, the kernel support may not be entirely contained within the problem domain. To preserve linear consistency near the boundaries, the Corrective Smoothed Particle Method (CSPM) is used (Chen et al., 1999).

In CSPM, the kernel interpolation of a field quantity A is calculated by

$$A\left(\mathbf{u}_i\right) = \frac{\sum_j A_j m_j W\left(\mathbf{r}_i - \mathbf{r}_j, h\right)}{\sum_j m_j W\left(\mathbf{r}_i - \mathbf{r}_j, h\right)} \tag{4.24}$$

with particle mass m, kernel function W, smoothing length h, index $_i$ for the particle under consideration and index $_j$ for the neighboring particles (including particle $_i$). In the CSPM, the equations for the first derivatives have to be calculated in a coupled fashion (Chen et al., 1999). This can be done by solving the set of equations

$$X_{\alpha\beta i} A_{\alpha i} = Y_{\beta i} \tag{4.25}$$

where

$$X_{\beta\alpha i} = \sum_{j=1}^{N} \left(r_j^\alpha - r_i^\alpha\right) \nabla_\beta m_j W\left(\mathbf{r}_i - \mathbf{r}_j, h\right) \tag{4.26}$$

$$Y_{\beta i} = \sum_{j=1}^{N} \left(A_j^\alpha - A_i^\alpha\right) \nabla_\beta m_j W\left(\mathbf{r}_i - \mathbf{r}_j, h\right) \tag{4.27}$$

gives the first derivative approximations. In above equations, $_\alpha$ and $_\beta$ are the indices of the spatial derivatives.

Unfortunately, higher order derivatives in SP, necessary for the diffusive term in (4.21), cannot be calculated directly by taking the second derivative of the kernel function. Fatehi et al. (2009) give several options to calculate the second derivative, i.e. double summation, second order kernel derivation, difference scheme. The double summation scheme requires to first calculate the first order derivative of each

particle, resulting in a large extra computational effort (looping twice over each particle). Although the second-order kernel derivation and the difference schemes can compute the second derivative in the same loop as the first derivative, implementation of Neumann boundaries are not straightforward. Cleary and Monaghan (1999) derived a model for heat conduction based on the difference scheme. In this scheme the diffusive term is calculated directly, it can deal with discontinuities in material parameters and it automatically adopts Neumann boundary conditions when not stated otherwise. Implementation of Dirichlet conditions is straightforward in this method. That is why in this research the methodology of Cleary and Monaghan (1999) is implemented, which is done in the form of

$$\nabla \cdot \left(\frac{\kappa}{\mu} \nabla p \right) = \sum_j \frac{m_j \left(\kappa_i + \kappa_j \right)}{\rho_i \left(\mu_i + \mu_j \right)} \left(p_i - p_j \right) \frac{\mathbf{n}_{ij} \cdot \nabla W \left(\mathbf{r}_i - \mathbf{r}_j, h \right)}{|\mathbf{r}_i - \mathbf{r}_j|} \tag{4.28}$$

where $\mathbf{n}_{ij}$ is the normal unit vector of the neighboring particle centers. Note that here κ and μ are considered as particle properties, meaning that these parameters can differ throughout the rock sample. In the case of DEM-SP, these parameters are assumed to be constant.

Two way coupling is applied at every timestep. DEM is advanced half a timestep as in equation 4.9, based on the intermediate velocities of the DEM-particles, the volumetric strain rate is calculated for the fluid. This is then used to advance the pore pressure diffusion equation one timestep. The resultant local pressure gradient of the fluid is calculated based on the new pore pressure distribution. The pressure gradient on a particle is then added as an interaction force to the sum of forces acting on the particles in equation 4.8 through

$$\mathbf{F}_i = -\nabla p \pi r_i^2 \tag{4.29}$$

with particle radius r_i. See figure 4.6 for an overview of the algorithm. Care must be taken when using this pore pressure coupling. When the coupling force is much larger than the strength of the particle bonds, i.e.

$$\nabla p \pi r_i^2 \gg T_n \tag{4.30}$$

the rock will disintegrate and the resulting behavior will be unrealistic. The effect becomes apparent when increasing either the particle size, whose effect scales quadratically, or by increasing the hydrostatic pressure, which leads to a higher maximum achievable pore pressure gradient, assuming that the cavitating limit can be met. If it is not met, larger hydrostatic pressure does not necessarily lead to different ∇p. Note that in the case of rock cutting for deep sea applications, the maximum achievable pore pressure gradient can be in the order of GPa/m.

Following the same analogy as in Cleary and Monaghan (1999), the critical time step for a pure diffusion problem of the fluid phase is given by

$$\Delta t_f = \frac{\beta \mu_f h^2}{M \kappa} \tag{4.31}$$

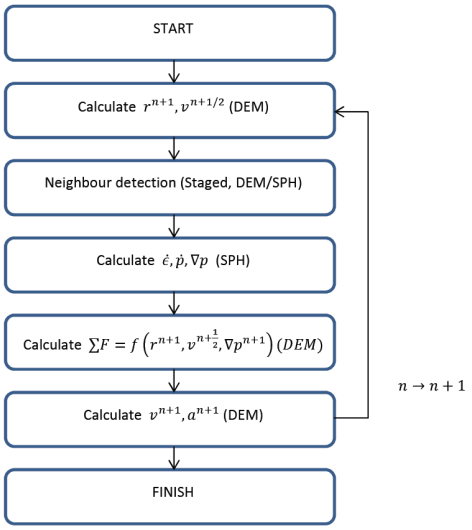

Figure 4.6: Flowchart of the calculations done per timestep in DEM-SP.

where β is a constant. According to Cleary and Monaghan (1999), $\beta \leq 0.15$ is required for a stable time integration for a structured set of particles. Although the set of particles is unstructured and a non-uniform particle distribution is used, in our case the time integration of DEM-SP is mostly limited by the stability of the solid phase. In the case of high permeability ($\kappa \geq 10^{-11}\text{m}^2$ when assuming water as pore fluid and gravelstone like rock), the critical timestep of the fluid phase might become limiting. However, in such a case the peaks in the fluid pressure will diffuse sufficiently fast that its influence on the failure mechanics of the rock is negligible. Due to the full coupling between solid and fluid phase, both phases have to march in time with the same step size, therefore a forward Euler scheme is sufficient for the fluid phase.

At the beginning of each simulation, the intrinsic permeability of the simulated rock is set as a global homogeneous and isotropic material property. Changes in permeability due to deformation of the rock are not considered within this research. The main reason to do so is that with the large range in strain rates that are considered within this thesis (up to 6 orders of magnitude) in this research, the local variations due to dilation and compaction are considered to be insignificant. When cracks occur and they are opened sufficiently, they are considered as a new (internal) boundary and hydrostatic pressure is then instantly applied, assuming that in such a case the permeability of the crack is several orders of magnitude larger.

It is possible that the fluid pressure drops below the vapor pressure during simulations, resulting in cavitation. When cavitation occurs, the compressibility of the fluid increases with several orders of magnitude. In the case of failure of saturated rock, the pore pressures can easily obtain a pressure gradient in the order

of $\mathcal{O}$ (GPa/m). Therefore it is chosen to model cavitation through a simplified approach, by the assumption that the phase transition of liquid to vapor or vice versa, are of negligible effect, except for the local pressure values (in case of cavitation of water the compressibility of the fluid increases with approximately the same factor as the viscosity decreases, which merely affects the source term in equation (4.21) and the combination of these two parameters is of negligible effect on the diffusivity of the pore pressure). When the pressure drops below the vapor pressure, the pressure value is fixed at the minimum pressure. From thereon it is only possible to increase the pressure by having fluid flow towards the cavitating zone, so if

$$p_i < p_{min} \quad \text{then} \quad p_i = p_{min} \quad \text{and} \quad \frac{\partial p_i}{\partial t} = \max\left(\frac{\partial p_i}{\partial t}, 0\right) \tag{4.32}$$

and both the fluid bulk modulus and the dynamic fluid viscosity are adjusted in those areas. In the case of water as a pore fluid this results in a bulk modulus that is approximately $\mathcal{O}\left(10^3\right)$ smaller and a dynamic viscosity that is also approximately $\mathcal{O}\left(10^3\right)$ smaller. As a result, the fluid pressure in the cavitating zone is close to uniform, resulting in an almost negligible pressure gradient force acting on the solid and dilative effects of the solid are no longer counteracted upon by the pore pressure gradient. In the end, cavitation has no effect on the numerical stability of the time integration scheme ($\Delta t_{crit} = \text{constant}$). Simulations of rock saturated with air show no significant differences compared to simulations without pore fluid interaction. This is due to the high compressibility of air compared to liquids, like water, oil, resulting in a factor of $\mathcal{O}(10^3 - 10^4)$ in difference.

4.5.1. Boundary conditions and detection

Often in smoothed particle simulations, the boundary conditions are applied by using either repulsive forces (Monaghan, 1994) or ghost particles (Colagrossi and Landrini, 2003). However, in this case the SP are coupled in a co-located fashion with the DEM, complicating the use of such methods. In these methods, the motion of the particles are described by SP as well, while in DEM-SP the motion of the particles is dictated by the DEM. Therefore it is desired to apply boundary conditions on the particles that are part of the boundary itself.

By using the discretisation of Cleary and Monaghan (1999), as in equation (4.28), undrained boundary conditions (no fluid flow, i.e. $\frac{\partial p}{\partial \mathbf{n}}|_\Gamma = 0$) are automatically applied. In order to apply a drained boundary condition (Dirichlet, i.e. hydrostatic pressure), the boundary particles on which it needs to be applied have to be detected, because interior particles can become boundary particles and vice versa. Therefore a method that can deal with a disordered particle structure and a non-uniform particle size/mass distribution is used. Besides that, the method needs to be able to detect the opening of a crack (in case of mode I failure) in the interior domain. The divergence of position, as suggested by Muhammad et al. (2013), meets these requirements. Divergence of position is given by

$$\nabla \cdot \mathbf{r} = \frac{\partial \mathbf{r}_x}{\partial x} + \frac{\partial \mathbf{r}_y}{\partial y} = 2 \tag{4.33}$$

The above equation is applied to the standard Smoothed Particle approach of Lucy (1977), in order to prevent the CSPM in equation (4.25) from adjusting the divergence of position to the particle deficiency that occurs at a boundary. In the interior domain of the rock, equation (4.33) is valid. However, at the boundaries this value differs due to particle deficiency, see figure 4.7. The divergence of position is more strict in comparison to other SP-based criteria, such as the density, sum of the kernel, etc. An advantage of the divergence of position is that it is insusceptible to what the shape or orientation of the boundary of the rock specimen is. For some of the algorithms used to determine the boundary particles in DEM this is still an issue, since these approaches determine the boundary particles with respect to a fixed or a priori known observer plane (Mendoza Rizo, 2013; Tropin et al., 2014).

In this work, particles with $\nabla \cdot \mathbf{r} \leq 1.5$ are considered to be part of the boundary. Dirichlet conditions can be applied by fixing the pressure value of the boundary particles to the desired hydrostatic pressure. In order to avoid instabilities originating from particle deficiency, particles that have less than five particles within their interpolation domain are considered to be fully surrounded by the hydrostatic pressure. As a result, the coupling force of these particles is zero.

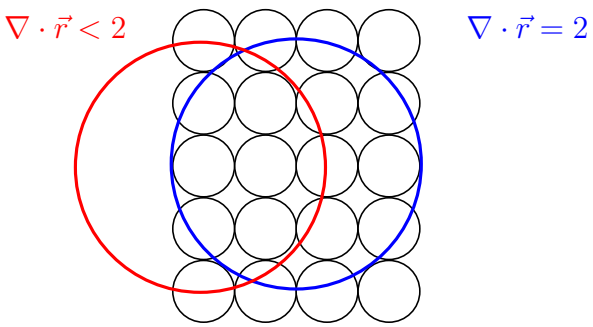

Figure 4.7: Schematic overview of particle deficiency. The incomplete kernel support of a surface particle gives a value for $\nabla \cdot \mathbf{r} \leq 2$ (2D).

4.6. Initial geometry generation

The discrete element method is best suited for materials which are inherently disordered on the microscopic scale, meaning that the material is composed of grains with various sizes and/or shapes with interactions between the grains. In the ideal case, the model gives a high quality representation of the micro-structure of the specific material. However, due to computational expenses the particles are idealized as discs with varying radii. This way, the problem of discretisation of a geometry reduces to the generation of a random homogeneous, isotropic packing of particles

with a prescribed size distribution. In general, two classes of generation methods can be distinguished, i.e. the dynamic and the constructive methods.

Dynamic methods start with an assembly of randomly distributed particles which are moved together by either sedimentation or applying compression through boundary elements until the desired porosity is achieved. Particles in the assembly that have insufficient number of contacts can be increased in size until the desired number of contacts are present. Overviews of such methods are presented in Potyondy and Cundall (2004) and in Feng et al. (2003). In these methods, the motion of each particle has to be simulated with the DEM code, which can lead to undesirable computational expense, especially for the larger particle assemblies. Furthermore the initial stress in the assembly needs to be sufficiently low to not let the initial stress affect the simulated results.

Constructive methods use a different basis. In most of such approaches particles are taken randomly from a particle size distribution and than placed alongside each other. This way, particles can be placed exactly touching its neighboring particles, resulting a zero initial stress condition. Various strategies can be applied when constructing a particle assembly.

1. Closed front methods start from the center of the geometry and add particles moving outward, e.g. (Feng et al., 2003; Zsaki, 2009).

2. Inwards packing methods start from the boundary of the geometry that needs to be generated and start moving inward, e.g. (Bagi, 2005; Benabbou et al., 2009).

In this thesis, the methodology of Bagi (2005) is used because it allows to accurately determine the boundary shape of the specimen, gives full control over the particle size distribution, has low initial stress has a sufficiently dense contact network and is fast. The porosity and the coordination number are parameters that are used as a measure of the density of the contact network. The coordination number is defined as the average number of bonds per particle. For proper rock modeling in 2D, the coordination number should be larger than 4 and the porosity lower than 0.19 (Bagi, 2005). Furthermore, the constructive geometry generation methods are fast (computation within few seconds for an assembly of $>$ 100k particles on a single CPU).

4.7. Smoothed particle averaging of discrete elements

Cleary and Monaghan (1999) have shown that their discretisation of the diffusive term is suitable for structured (regular Carthesian grid) and unstructured particle positions. In their paper they consider the particles to have the same mass and/or volume. A structured particle distribution is not realistic in the case of SPH (and DEM as well), so in order to obtain a realistic disorder of the particle structure, Cleary and Monaghan (1999) performed simulations of fluid flow with SPH. However, in DEM-SP this is not completely valid. The particles have a particle size

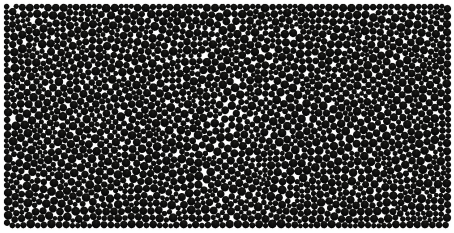

Figure 4.8: Particle position distribution for particles with unequal mass.

distribution and the positions of the particles are dictated by the underlying physics of the DEM.

In order to verify the applicability of equation (4.28) to solve diffusive problems related to the DEM, results of DEM-SP are compared with the exact solution of the diffusion equation

$$\frac{\partial u}{\partial t} = D\frac{\partial^2 u}{\partial x^2} \tag{4.34}$$

$$u(0,t) = u(1,t) = 0 \tag{4.35}$$

$$u(x,0) = \sin(\pi x) \tag{4.36}$$

in which D is the diffusion coefficient. The exact solution of the boundary value problem stated above is given by

$$u(x,t) = \sin(\pi x)\, e^{-\pi^2 Dt} \tag{4.37}$$

The settings that have been used to determine the DEM-SP solution of the diffusion equation (4.34) are a height and width of 0.5 and 1.0, respectively, with a uniform particle size distribution with radii in the range of 0.005-0.01, resulting in a total of 2142 particles. The distribution of the particle sizes and positions used for this calculation is shown in figure 4.8. The diffusion coefficient D has been set to 1.0 and for the time integration 1000 timesteps of $5 \cdot 10^{-6}$ are used. The numerical diffusion coefficient of equation (4.28) differs with varying smoothing length, as is shown in figure 4.9. The solution of (4.28) shows a spread closely comparable to the exact solution. This spread is caused by both the disordered particle positions and the non-uniform particle masses, see figure 4.10. It is clear that with a smoothing length that is too small, the diffusion coefficient is significantly underestimated, which is due to the lack of interacting particles. For larger smoothing lengths ($h > 6\bar{r}$), the diffusion coefficient is slightly overestimated, but is still within acceptable accuracy (error $< 5\%$) for application in rock mechanics.

The choice of the smoothing length requires a compromise between a minimum amount of neighboring particles to assure stability, while on the other hand it is desired to use as few neighboring particles as possible to limit the computational

expense and to avoid the loss of detail due to smoothing. Therefore it is chosen to use a smoothing length in the range of $5\bar{r} - 6\bar{r}$.

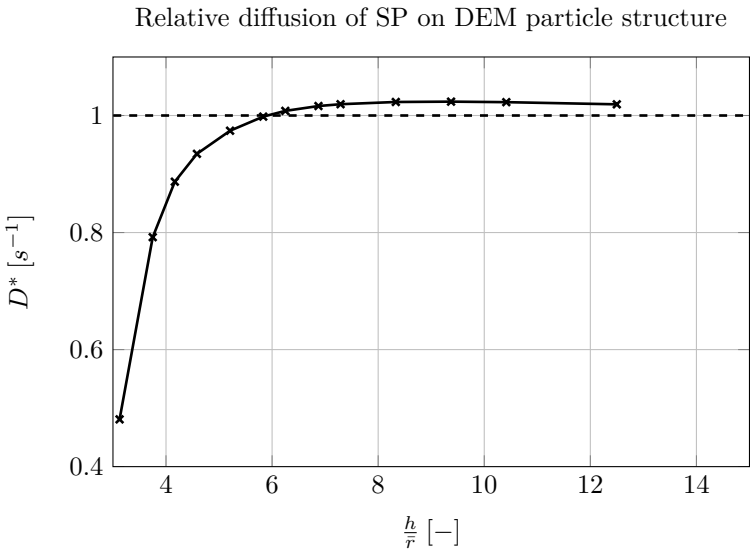

Figure 4.9: Diffusion coefficient with respect to the relative smoothing length. D^* is the relative diffusion of the SP solution w.r.t. the exact diffusion coefficient. The relative diffusion coefficient is considered for the particle that is nearest to the line $x = 0.5$.

4.8. Conclusions

Regarding the rock cutting process, discontinuum methods have a preference over continuum based methods. The two main arguments are: 1)continuum based methods will require remeshing when significant distortion is applied to the rock, 2) a complex set of equations that will be able to cover the transition from intact rock through fragmentation towards granular flow.

The approach used within this thesis is a combination of the discrete element method to model the rock and a smoothed particle based approach to model the hydro-mechanical coupling, currently implemented in two dimensions. Due to the low permeability, fluid flow is modeled as a pore pressure diffusion process. This way, fluid velocity does not need to be solved, but it is modeled through the diffusive term. The combination of physics allows to use the DEM and SP in a co-located fashion. It is the first attempt to incorporate full hydro-mechanical coupling in DEM on this scale.

Solid boundaries of the rock are identified by calculation of the divergence of position with SP. The use of SP to model diffusive processes with particle size and position distributions based on DEM problems show good resemblance with the exact solution. A smoothing length of $5\bar{r} - 6\bar{r}$ gives the best compromise between

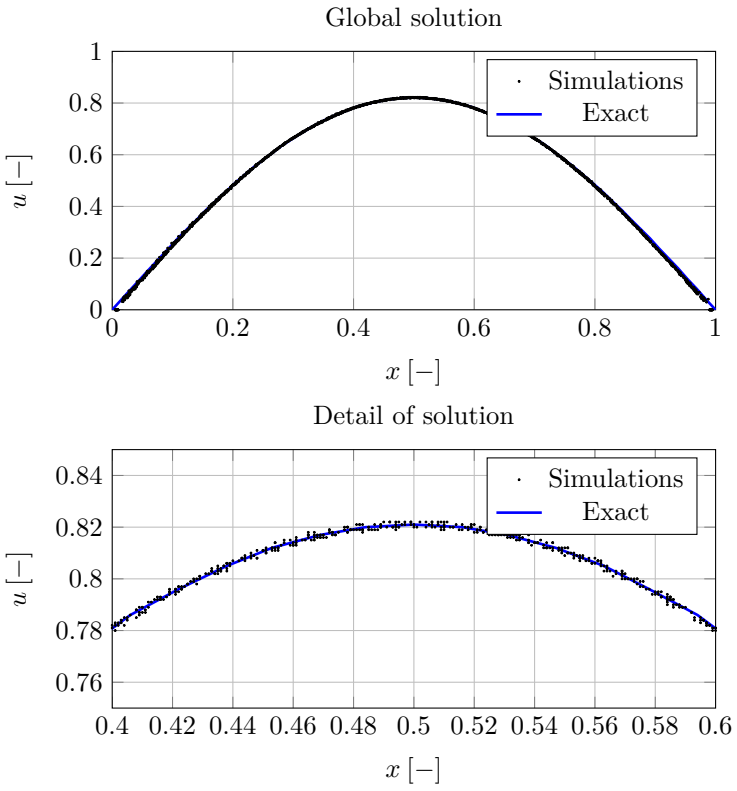

Figure 4.10: Solution of (4.34), results obtained by solving the diffusive term with equation (4.28) and the exact solution according to equation (4.37).

computational effort and accuracy to solve the pore pressure diffusion equation.

5

Validation - Material tests

"There are known knowns. These are things we know that we know. There are known unknowns. That is to say, there are things that we know we don't know. But there are also unknown unknowns. There are things we don't know we don't know."

Donald Rumsfeld

The combination of the DEM and the hydro-mechanical coupling effect, which is modeled with a smoothed particle approach, gives rise to a large number of independent parameters. First a parameter sensitivity analysis is presented. Here the most relevant micro-parameters of the DEM are compared between dry and saturated conditions. Additionally, it is shown that the methodology corresponds with Terzaghi's effective stress theory. Furthermore, simulations of shale samples over a range of several orders of magnitude in strain rate are compared with experiments in literature.

Part of this chapter has been published in Helmons et al. (2016b).

5.1. Parameter sensitivity

Huang (1999) developed a methodology to calibrate the macro-parameters of a rock specimen based on the combination of dimensional analysis and numerical simulations of the standard laboratory tests, e.g. unconfined compression test, Brazilian test. Other researchers have adopted this methodology as well, (Yang et al., 2006; Fakhimi and Villegas, 2007; Rojek et al., 2011).

Dimensional analysis is performed, based on the Buckingham π theorem. This theorem states that any physically meaningful relationship of N variables can be expressed equivalently by a function of $N - c$ dimensionless parameters, where c is the number of primary dimensions, in this case being mass, length and time. The macroscopic parameters that define the behavior of dry rock are: Young's modulus E, Poisson's ratio ν, uni-axial compressive strength σ_{UCS} and tensile strength σ_{BTS}. The hydro-mechanical coupling effects are characterized by the fluid's bulk modulus M, dynamic viscosity η, hydrostatic pressure p_h, pore pressure p_p, the rock's intrinsic permeability κ and effective stress coefficient α. The micro-parameters that define the macro-scopic properties of the simulated rock are k_n, k_s, T_n, T_s, μ, α_d. Furthermore, the properties of the particle assembly are of influence as well: average particle diameter $\bar{d_p}$, porosity of the particle assembly n (not necessarily the same porosity as that of the real specimen), material density ρ, loading velocity V and characteristic specimen dimension L (possible scale effects, (Yenigül and Alvarez Grima, 2010)). This leads to a total of 16 parameters, which can be reduced to 13 independent parameters. Note that κ and η only occur once in the whole set of equations in the same term that they cannot be treated as separate parameters.

The set of parameters is not unique and can be modified by considering other parameters as well. One can argue whether the type of particle size distribution (e.g. Gaussian, uniform) should be considered or not. Here it is assumed that the geometrical porosity of the particle assembly is directly related to the particle size distribution. The set of independent parameters considered in this study is:

$$\begin{aligned} &\text{Dry rock} && \frac{k_n}{k_s}, \frac{T_n}{T_s}, \frac{k_n \bar{d_p}}{T_n}, \mu, \alpha_d \frac{V}{\sqrt{k_n/\rho}} \\ &\text{Geometry} && \frac{d_p}{L}, n \\ &\text{Hydromechanical coupling} && \frac{M}{k_n}, \alpha_d, \frac{p_h}{p_p}, \frac{\kappa}{\eta}\frac{M}{V d_p} \end{aligned} \tag{5.1}$$

Even more parameters could be necessary to include when considering more complex bond and/or collision models. Due to the large number of independent variables, some assumptions and simplifications are made. As stated in chapter 4, the numerical damping is chosen to be exactly the same as used by Potyondy and Cundall (2004) and is thus fixed at the value of 0.7. Geometry scaling effects of particle size with respect to specimen size are already thoroughly investigated by Yenigül and Alvarez Grima (2010). Concerning the hydro-mechanical coupling, various parameters are limited to the application of water or air. Other fluids are beyond the scope of this dissertation. In order to investigate hydro-mechanical

coupling effects on a generic type of rock, these effects will be investigated in a parameter study on material tests (UCS and BTS) for dry and saturated rock, in the undrained regime.

Due to the large number of simulations needed in the parameter sensitivity analysis, post processing to determine the macro parameters is automated. The criteria that are used are:

- σ_c: maximum force acting on a plate in a UCS-test, divided by W, the width of the sample, to obtain stress.
- σ_t: maximum force acting on a plate in a BTS test, calculated as $\sigma_t = \frac{2F_{max}}{\pi W}$.
- E': determined at 0.2 millistrain before maximum force in a UCS-test, calculated as $E' = \frac{\sigma_1}{\epsilon_{yy}}$.
- ν', determined at 0.2 millistrain before maximum force in a UCS-test, calculated as $\nu' = -\frac{\epsilon_{xx}}{\epsilon_{yy}}$, where ϵ_{xx} is determined by measuring the averaged x-coordinate of the outermost particles at these free boundaries.

Currently, the DEM-SP is in 2D, inherently assuming plane strain conditions (that is why $'$ is used). Therefore the Poisson's ratio and the Young's modulus are corrected for 3D analysis through

$$\nu = \frac{\nu'}{1 - \nu'} \tag{5.2}$$

$$E = \frac{E'}{1 - \nu^2} \tag{5.3}$$

For each test both the damaged sample and the stress-strain curves are checked to verify that the obtained result indeed corresponds with an artificial rock and the criteria mentioned before. Combinations of micro parameters that would result in behavior that does not correspond with the criteria mentioned before are not considered within the scope of this dissertation. Some examples of what might happen are:

- Maximum stress is not the same as stress at failure, i.e. the frictional strength of the sample is larger than its structural strength.
- Fluid pressure gradient forces are significantly larger than the bond strength, resulting in disintegration of the sample.

5.1.1. Results

The parameter study concerns the comparison of the dry and saturated macroscopic properties of generic rock. In this study, the micro-parameters k_n, k_s, T_n, T_s are varied. The friction coefficient μ is not varied, since it is only of limited effect when considering brittle failures up to the occurrence of the macroscopic failure (Huang, 1999). The properties of all rock samples are in this case kept identical, using the same particle assembly as well. For an overview of the constant and the varying parameters, see respectively tables 5.1 and 5.2 for an overview of respectively the

Table 5.1: Constant properties for sensitivity analysis.

Parameter	Quantity	Unit
α	0.5	[-]
μ	1.0	[-]
κ	$1 \cdot 10^{-19}$	[m^2]
η	0.001	[Pas]
K_f	2.0	[GPa]
p_h	0.1	[MPa]
p_i	0.1	[MPa]
H	0.07	[m]
W	0.035	[m]
R_{min}	0.2	[mm]
R_{avg}	0.3	[mm]
R_{max}	0.4	[mm]
h	0.0015	[m]

Table 5.2: Varying properties for sensitivity analysis.

Parameter	Quantities					
k_n	1.25	2.5	5.0	7.5	10	[GPa]
k_s	$0.5k_n$	$0.75k_n$	$1.0k_n$	$1.5k_n$	$2.0k_n$	[GPa]
T_n	$1 \cdot 10^{-6}k_n$	$2 \cdot 10^{-6}k_n$	$4 \cdot 10^{-6}k_n$	$6 \cdot 10^{-6}k_n$	$8 \cdot 10^{-6}k_n$	[N/m]
T_s	$1 \cdot 10^{-6}k_s$	$2 \cdot 10^{-6}k_s$	$4 \cdot 10^{-6}k_s$	$6 \cdot 10^{-6}k_s$	$8 \cdot 10^{-6}k_s$	[N/m]

constant and the varying parameters. For each combination of settings, four tests are performed and analyzed, being both dry (without any fluid coupling) and saturated for both UCS and BTS tests. Due to the random generation of the set of parameters, not all combinations lead to a stable solution to simulate rock. Especially the cases with high bond stiffness and low bond strength might result in this unrealistic behavior. These results are omitted from this analysis.

The results of the parameter sensitivity study on the macroscopic rock properties are shown in figures 5.1 to 5.8. All figures are based on UCS tests, except figures 5.4 and 5.7 are based on BTS tests and figures 5.5 and 5.8 are based on the combinations of UCS and BTS tests.

5.1.2. Discussion

Figure 5.1 presents the variation of the macroscopic Young's modulus as a function of the microscopic parameters for both dry and saturated conditions. Based on the results, several observations can be made. First of all, there is a significant difference in the measured Young's modulus between saturated and dry rock. In the saturated cases, the Young's modulus is significantly larger. This is due to the additional stiffness that is contributed by the fluid against any volumetric deformation. Secondly,

with an increase in the ratio of shear to normal stiffness k_s/k_n the bulk modulus of the rock sample slightly increases as well. And a third significant effect is that with an increase in the ratio of bond stiffness over bond strength $k_n R_{avg}/T_n$, the Young's modulus increases as well. The ratio can be used as a measure of the relative bond length with respect to the particle size. Low ratios allow for a relatively large bond length. As a result, the particle assembly allows for larger mobility of the particles before the bonds will fail, effectively lowering the bulk stiffness of the assembly.

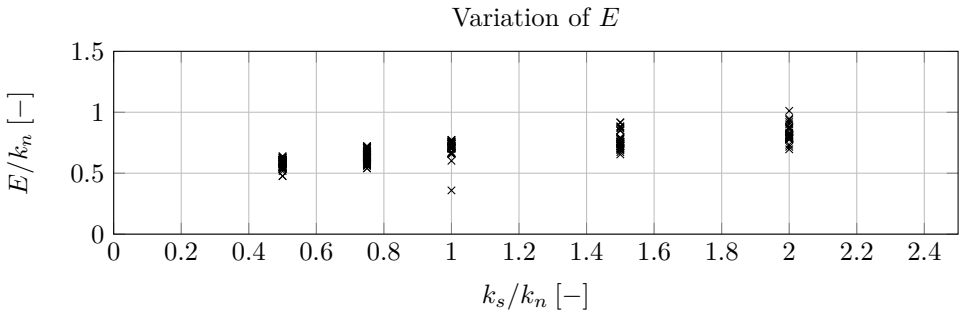

(a) Dry conditions.

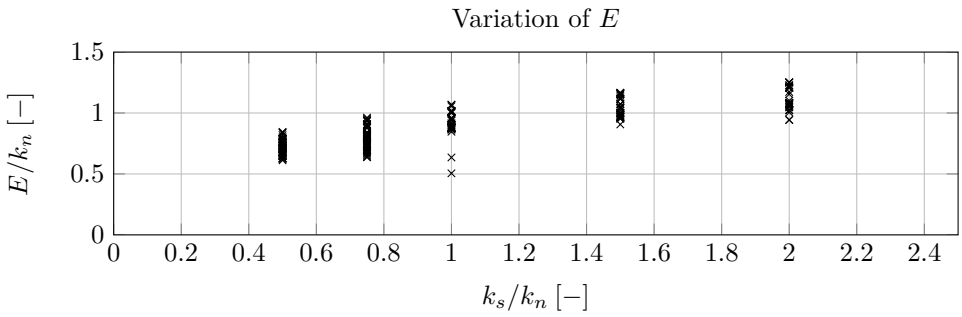

(b) Saturated conditions.

Figure 5.1: Variation of Young's modulus as a function of K_s/K_n. Micro-parameters correspond with input presented in tables 5.1 and 5.2.

The dependence of the Poisson's ratio ν on the bond stiffness ratio k_s/k_n is shown in figure 5.2. When the stiffness ratio increases, the Poisson's ratio decreases significantly. In saturated conditions, a similar trend is shown. However, it shows a higher Poisson's ratio compared to dry conditions, for all combinations of the micro-parameters used in this parameter sensitivity analysis.

Both trends for the dry Young's modulus and Poisson's ratio show similar trends compared to Huang (1999); Fakhimi and Villegas (2007); Rojek et al. (2011).

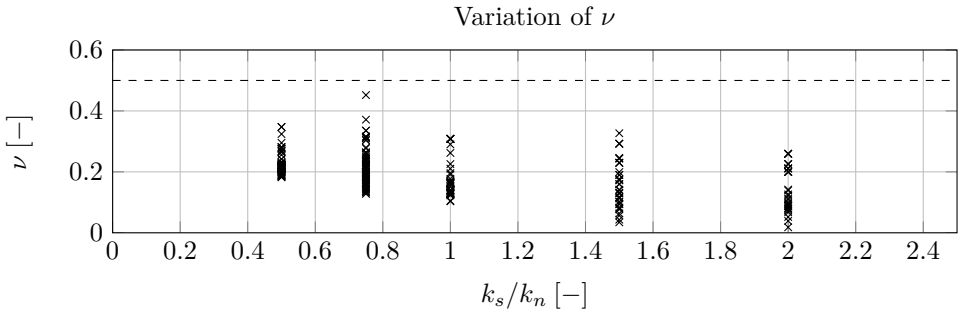

(a) Dry conditions.

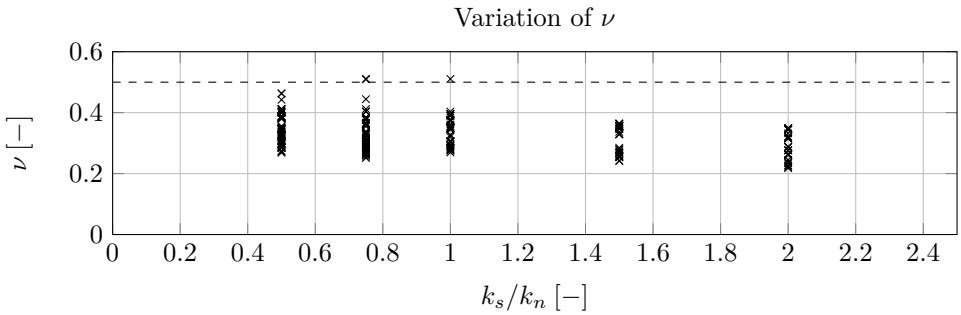

(b) Saturated conditions.

Figure 5.2: Variation of Poisson's ratio as a function of K_s/K_n Micro-parameters correspond with input presented in tables 5.1 and 5.2.

Figures 5.3, 5.4 and 5.5 the compressive, tensile and the ratio of compressive to tensile failure with respect to the input of the micro parameters. These figures show that there is a weak effect of the average bond length $k_n R_{avg}/T_n$ on the scaled strengths $\sigma_c R_{avg}/T_n$ and $\sigma_t R_{avg}/T_n$, when assuming a constant bond strength ratio T_s/T_n. This is the case for both dry and saturated conditions. Interesting to notice is that the compressive strength is lower for saturated compared to dry conditions for values of $k_n R_{avg}/T_n > 75$. The same holds for the tensile strength, but here the reduction is less significant. With respect to the strength ratio of the rock sample, a slight increase in possible ratios is noted for larger values of $k_n R_{avg}/T_n$, see figure 5.5. When comparing dry and saturated conditions, it can be observed that the strength ratio is lower and has a wider spread in saturated conditions than is the case in dry conditions.

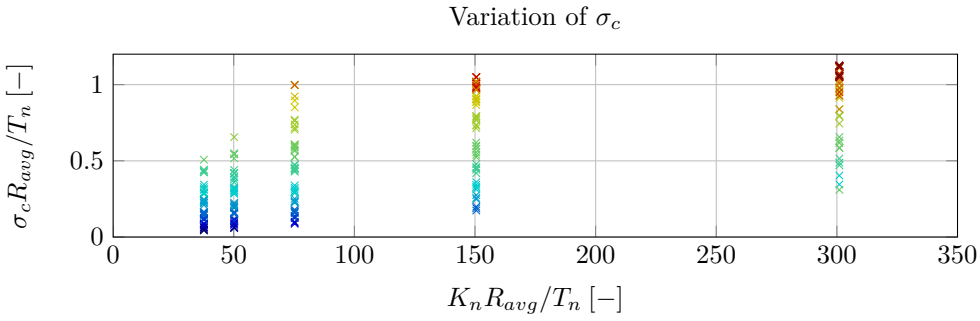

(a) Dry conditions.

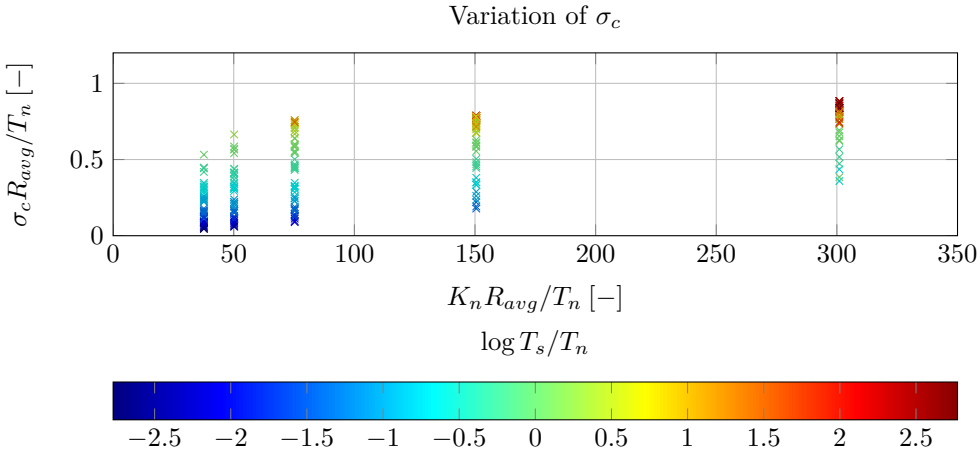

(b) Saturated conditions.

Figure 5.3: Variation of compressive strength as a function of $K_n R_{avg}/T_n$ Micro-parameters correspond with input presented in tables 5.1 and 5.2.

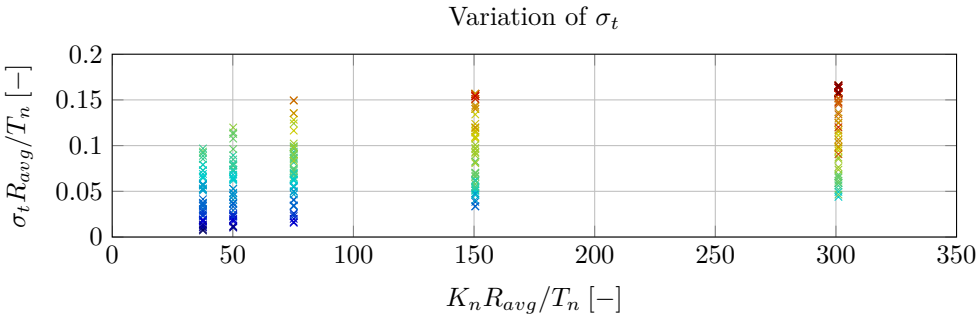

(a) Dry conditions.

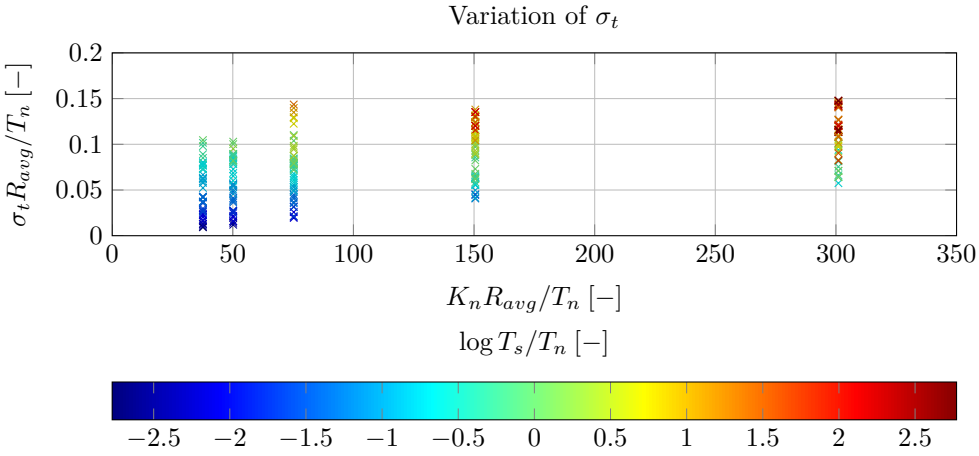

(b) Saturated conditions.

Figure 5.4: Variation of tensile strength (BTS) as a function of $K_n R_{avg}/T_n$ Micro-parameters correspond with input presented in tables 5.1 and 5.2.

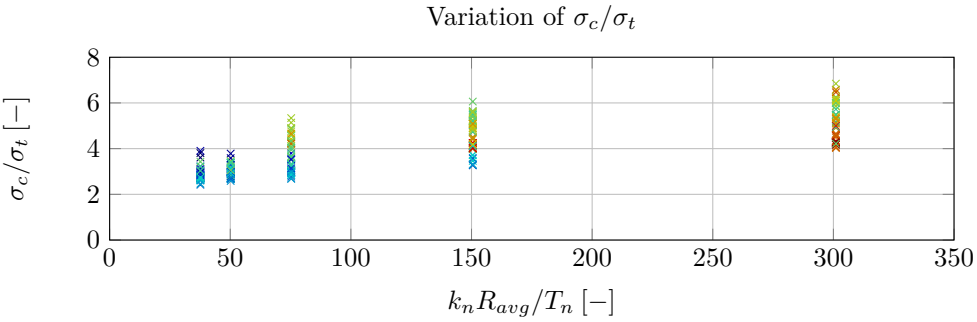

(a) Dry conditions.

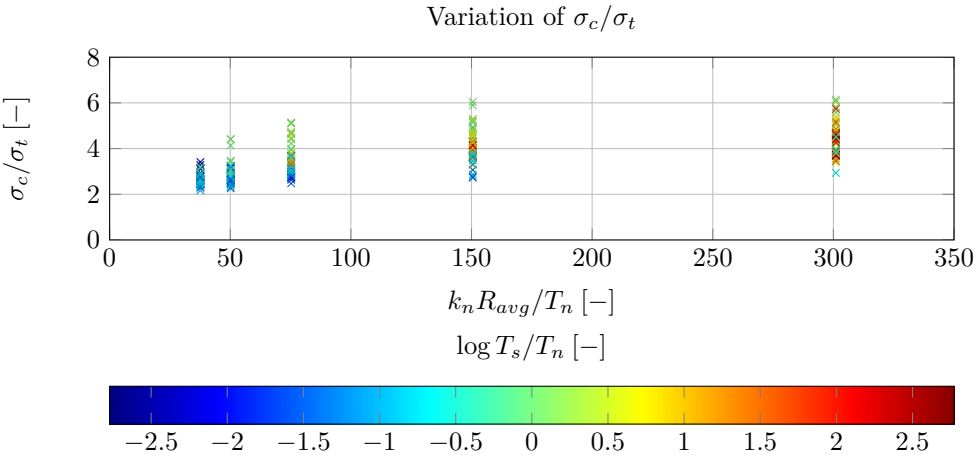

(b) Saturated conditions.

Figure 5.5: Variation of strength ratio σ_c/σ_t as a function of $K_n R_{avg}/T_n$ Micro-parameters correspond with input presented in tables 5.1 and 5.2.

Figure 5.6 presents the compressive strength with respect to the ratio of the bond shear and tensile strengths. Based on this figure, two regimes can be identified, i.e. for $T_s/T_n < 1$, the compressive strength is dominated by microscopic tensile failures, while for values > 1 microscopic shear failures are dominant. This holds for both dry and saturated conditions. Similar trends can be observed for the scaled tensile strength, see figure 5.7. Figure 5.8 shows the strength ratio with respect to the bond strength ratio on a semilog scale. The transition between tensile and shear dominated failure mechanisms is located near $T_s/T_n = 1$. In the figure it is also shown that the higher values for σ_c/σ_t are obtained for cases with smaller bond lengths (larger values for $k_n R_{avg}/T_n$).

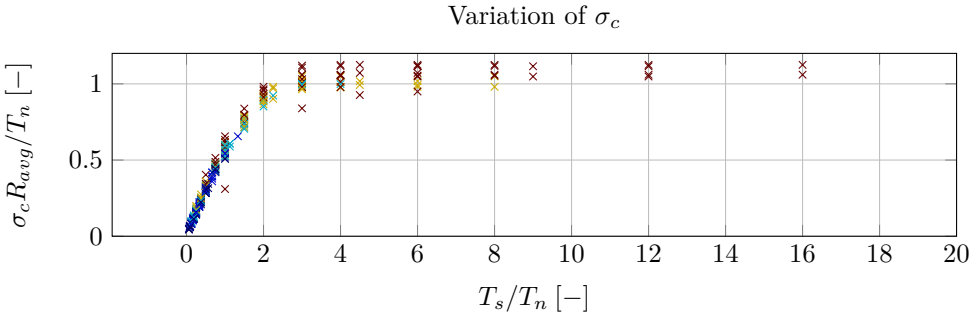

(a) Dry conditions.

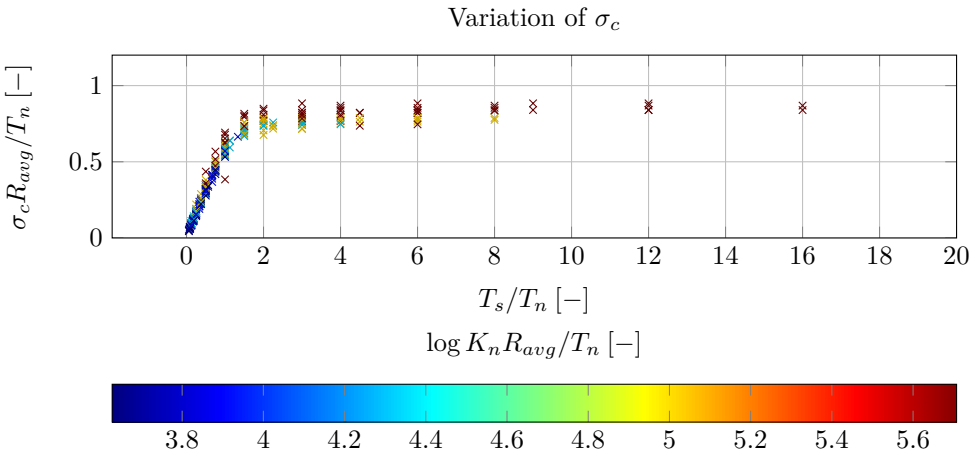

(b) Saturated conditions.

Figure 5.6: Variation of compressive strength as a function of T_s/T_n. Micro-parameters correspond with input presented in tables 5.1 and 5.2.

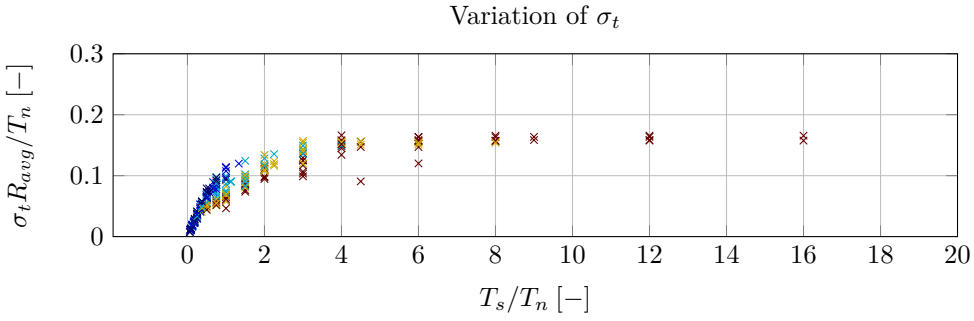

(a) Dry conditions.

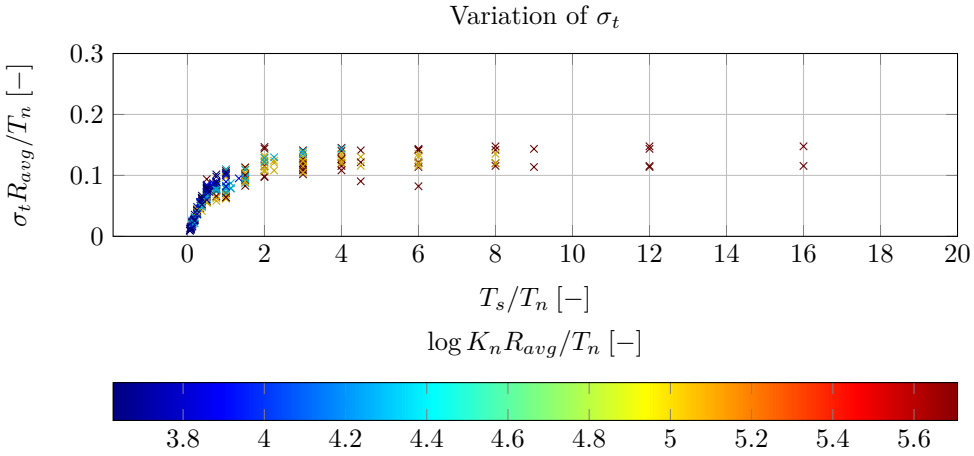

(b) Saturated conditions.

Figure 5.7: Variation of tensile strength (BTS) as a function of T_s/T_n. Micro-parameters correspond with input presented in tables 5.1 and 5.2.

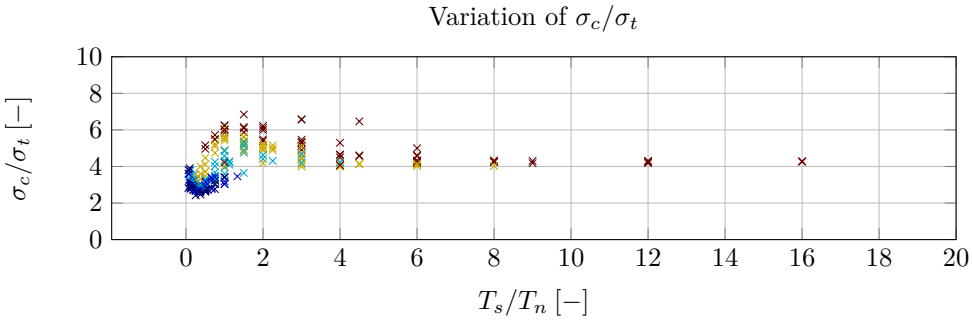

(a) Dry conditions.

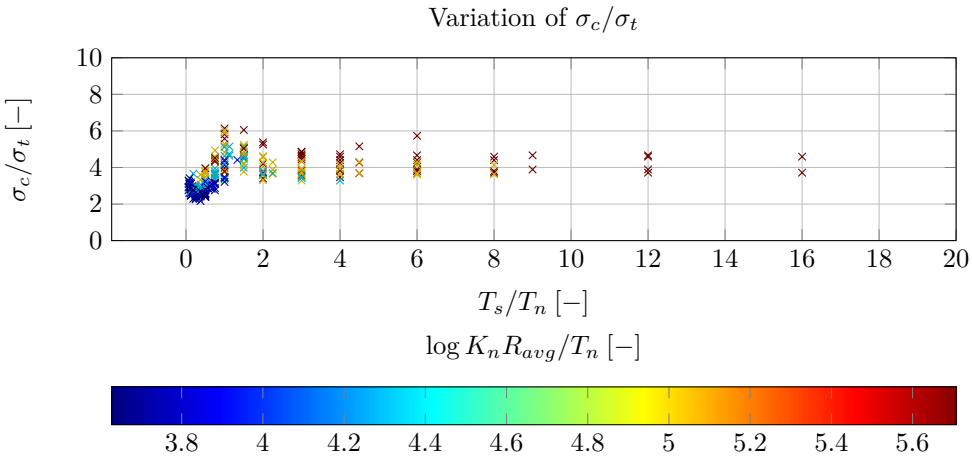

(b) Saturated conditions.

Figure 5.8: Variation of strength ratio σ_c/σ_t as a function of T_s/T_n. Micro-parameters correspond with input presented in tables 5.1 and 5.2.

In order to verify whether DEM-SP does not lead to significant differences, the same set of simulations have been performed with air as pore fluid. The fluid properties that are used are a bulk modulus of 2 MPa and a fluid viscosity of $1 \cdot 10^{-6}$ Pas. A comparison of the resulting Young's modulus and compressive strength of fluid-less DEM and DEM-SP with air is shown in figure 5.9. Both properties show almost a perfect match, only slightly some differences in Young's modulus can be observed. The differences that are noted are well within what is reasonable for the accuracy of the methodology.

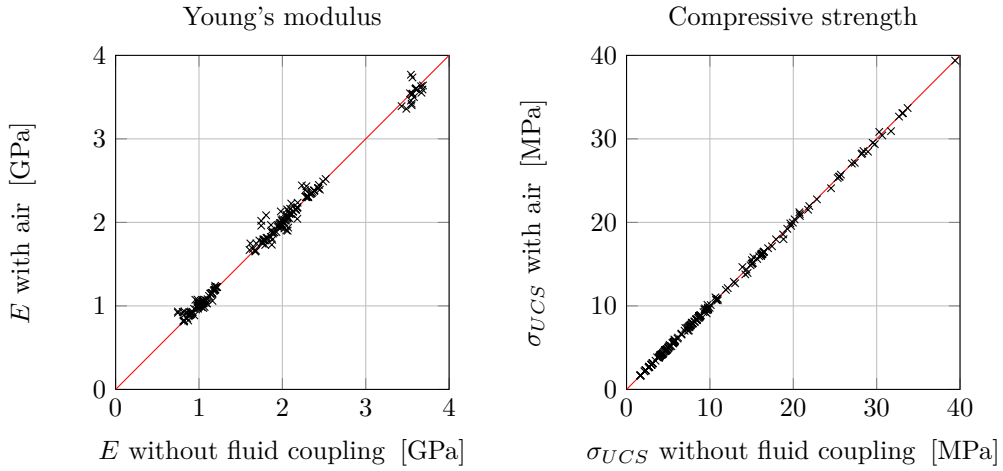

(a) Comparison of Young's modulus.

(b) Comparison of compressive strength.

Figure 5.9: Comparison of macro-properties based on DEM without any fluid coupling and DEM-SP with air

5.2. Fluid stress effects

In this section, various tests are presented that specifically look more into the effects of the hydro-mechanical coupling itself. First a set of tests is presented in which the effective stress theory of Terzaghi is verified. This is followed by a set of simulations concerning a range of strain rate effects in shale, which is based on a comparison with the experiments of Swan et al. (1989).

The micro and macro parameters that are used for these tests are shown in table 5.3. Note that in the 2D case to obtain practical units for the micro and macro parameters that a unit thickness of 1 is assumed for all particles. A comparison between the simulated rock properties and the properties of the shale are shown in table 5.4. Note that a range of permeabilities is used in the numerical rock to correct for the Deborah number N, which will be discussed in section 5.2.2.

Table 5.3: Micro and macro parameters of the artificial rock

Micro parameter	Quantity	Macro parameter	Quantity
k_n	$5 \cdot 10^9$ [Nm^{-2}]	UCS (dry)	21.4 [MPa]
k_s	$2.5 \cdot 10^9$ [Nm^{-2}]	E (dry)	3.5 [GPa]
T_n	$2 \cdot 10^4$ [Nm^{-1}]	ν (dry)	0.27 [-]
T_s	10^4 [Nm^{-1}]	Sample height	0.07 [m]
μ	1 [-]	Sample width	0.035 [m]
α	$0.5 - 0.75 - 1.0$ [-]	Nr of particles	7201
$\alpha_{damping}$	0.7 [-]	$\dot{\epsilon}$	1.43 [s^{-1}]
r_{min}	0.2 [mm]	H	0.07 [m]
r_{max}	0.4 [mm]	W	0.035 [m]
# of particles	7196	N_c	3.98 [-]
n	0.18 [-]		
P_{min}	0 [Pa]		

Table 5.4: Comparison of simulated rock and Kimmeridge Bay shale Swan et al. (1989)

Parameter	Kimmeridge Bay shale Swan et al. (1989)	DEM-SP
UCS [MPa]	23.5	21.4
E [GPa]	3.4	3.5
ν [-]	0.14	0.27
κ [m^2]	$8 \cdot 10^{-21}$	$0 - 10^{-15}$

5.2.1. Effective stress

The basic principle of the effective stress theory applied to rock mechanics has been verified with DEM-SP. About 100 simulations of jacketed bi-axial tests have been performed. In these simulations, the initial pore pressure, the confining pressure and thus the effective confining pressure are varied (with pressure values of 0.1,

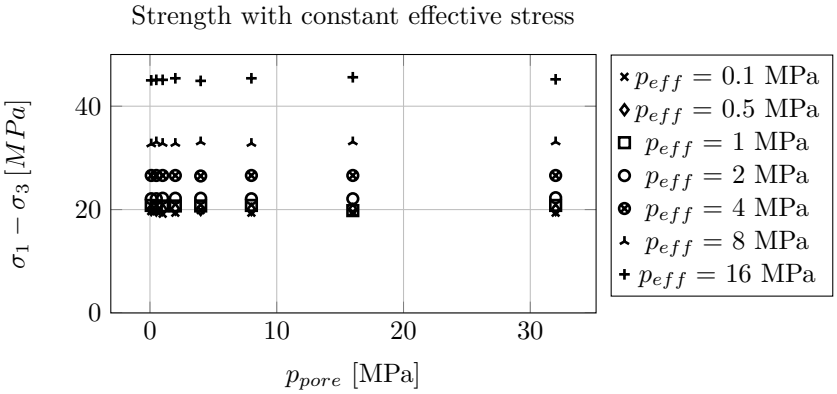

Figure 5.10: Simulated strength values with respect to initial pore pressure.

0.5, 1, 2, 4, 8, 16 and 32 MPa). A comparison of the experiments with constant effective confining stress is shown in figure 5.10. In this figure it is clearly shown that the strength of the rock does not differ for constant effective stress. Figure 5.11 shows the damage and pressure distribution in the simulated rock that is tested in saturated atmospheric conditions, i.e. $p_{pore} = p_{conf} = 0.1$ MPa. Damage is defined as $1 - \frac{\#_{bonds}}{\#_{initialbonds}}$. The damage and pressure distribution for the sample tested at $p_{pore} = 0.1$ and $p_{conf} = 16$ MPa are shown in figure 5.12.

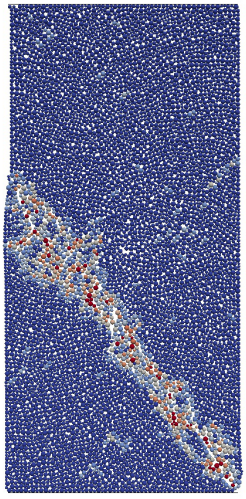

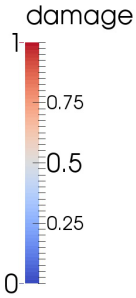

(a) Damage distribution.

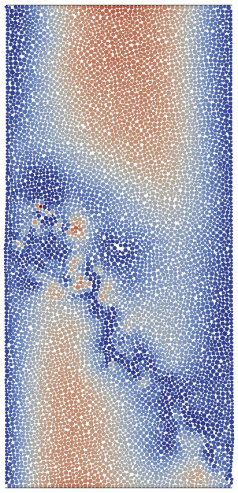

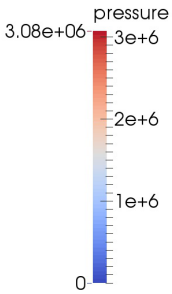

(b) Pore pressure distribution.

Figure 5.11: Simulation results of artificial rock tested with $p_{pore} = p_{conf} = 0.1$ MPa. Results shown at the moment of failure of the rock.

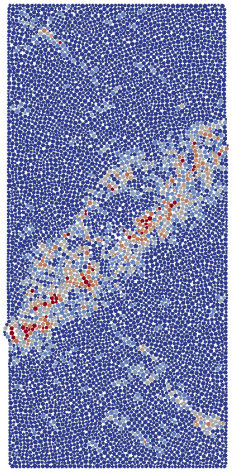

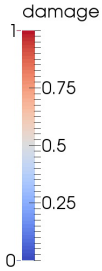

(a) Damage distribution.

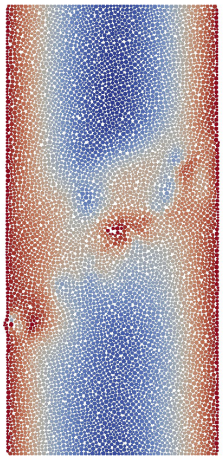

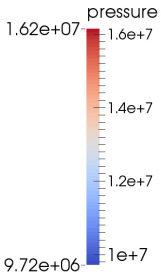

(b) Pore pressure distribution.

Figure 5.12: Simulation results of artificial rock tested with $p_{pore} = 0.1$ MPa and $p_{conf} = 16$ MPa. Results shown at the moment of failure of the rock.

5.2.2. Strain rate effects

In this section, biaxial compression simulations with varying strain rate are compared with experiments on Kimmeridge Bay shale, as those are described by Swan et al. (1989). Only few references are found that describe bi- or tri-axial compression tests with varying strain rates on rock samples, simulated in DEM. Zhang and Wong (2013) performed an analysis of strain rate effects on gypsum in uniaxial compression tests in DEM with a bonded particle model. In Zhang and Wong (2014) a further extended this analysis based on data from literature to the effect of loading rate on uniaxial compression tests on rock-like materials in DEM. Most other publications that deal with DEM and a rock-like material are based on split Hopkinson bar tests (both tensile and compressive), e.g. Li et al. (2013), or are based on impact loading of debris falling down or impacted at high velocity, e.g. Carmona et al. (2008); Zhao et al. (2017). Biaxial tests with varying strain rates in DEM are also applied in DEM for modeling of granular media, e.g. (Singh and Luding, 2010; Stahl and Konietzky, 2010). Although these are not directly applicable for rock-like materials, those simulations can help to obtain insight in the effect of friction between particles and particle shapes on the residual strength of a fragmented rock specimen.

5

Swan et al. (1989) performed two series of experiments on Kimmeridge Bay shale in which they investigated the effect of strain rate on the deformation, strength and failure properties of the rock. In the first, no drainage of pore fluid could occur across the sample boundary. The deviatoric stress is applied at the required constant rate of axial deformation. In the second series, isotropic consolidation was achieved under fully drained conditions. Upon completion of the isotropic loading they closed the drainage lines and the deviatoric stress applied under nominally undrained conditions, as in the first series. Swan et al. (1989) performed experiments at various confining pressures, of which most of the experiments were done at a confining pressure of 50 MPa.

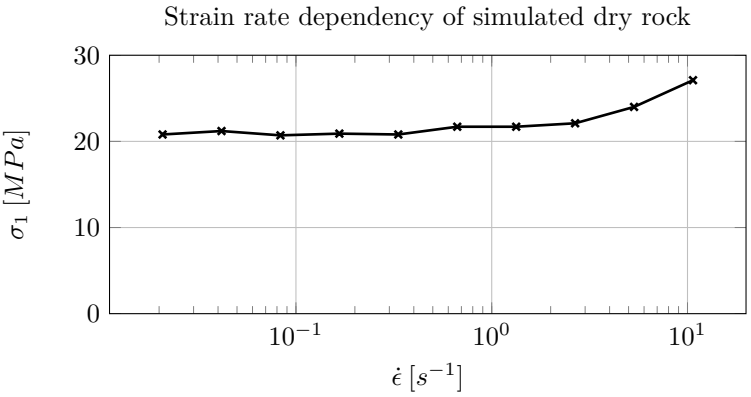

Figure 5.13: Strength simulated dry rock with respect to applied strain rate

It is not possible to directly apply the strain rates in the simulations, due to the

large range in orders of magnitude. Not only the required computational time for the slowest strain rates would take too long, but also the strain rate dependency of the simulated dry rock is of influence, as is shown in figure 5.13. Zhang and Wong (2013) obtained a similar result, based on DEM simulations with varying strain rates in compression tests on gypsum blocks with a pre-existing flaw. The problem is that in the case of the higher strain rates, work is applied in a too high rate to ensure sufficient numerical damping to result in a realistic solution, which is also the reason why it is often stated that the velocities in the simulation need to be significantly smaller than the speed of sound of the artificial rock (Huang, 1999). The failure mechanism that is observed in simulated UCS-tests shows strong resemblance when in practice, equipment with a low stiffness is used (Hemami and Fakhimi, 2014). After failure, the strain energy that is stored in the machine needs to be released. If this release of strain energy allows for a large displacement, the failed specimen is immediately again loaded and the frictional strength of the failed specimen might get higher than the strength of the residual intact rocks, leading towards a higher apparent strength and a transition from brittle to ductile behavior. In order to simulate the strain rate effect, scaling of the intrinsic permeability is applied through the dimensionless number N, as in equation (2.15).

The simulation and experimental results of the unconsolidated compression tests and consolidated compression tests are shown in figures 5.14 and 5.15 respectively. The cumulative accoustic emissions (total nr. of broken bonds) measured in the simulations are shown in figure 5.16. Damage and pressure distribution of a sample tested at lower and higher Deborah number are respectively shown in figures 5.17 and 5.18.

5.2.3. Discussion

Based on figure 5.14, the critical strain rate for the shale occurs at a deformation rate with $N \approx 2.3 \cdot 10^5$. Below this value there is no significant increase in strength with increasing strain rate. For experiments with $N > 10^4$, a significant increase is noted. The strengthening rate of the DEM-SP seems less significant compared to the experiments. It needs mentioning that the simulation at $\lambda = 1.7 \cdot 10^9$ is basically the upper limit in strain rate dependency of the DEM-SP. Here the pore pressure diffusion is almost identical to the case where the rock is considered to be perfectly impermeable (i.e. $\kappa = 0$). Besides that, in this simulation it is also noted that the pore fluid in the macro crack is fully cavitating, resulting in a limited strengthening effect.

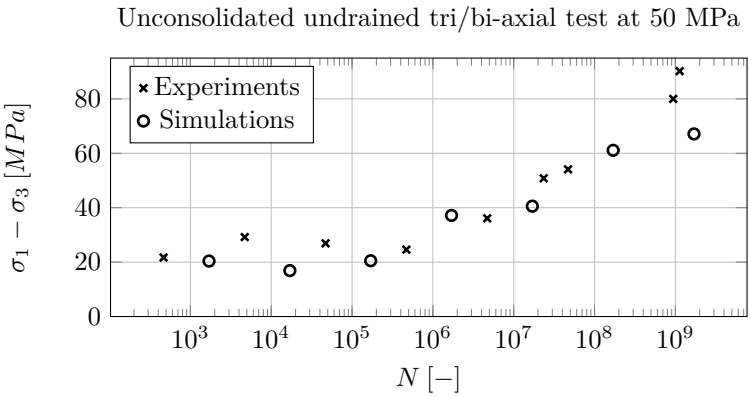

Figure 5.14: Unconsolidated tri-axial tests at 50 MPa confining pressure (experiments of (Swan et al., 1989)), compared with bi-axial simulations (2D). N is a representation of the Deborah number, as given in equation (2.15).

In the consolidated experiments and simulations both strengthening and weakening effects are observed, see figure 5.15. For experiments performed at $N < 10^4$, the material tends to weaken. Due to the compression that is applied to the samples, the volume decreases, resulting in an increase in pore pressure. This increase results in a lower effective stress and eventually in a lower strength of the sample. For experiments and simulations with $\lambda > 10^4$, dilative strengthening causes the strength of the samples to increase again. Both the weakening and the strengthening effect seem to be less pronounced in the simulations with respect to the experiments.

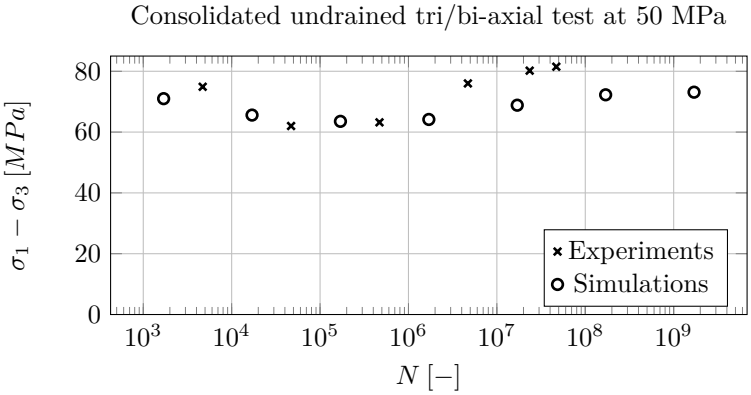

Figure 5.15: Consolidated tri-axial tests at 50 MPa confining pressure (experiments of (Swan et al., 1989)), compared with bi-axial simulations (2D). N is a representation of the Deborah number, as given in equation (2.15).

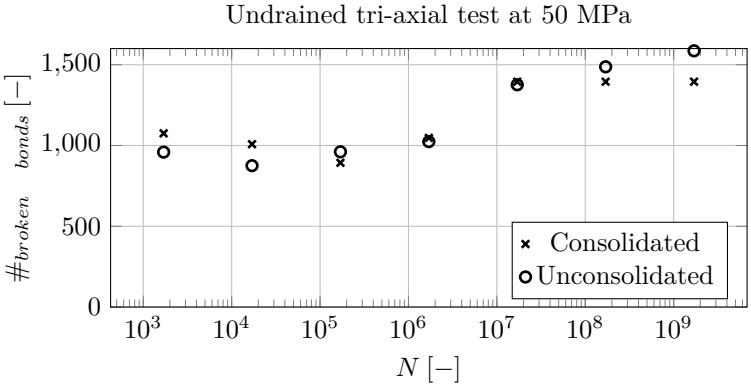

Figure 5.16: Number of broken bonds in simulations. N is a representation of the Deborah number, as given in equation (2.15).

The trend in the accoustic emissions with respect to the applied strain rate

corresponds with the observations of Rutter (1972), that with increasing strain rate, rock tends to show less strain softening (i.e. more ductile) and that the amount of damage (number of accoustic emissions) increases.

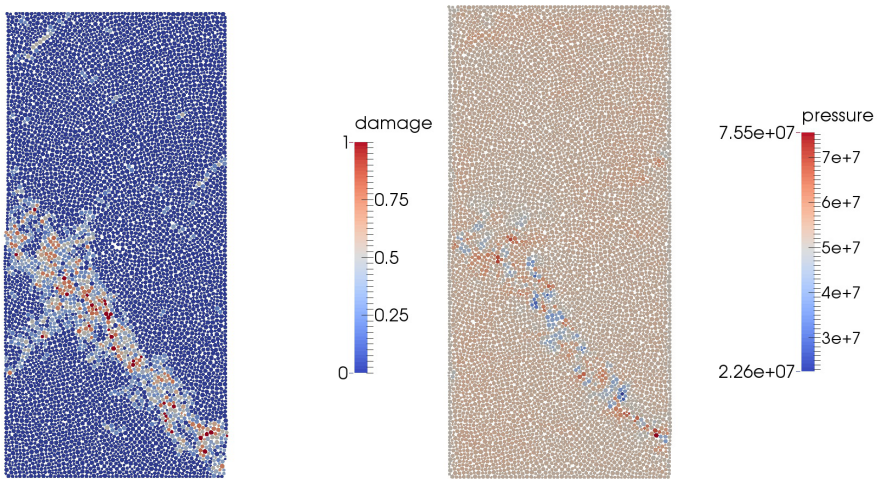

(a) Damage distribution.

(b) Pore pressure distribution.

Figure 5.17: Simulation results of artificial rock tested with $p_{pore} = p_{conf} = 50$ MPa and $N = 170$. Results shown at the instance of macro-failure of the rock.

Several drainage related mechanisms have been identified in simulations. The phenomena of compaction weakening, stiffening and the occurrence of cavitation correspond with the trends described in chapter2. Except for the occurrence of dilatancy hardening. In DEM-SP, the rock starts to dilate when the sample has already failed, while in practice, often the sample dilates before it fails (Bernabe, 1987). This is most likely caused by the strongly simplified geometry of the rock,i.e. the grains are idealized as circular particles, the simulations are based on 2D and not 3D. Additionally, near internal discontinuities (micro-cracks), the SP will smoothen the pore pressure, ignoring the local discontinuity.

5.3. Conclusions

A parameter sensitivity analysis is performed and analyzed with the use of the Buckingham-π theorem in which the microscopic input parameters for bond stiffness and bond strengths are varied for both UCS and BTS tests. The results show that for saturated conditions, given that a constant Deborah number is used, a decrease in compressive strength and strength ratio. Furthermore an increase in Young's modulus, Poisson ratio is noted. No significant differences with respect to the tensile strength of the sample are noted. Mechanical properties of DEM-SP filled with air simulations show little difference compared to DEM simulations without fluid coupling effects.

The DEM is found to be highly sensitive above a critical strain rate. Low strain

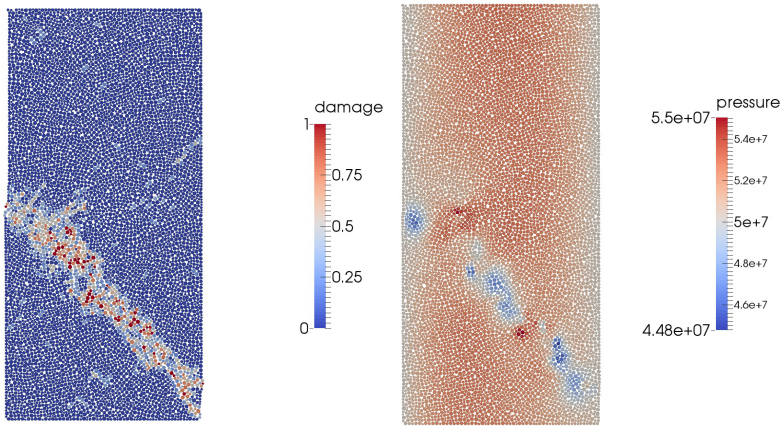

(a) Damage distribution.

(b) Pore pressure distribution.

Figure 5.18: Simulation results of artificial rock tested with $p_{pore} = p_{conf} = 50$ MPa and $N = 1.7 \cdot 10^7$. Results shown at the instance of macro-failure of the rock.

rates are undesirable in DEM due to the large increase in computational effort. Therefore strain rate effects on saturated rock should be modeled by scaling the Deborah number through permeability instead of strain rate.

It is shown that the effective stress theory is still valid when using the DEM-SP approach. Furthermore, tri-axial tests with varying strain rates on Kimmeridge Bay shale have been simulated and compared with experiments. Scaling of the strain rate in the simulations is achieved by scaling through the Deborah number by adjusting the permeability, instead of the applied strain rate. The results show that for the case where the initial pore pressure is equal to the hydrostatic pressure, an increase in strain rate first results in compactive weakening, and for a further increase of the strain rate dilatancy hardening becomes dominant. In the case that a higher hydrostatic pressure is used compared to the initial pore pressure, failure the resultant compressive strength of the samples increases significantly due to dilatant hardening.

Additionally, based on the results presented on the range in strain rate/permeability in the simulation, it is expected that the use of an adaptive permeability will be of lesser relevance to the model. Especially because in practice the uncertainties concerning the rock properties are already quite large, since rock is a natural material. For practical applications the accuracy of the model is thus limited by the tests that are done to measure the rock properties.

6

Validation - Tool-Rock Interaction

"The first principle is that you must not fool yourself and you are the easiest person to fool."

Richard Feynman

Several validation cases with respect to rock cutting processes are presented in this chapter. A set of simulations are compared to 2D rock (tile) cutting experiments that are performed on dry artificial rock. Additionally, the method is used to compare the tool-rock interactions that are more comparable to the practices of the industry. One set of simulations based on a confining stress is compared to drilling experiments. A comparison is also made between the DEM-SP methodology and the existing techniques found in literature. Another set of simulations comprises the effect of water depth on the rock cutting process for deep sea mining applications. These results are also validated with experimental results found in literature. As a test case, the cutting motion of a single tooth on a cutter head is simulated.

Section 6.3 is based on improved simulations of those published in Helmons et al. (2015).
Section 6.4 has been published in Helmons et al. (2016a).
Section 6.5 has been published in Helmons et al. (2016c).

6.1. Introduction

Through the 1970's till the beginning of 1990's, an extensive research program on rock cutting processes was commissioned by the Dredging Research Association (in Dutch: Commissie Speurwerk Baggertechniek, nowadays Stichting Speurwerk Baggertechniek, currently the joint research organisation of Boskalis and Van Oord) to Delft Hydraulics and Delft Geotechniques (now Deltares). Within this research program, emphasis was on the cutting processes that are of relevance to the, in dredging commonly used, crown cutter. Some of the experiments are made available to use for validation in this thesis. These are the 2D tile cutting experiments (Meijer, 1972, 1973b,a).

As already described in section 4.2, several researchers modeled the confining stress in the drilling process as a boundary condition in the simulations, inherently assuming dry rock material. The DEM-SP method is used to recreate the cases described by Kaitkay and Lei (2005) in order to show that application of a confining stress in the DEM gives proper results.

Furthermore, experimental data concerning the rock cutting process at hyperbaric ($p_h > \sigma_c, \sigma_t$) conditions Alvarez Grima et al. (2015) for deep sea mining purposes, carried out by Royal IHC, is publicly available and can be used for validation. On a similar type of rock, the effect of both hydrostatic pressure and cutting velocity have been tested.

As a test case for dredging applications, the cutting process of a single tooth mounted on a cutter head is simulated. Other than the results of the high pressure cases in drilling and deep sea mining, in dredging the range in hydrostatic pressure is limited to 30m (0.3 MPa). Additionally, all cutting models presented in chapter 3 and all cutting simulations performed in this thesis thus far are based on linear cutting. Most significant differences in rotational compared to linear cutting are the non constant cutting depth and that the tool no longer moves in a direction parallel to the rock bed.

The various aforementioned cases of tool-rock interactions are discussed in this chapter. Each of these cases starts with a brief overview of the experiments performed, although these experiments were not performed with this thesis in mind. Therefore, for sake of completeness, a brief description of these experiments is presented. This is then followed by the input parameters and simulation geometry setup for these experiments. The simulated results, after post-processing, will be compared with the experimental results. At the end of this chapter, an overall discussion of the presented tool-rock interactions is given.

6.2. 2D tile cutting

6.2.1. Experiments

The experiments, described by Meijer (1972, 1973b), consist of a chisel that is pushed into a tile of artificial rock. The thickness of the tile is smaller than the width of the tool to ensure a 2D cutting process. The force needed to cut the tile is generated a hydraulic cylinder. The cylinder pushes a cart on which the tool is mounted to enforce a linear movement of the tool into the tile. A force sensor is

positioned between the cylinder and the cart. The height and angle of the chisel can be altered. The chisel is pushed at a velocity of 1 mm/s into the rock. See figure 6.1 for a schematic overview of the test setup. The movement of the tool stopped when a large chip occurred, limiting each experiment to one chip.

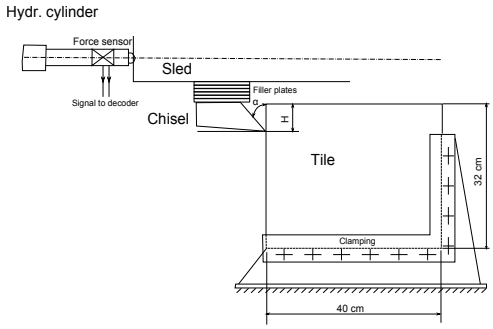

Figure 6.1: Experimental setup used for the tile cutting experiments, as in (Meijer, 1972, 1973b).

The experiments are performed on tiles artificial rock with dimensions 40 x 32 x 2 cm. The artificial rocks are based on the mixture as given in table 6.1. The material properties of the artificial rock are presented in table 6.3, together with a comparison of the material properties of the simulated rock. The Young's modulus of the tiles in the experiments was not measured. Its value for the simulations is estimated as approximately $450 \cdot \sigma_{UCS}$, which is comparable for an average type of limestone, see appendix A.

Table 6.1: Mixture components for artificial rock used in 2D tile cutting experiments

Component	$\%_{mass}$
Sand	69.2
Cement	13.3
Water	13.3
Clay	3.5
Calcium-chloride	0.7

Results and comparisons of the cutting forces and penetration depth are presented in respectively tables 6.4 and 6.5. A comparison between the typical chip shapes that are obtained in the simulations and experiments is shown in figure 6.2.

6.2.2. Discussion

As depicted in table 6.4, the required cutting forces correspond well with those observed in experiments. All of the simulated results lie within one standard deviation (std) from the mean cutting force measured in the experiments. Although, at smaller cutting depths, the simulated results seem to underestimate the required cutting forces. With respect to the penetration depth, these values can significantly

Table 6.2: Input parameters for tile cutting experiments in DEM-SP

Symbol	Quantity
k_n [N/m^2]	$5.0 \cdot 10^9$
k_s [N/m^2]	$5.0 \cdot 10^9$
T_n [N/m]	$1.25 \cdot 10^4$
T_s [N/m]	$1.25 \cdot 10^4$
μ [-]	1.0
$r_{min} - r_{max}$ [mm]	$0.5 - 1.0$
$\bar{r}$ [mm]	0.75
Δt [s]	$3 \cdot 10^{-7}$
$\#_{particles}$ [-]	56179
v_c [m/s]	0.03125

Table 6.3: Mechanical properties of rock used in 2D tile cutting experiments. Material properties are found in (Meijer, 1972, 1973b)

Property	Experiment (mean - std)	DEM-SP
σ_{UCS} [MPa]	11.38 - 0.88	10.36
σ_{BTS} [MPa]	1.17- 0.08	1.17
E [GPa]	Unknown	4.51

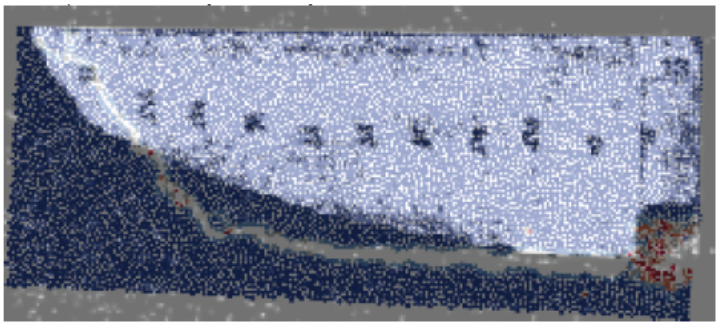

Figure 6.2: Comparison of chip shape of simulations and experiments, with $\alpha = 45°$ and $t_c = 6.5$ cm. Simulated results depict damage, blue being intact and red completely disintegrated.

differ from those observed in the experiments. First of all, calculations of penetration depths that small in DEM, i.e. $t_p \approx \bar{r}$ are prone to discretisation errors. The simulated rock is not a perfect block, but an assembly of finite sized particles that are connected together. Hence, the penetration depth is strongly influenced by at which exact location the tool enters the rock, i.e. whether the tooltip moves directly towards a particle center or whether it moves exactly between two particles can make a big difference, see figure 6.3 for clarification.

Table 6.4: Tile cutting forces obtained in experiments and simulations. Experimental data is found in (Meijer, 1972, 1973b)

Rake angle α [°]	Cutting depth t_c [m]	Experiments F_c [kN] (mean - std)	DEM-SP F_c [kN]
45	3.5	1.589 - 0.216	0.915-1.122
30	6.5	1.97 - 0.216	2.2
45	6.5	1.76 - 0.39	1.68-1.8
60	6.5	1.69 - 0.177	1.243-1.767
30	6.5	1.97 - 0.216	2.2

Table 6.5: Tile cutting penetration depth obtained in experiments and simulations. Experimental data is found in (Meijer, 1972, 1973b)

Rake angle α [°]	Cutting depth t_c [m]	Experiments t_p [m] (mean - std)	DEM-SP t_p [mm]
45	3.5	1.22 - 0.36	0.3
30	6.5	1.97 - 0.216	2.2
45	6.5	1.29 - 0.38	2.6
60	6.5	2.21 - 0.55	5.8

The shape and size of the chips generated both in the experiments and simulations correspond well. The simulated chip shows a less smooth crack trajectory than those in the experiments. This is likely caused by the limited brittleness of the simulated rock. In the current model, only shear and normal bonds are incorporated, which restrict deformation in normal and in tangential directions along the particle bonds, but it does not restrict the bending moment that particles can make. This might be improved upon by using the parallel bond model of Potyondy and Cundall (2004).

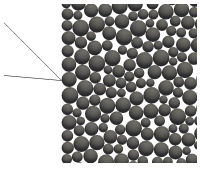

(a) Attacking particle through center

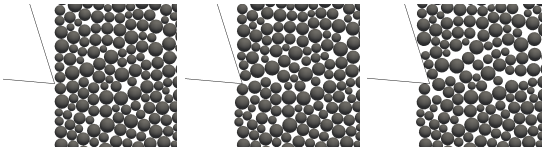

(b) Attacking between particles

Figure 6.3: Discretisation effects in tool - rock interactions

6.3. Drilling

In this section, the DEM-SP approach is validated against the experimental data on drilling experiments of Kaitkay and Lei (2005). These experiments are especially interesting because Lei and Kaitkay (2003) also tested their DEM-based modeling approach against these results, allowing for a comparison between their method and the DEM-SP approach.

6.3.1. Experiments

The single point cutting experiments are performed on Carthage marble. The rock sample is placed in a pressure vessel in which the desired hydrostatic pressure is applied. Vertical feed and the rotary motion of the cutter are controlled. Table 6.6 lists the machining conditions tested by Kaitkay and Lei (2005). The properties of the Carthage marble samples they have used are presented in 6.7. The DEM-SP requires that for a reasonable solution of the cutting process, a cutting depth of at least several particles needs to be achieved. The particle size is chosen in such a way that on average the cutting depth is five particles deep. In order to limit the computational expense of the simulations, a smaller block with a height of 0.016 m and a width of 0.05 m is used, similar to the size used by Lei and Kaitkay (2003).

Table 6.6: Machining conditions for drilling experiments, (Kaitkay and Lei, 2005).

Parameter	Setting
Feed	0.8 [mm/r]
Cutting speed	1 [m/s]
Rake angle	-15, -25 °
External pressure	0.1, 3.44, 34.4 [MPa]

Table 6.7: Properties of Carthage marble and simulated rock.

Property	Carthage marble Lei and Kaitkay (2003)	DEM-SP
E [GPa]	44.8	41.8
ν [-]	0.24	0.21
σ_c [MPa]	103	105
σ_c at $\sigma_{2,3} = 34.5$ [MPa]	186	154
σ_{BTS} [MPa]	unknown	14

The input parameters used in DEM-SP are shown in table 6.8. The compressive strength at high confining pressures does not match, the current implementation of the DEM models does not allow for such an increase in strength with confining pressure. On the other hand, Cunningham and Eenink (1959) already showed by experiments that the differential pressure (bottomhole - pore pressure) has a more profound effect than the increase in compressive strength of the rock due to the confinement of the differential pressure. Furthermore, the tensile strength of the

simulated material is given. Unfortunately, the tensile strength of the rock used in the experiments is not mentioned (Kaitkay and Lei, 2005). Fixed displacement boundary conditions are applied on the particles at the bottom and right end of the rock specimen.

Table 6.8: Input parameters used generate the simulated rock as in 6.7.

Symbol	Quantity
k_n [N/m^2]	$7 \cdot 10^{10}$
k_s [N/m^2]	$2 \cdot 10^{10}$
T_n [N/m]	$2 \cdot 10^4$
T_s [N/m]	$1.3 \cdot 10^4$
μ [-]	0.75
$r_{min} - r_{max}$ [mm]	$0.0533 - 0.01067$
$\bar{r}$ [mm]	0.08
Δt [s]	$1 \cdot 10^{-8}$
p_h [MPa]	$0.1 - 34.5$
h [m]	$4 \cdot 10^{-4}$

Care must be taken when analyzing the data of Kaitkay and Lei (2005), as the data presented at atmospheric conditions is actually based on a different type of experiment. The experiments at elevated pressure are performed with the drill axis parallel to gravity, while the experiments at atmospheric conditions are performed with the drill axis perpendicular to gravity and without a confining fluid, see figure 6.4 for clarification. The drill bit is positioned such that the generated debris falls to the side of the bit (in DEM-SP that would mean out of plane movement of the debris).

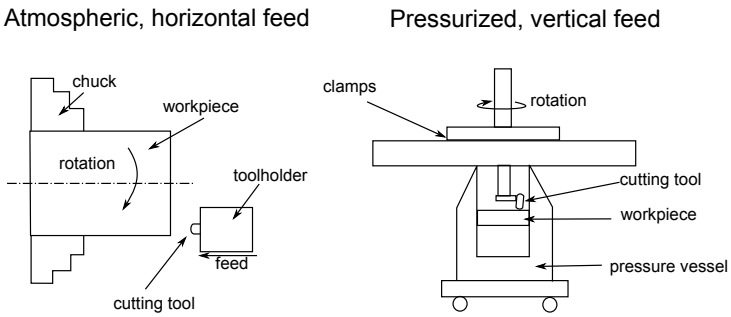

Figure 6.4: Experimental setups as used by Kaitkay and Lei (2005).

6.3.2. Simulated results

Figure 6.8 shows a set of image sequences representing the damage that occurs during the cutting process with a rake angle $\alpha = -15°$ at atmospheric conditions and at confining stress $p_c = 34.5$ MPa. Because of its negligible effect on the cutting process, gravity is neglected in this simulation. That is why the large horizontal ribbon of debris occurs at atmospheric conditions. The force signals of both simulations are shown in figures 6.5 and 6.6 for respectively the horizontal and vertical direction.

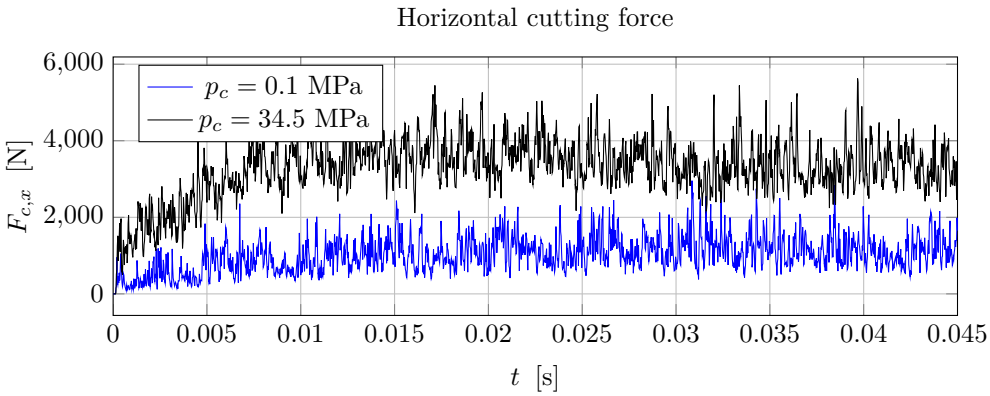

Figure 6.5: Horizontal cutting force over time for both atmospheric and high pressure confinement (34.5 MPa) with rake angle of -15°.

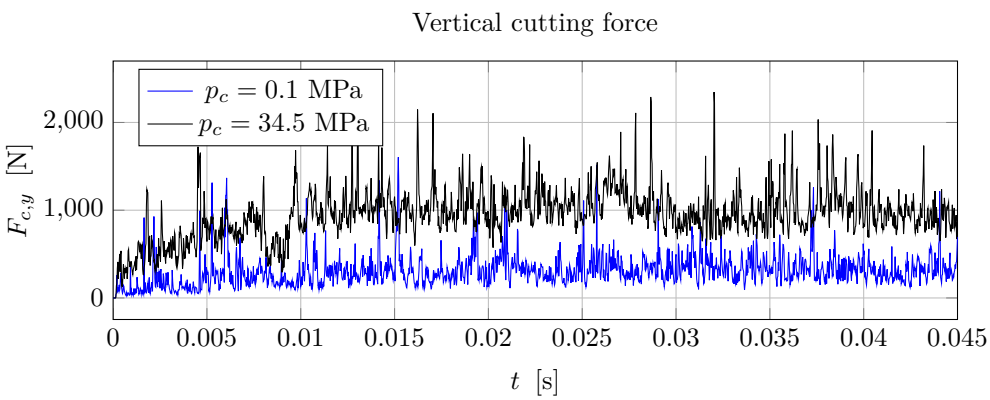

Figure 6.6: Vertical cutting force over time for both atmospheric and high pressure confinement (34.5 MPa) with rake angle of -15°. The tendency is that the tool will be 'pushed' out of the rock.

The damage inflicted over time in both cutting processes is shown in figure 6.7. More simulations are performed to investigate the behavior of the cutting process

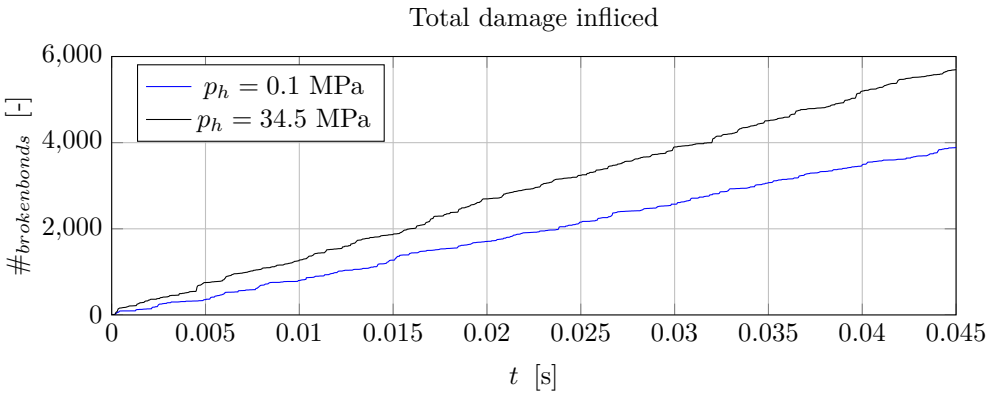

Figure 6.7: Total number of accumulated broken bonds over time for both atmospheric and high pressure confinement (34.5 MPa) with rake angle of -15°.

with respect to the confining stress, for confining stresses ranging from $0.1 - 34.5$ MPa and for both rake angles $\alpha = -15, -25°$. The time averaged cutting forces, both horizontal and vertical are respectively shown in figures 6.9 and 6.10. The cutting forces as predicted by Lei and Kaitkay (2003) and the experimental results of Kaitkay and Lei (2005) are also shown in these graphs. The total damage applied over time for each of the simulations is shown in figure 6.11.

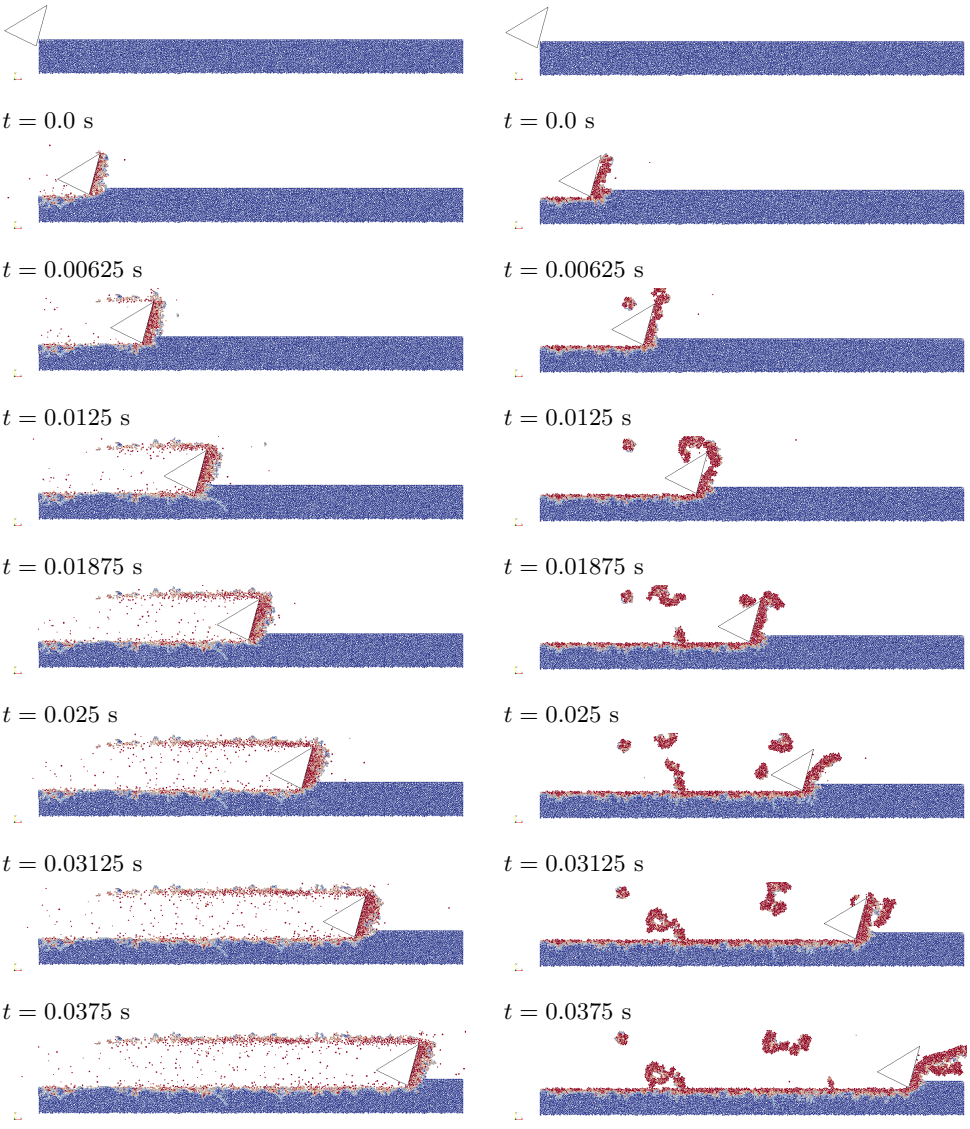

(i) No confining stress.

(r) At confining stress $p_h = 34.5$ MPa.

Figure 6.8: Damage of cutting simulations with $\alpha = -15°$. For damage, red corresponds with fully disintegrated particles and blue corresponds with perfectly intact material. Note that only the top layer where observable changes occur is shown in the figures

6.3.3. Discussion

A significant difference in behavior is noted between low and high pressure conditions. At low confining stresses, the debris generated behaves much like a granular flow and separate small clusters and single particles move freely away from the cutting process. At high confining stresses a continuous chip is generated and at some extent this chip can curl up (balling as described by Zijsling (1987) and theoretically calculated by Miedema and Zijsling (2012)). It seems that the curling up of the chip in front of the tool gives no significant effect on the cutting force. Furthermore it is shown that the friction area of the chip along the face of the bit changes over time. Based on the number of experiments that are performed thus far it is not yet possible to give a more in depth analysis on the curling behavior of the chip.

The type and amount of damage that is applied to the non-cut rock differs as well when comparing low and high confining stresses. At low stresses, the total damage to the rock is lower and some cracks that move deeper into the virgin rock are shown. At high confining stresses the amount of damage that is applied to the virgin rock is significantly larger and it shows little to no damage deeper into the virgin rock. The highly damaged layer acts like a filter cake, as described in chapter 3.

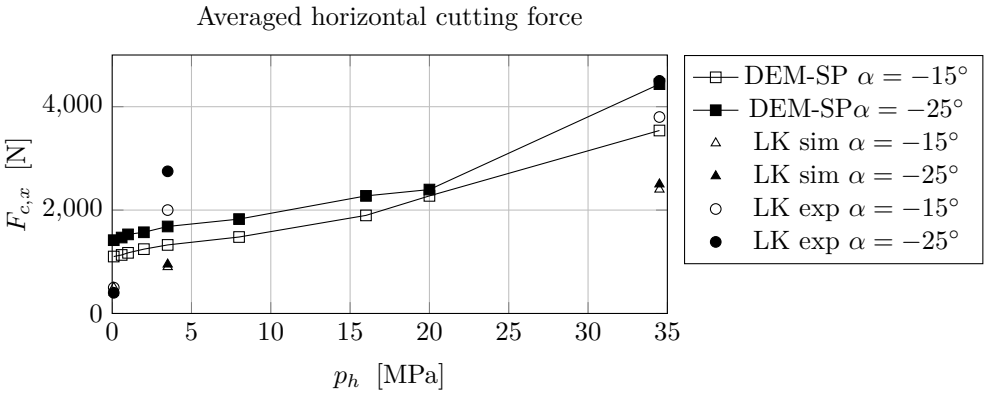

Figure 6.9: Time averaged horizontal cutting force with varying confining pressures.

In the graphs showing the cutting forces, although highly rapid fluctuations are noticed, the mean cutting force over time does not differ significantly. The spikes in these graphs are a result of the stress build until bonds break. The highest spikes are a result of the discretisation, depending on where the tool touches on a specific particle and whether it has some mobility whether such a spike can occur, as is discussed in previous section 6.2.

The time averaged components of the cutting forces of the simulations in figure 6.9 and 6.10 show a similar trend to the drilling experiments of Kaitkay and Lei (2005). Although the vertical cutting force significantly underestimates the cutting force as measured in the experiments (approx 50-60 %). The cutting forces as

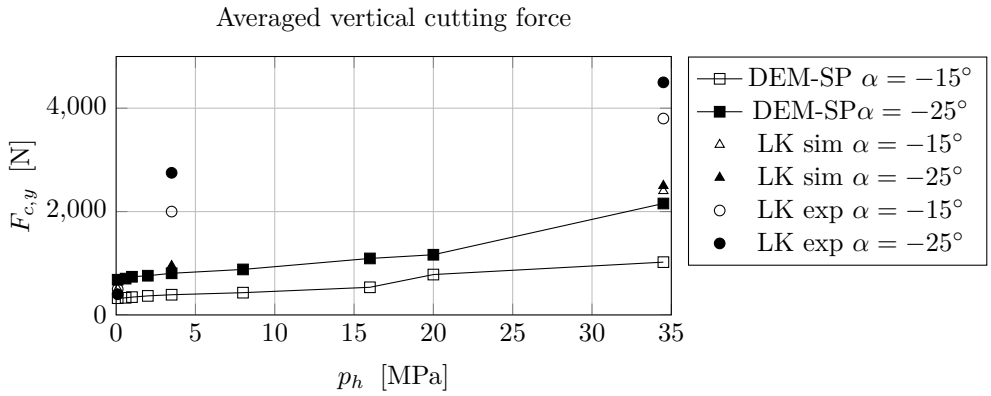

Figure 6.10: Time averaged vertical cutting force with varying confining pressures.

simulated with DEM-SP show closer resemblance with the experiments in horizontal direction compared to the simulated method of Lei and Kaitkay (2003). In vertical direction, no significant differences are noted with respect to the simulations of Lei and Kaitkay (2003).

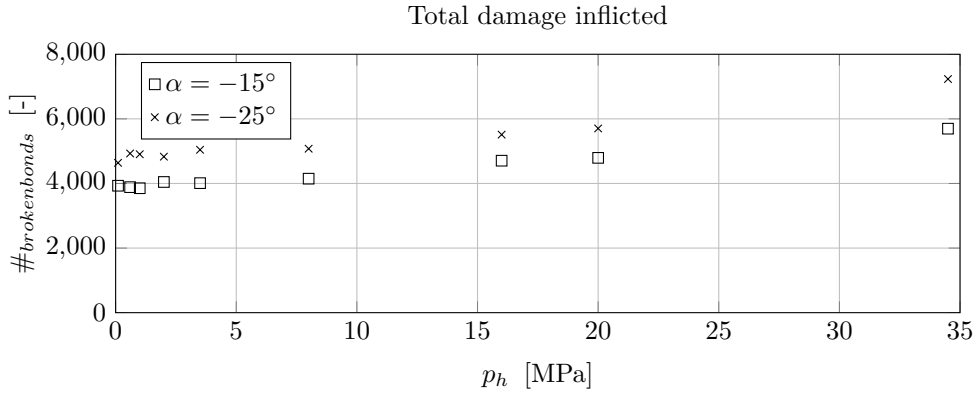

Figure 6.11: Total number of accumulated broken bonds over time, presented for varying confining pressures.

The improvement shown by DEM-SP can be due to the higher level of detail in the cutting zone, a layer of on average five particles thick is being cut in DEM-SP while Lei and Kaitkay (2003) cut a layer of one particle thickness. Additionally it might be that their chain method causes some unrealistic results, as is shown by Mendoza Rizo (2013). It could as well be that both arguments are valid.

Only the cutting force at atmospheric conditions is significantly overestimated. As mentioned before, this experiment is performed with a different setup, which

might lead to the significantly different cutting force. Simulations with lower tensile strength ($\sigma_{BTS} = 10$ MPa) at confining stress $p_c = 0$ and 34.5 MPa did not result in a significant decrease ($< 10\%$) in cutting force that might explain the difference. In the cutting theory of Miedema (2014) and in the experiments of Zijsling (1987) this such a transition as depicted by Kaitkay and Lei (2005) might not be present when all experiments are performed with the same setup.

Total damage over time that is applied in the cutting process shows a linear trend with increasing confining stress for both rake angles. The trend corresponds with expectations, that with increasing confining stress the cutting process goes through the brittle-ductile transition.

6.4. Dredging and (Deep) Seabed Mining

The DEM-SP with fluid pressure effects has been applied to the simulation of linear rock cutting tests using a 2D geometry. Both the pore Peclet number and the water depth (assuming both internal pore pressure and ambient pressure are initially in equilibrium) are varied in the set of simulations. The rock specimen is discretized using 96 991 cylindrical elements with a uniform particle size distribution with radii 0.2-0.4 mm. The cutting tool is discretized in 1050 straight line segments with a maximum length of 0.4 mm per line segment. As a boundary condition, the position of the particles at the bottom and the right end of the slab is fixed. For the fluid counterpart, all boundary particles are subsequent to Dirichlet boundary (ambient hydrostatic pressure). Except for the particles that are in contact with the cutting tool, there a Neumann boundary is applied (no fluid flow through the cutting tool).

The geometry of the tooth and the rock properties that are used are based on the experiments of Alvarez Grima et al. (2015). Linear rock cutting simulations are carried out on a block with dimensions 0.1 and 0.35 m. The tooth is placed at a cutting angle of 68 ° and has a clearance angle of 10 °, is 95 mm in height and the tip of the tool has a width of 21 mm. In the 2D simulations, the cutting force is calculated per unit thickness. Therefore the cutting force is scaled with the width of the cutting tool. A fixed timestep of 11.25 ns is used and the data is stored every 1250 timesteps, resulting in a sampling frequency of 7.1 kHz.

Table 6.9: Micro (input) and macro (output) parameters used in the rock cutting simulations.

Input parameters		**Output parameters**	
	Micro parameters (DEM)		
k_n	10 GPa	σ_{UCS}	9.89 MPa
k_s	2.5 GPa	σ_{BTS}	1.47 MPa
T_n	10 kNm^{-1}	E	8.03 GPa
T_s	20 kNm^{-1}	ν	0.28
μ	1		
R	0.0002-0.0004 m		
α_d	0.7		
ρ	2800 kgm^{-3}		
	Fluid parameters (SP)		
κ	$\mathcal{O}\left(10^{-16} - 10^{-14}\right)$ m^2		
n	0.18		
h	0.0015 m		
M	2 GPa		
μ_{fluid}	0.001 Pas		
α_{eff}	0.5		

The micro and macro parameters used are shown in table 6.9. The properties of the rock are chosen such that they are well within the range of the measured rock properties in the experiments of Alvarez Grima et al. (2015). These macroscopic

parameters are obtained by calibration of the micro-parameters on both UCS and BTS tests. Several simulations have been performed in which the permeability and the ambient pressure are varied. Here the permeability is used to mimic a change in cutting velocity in the simulation. Decreasing the cutting velocity in the simulation would result in a too large computational expense. Note that for the weak type of rock that is modeled in this study, the contact bond model is sufficient. When simulating tougher rock types, it is advised to extend the contact bond model to the parallel bond model (Potyondy and Cundall, 2004).

6.4.1. Results

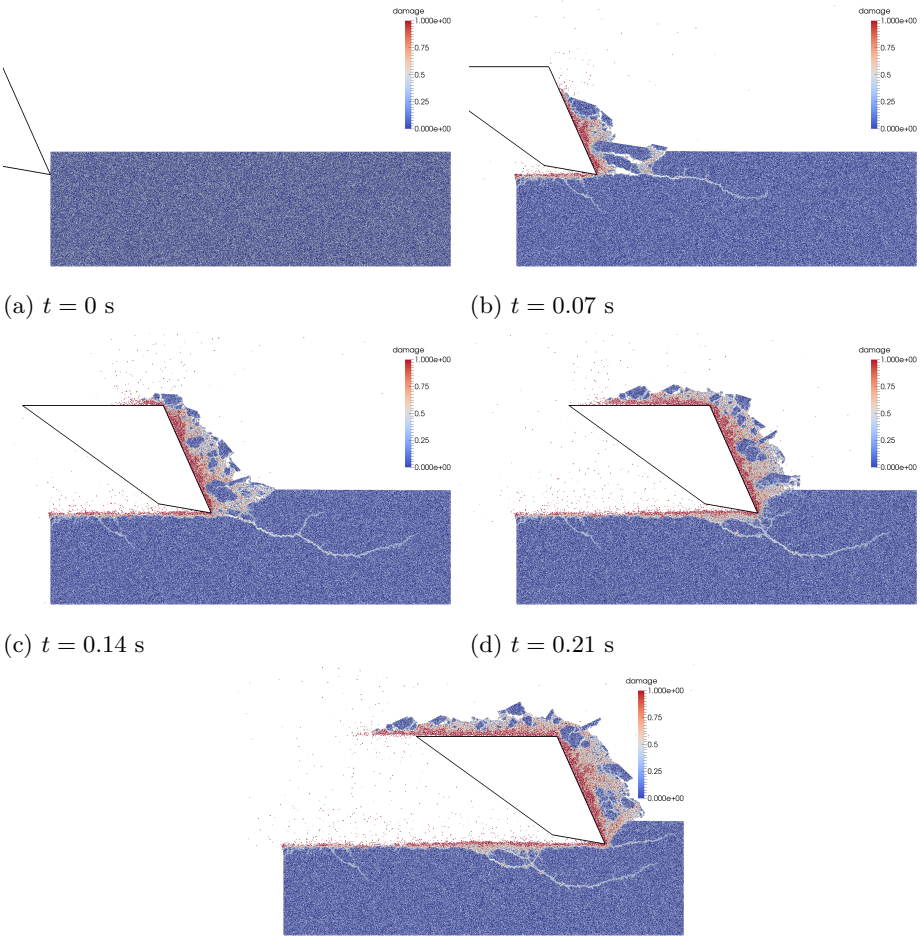

(a) $t = 0$ s

(b) $t = 0.07$ s

(c) $t = 0.14$ s

(d) $t = 0.21$ s

(e) $t = 0.28$ s

Figure 6.12: Damage for rock cutting simulation at atmospheric pressure, $p_h = 0.1$ MPa, and $\kappa = 10^{-14}$ m^2.

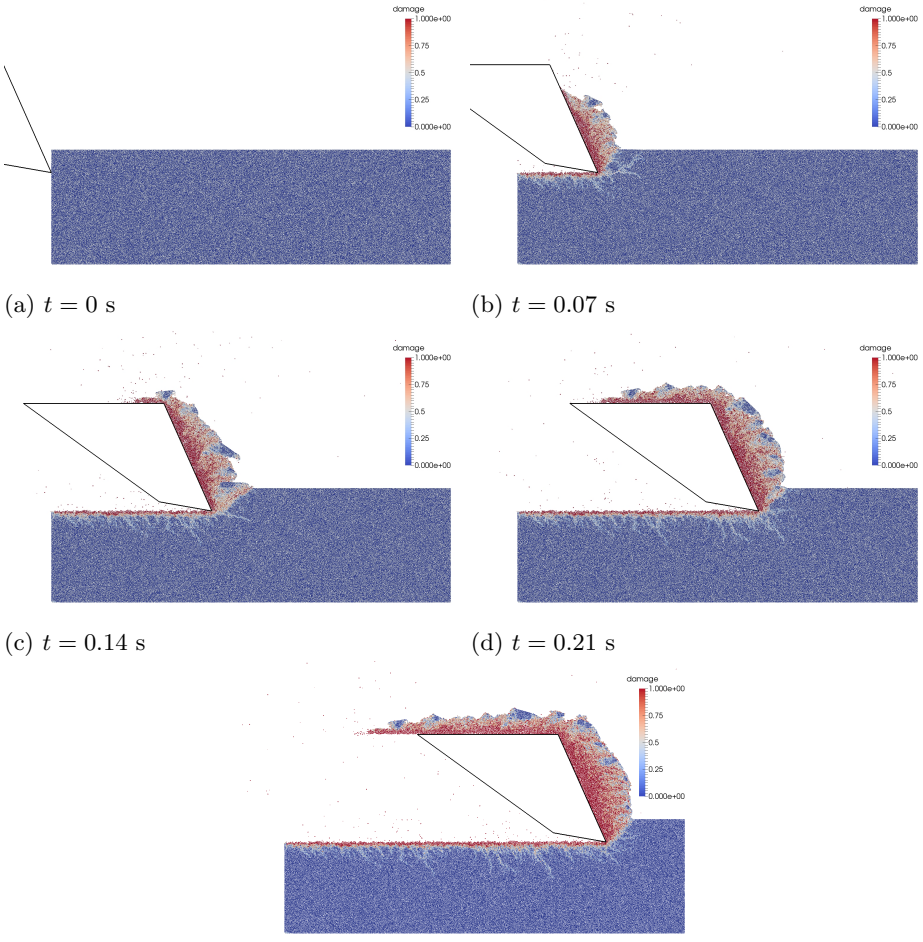

(a) $t = 0$ s (b) $t = 0.07$ s

(c) $t = 0.14$ s (d) $t = 0.21$ s

(e) $t = 0.28$ s

Figure 6.13: Damage for rock cutting simulation at $p_h = 10.1$ MPa and $\kappa = 10^{-14}$ m^2.

Image sequences of rock cutting simulations at both atmospheric and 10.1 MPa ambient pressure (comparable to 1 km water depth) are presented in figures 6.12 and 6.13. In both image sequences, the depicted damage is defined as

$$D = 1 - \frac{\#_{intact \quad bonds}}{\#_{initial \quad bonds}} \tag{6.1}$$

so that with $D = 0$ all bonds of the particle are still intact and with $D = 1$ all bonds of that particle are broken.
The total cutting force with respect to time is shown in figure 6.14. The total force is calculated by summation of all force vectors acting on the surface of the tool. The averaged total cutting force components for various ambient pressures and

permeabilities are shown in figures 6.15 and 6.16. Start-up effects are omitted by determining the average cutting forces in the range of 0.07-0.28 seconds. Although it is shown in figures 6.12b and 6.13b that the front of the tooth is not yet completely covered with cut material, it has an insignificant effect on the total cutting force.

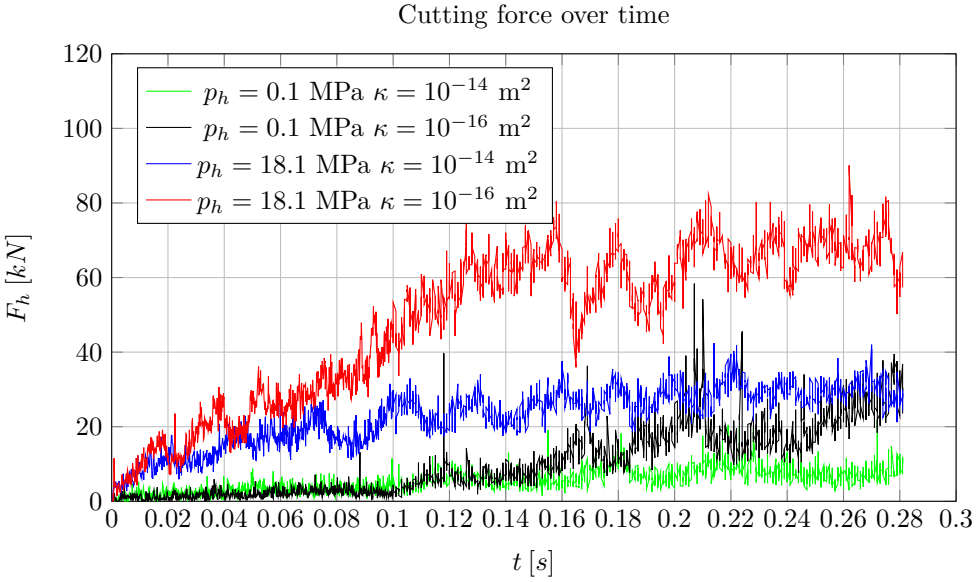

Figure 6.14: Horizontal cutting force over time for atmospheric and hyperbaric conditions.

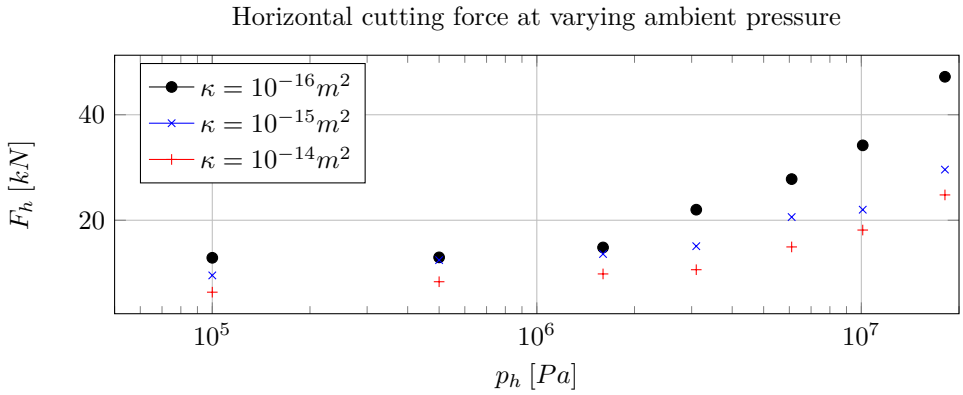

Figure 6.15: Simulated average horizontal cutting force with respect to varying ambient pressures. Cutting velocity is set at 1 m/s.

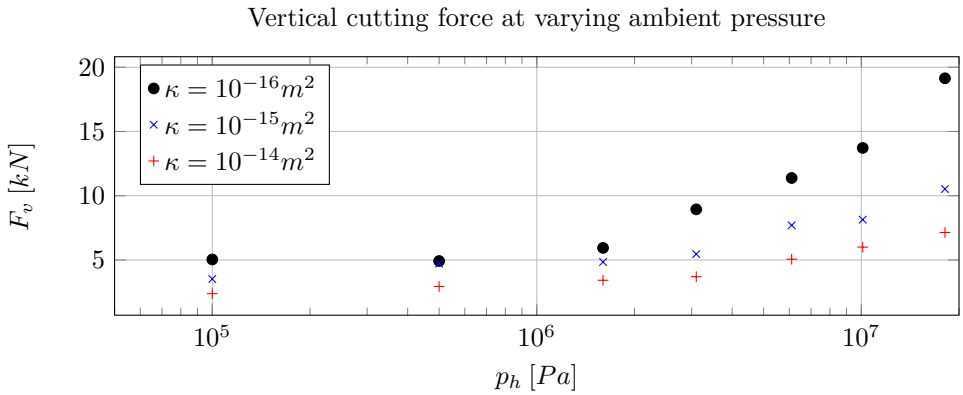

Figure 6.16: Simulated averaged vertical cutting force with respect to varying ambient pressures. Cutting velocity is set at 1 m/s.

Figure 6.17 shows a comparison for the total amount of damage incurred over time for the most diverse cases, i.e. atmospheric vs hyperbaric and low permeability vs high permeability. A comprehensive comparison of the total cumulative damage incurred at the end of all simulations is shown in figure 6.18.

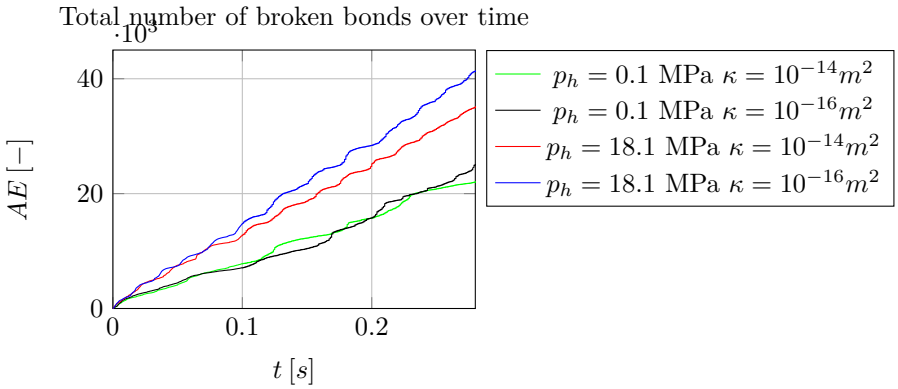

Figure 6.17: The number of broken bonds over time for atmospheric and hyperbaric conditions.

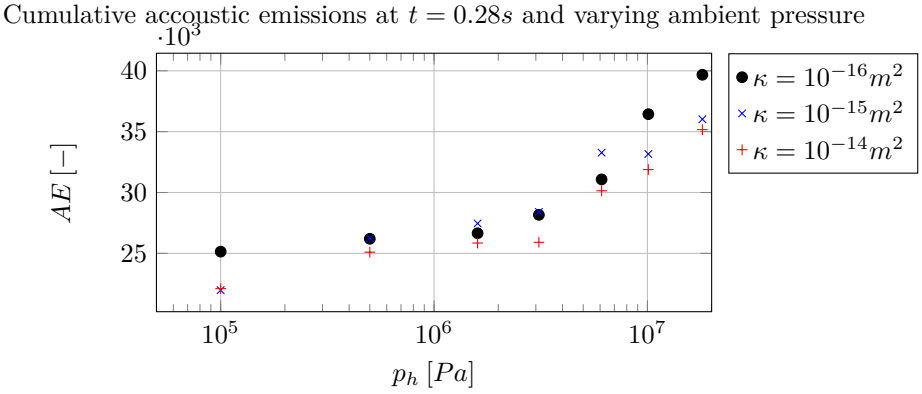

Figure 6.18: Number of broken bonds at the end of the simulations. Hydrostatic pressure and permeability of the rock are varied.

Two different regimes can be distinguished, being tensile dominated and shear dominated cutting. The transition is observed in both the cutting force components and the amount of damage inflicted to the rock, see figures 6.15, 6.16 and 6.18. For higher permeabilities, this transition occurs at approximately $p_h = 3$ MPa, while for the less permeable rocks this transitions seems to occur at $p_h = 1.5$ MPa. The first regime occurs at low ambient pressures, the rock cutting process is dominated by the occurrence of large chips that are created by long macroscopic tensile cracks. The second regime occurs at higher ambient pressures ($p_h > 2 - 3\sigma_{BTS}$) is dominated by shear failures that result in smaller chips and further fragmentation of

the cut material. A similar effect can be noticed in figures 6.14 and 6.17, where the frequency of stress build-up and release through brittle failure increases with increasing ambient pressure. The transition from tensile dominated to a shear dominated cutting seems to correlate with the BTS value of the simulated rock, i.e. the transition is at a hydrostatic pressure with a magnitude of 100-200% of the BTS value depending on the rocks permeability.

The simulations show qualitatively that the size of the crushed zone increases with increasing water depth. This can be observed when comparing figures 6.12d and 6.13d. Pore collapse and particle crushing are failure modes that can occur in the crushed zone van Kesteren (1995), while these failure phenomena are not considered in the current DEM modeling approach. The bonds between the particles can fail in either tensile or shear mode, while the particles themselves cannot fail. In this research, particle crushing is considered to be of lower significance on the cutting process compared to the fluid pressure effect, see section 2.3.2.

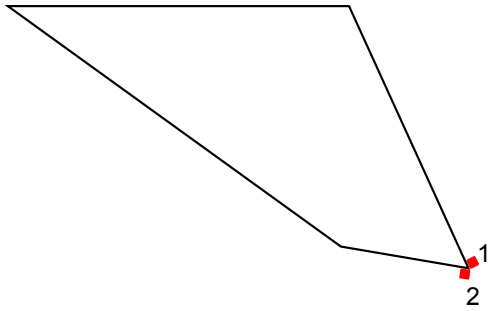

Figure 6.19: Location of the pressure measurements with respect to the shape of the tool. The area over which the pore pressures are measures is a square with 2x2 mm.

More interestingly, with the use of simulation techniques it is possible to investigate effects that are difficult to measure, like the pore pressure at the tip of the tool. The averaged pore pressure over time at the tip of the tool is measured at two different positions with respect to the tool. The position of these measuring areas are shown in figure 6.19. Measurements of these pressure sensors are shown in figures 6.20 and 6.21. Note that there are no particles present in the first few time steps of the simulations to determine the excess pore pressure in the sensor regions. For the set of simulations, the time averaged excess pore pressures with respect to the hydrostatic pressure are shown in figures 6.22 and 6.23. An impression of an instantaneous spatial pore pressure distribution during a cutting simulation performed at $p_h = 18.1$ MPa and $\kappa = 10^{-14}$ m^2 is shown in figure 6.24.

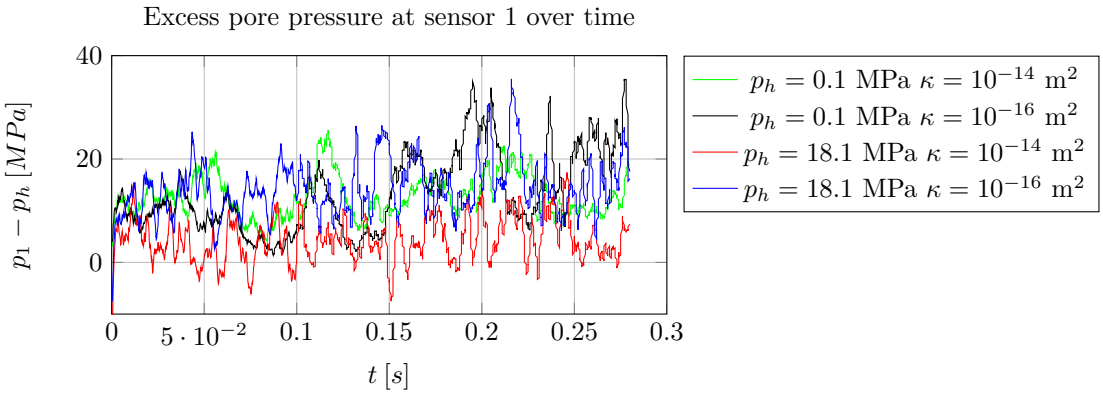

Figure 6.20: Excess pore pressure over time, measured at the front of the tip of the tool (position 1, as depicted in figure 6.19). Note that there are no particles present in the first few time steps to measure a pore pressure.

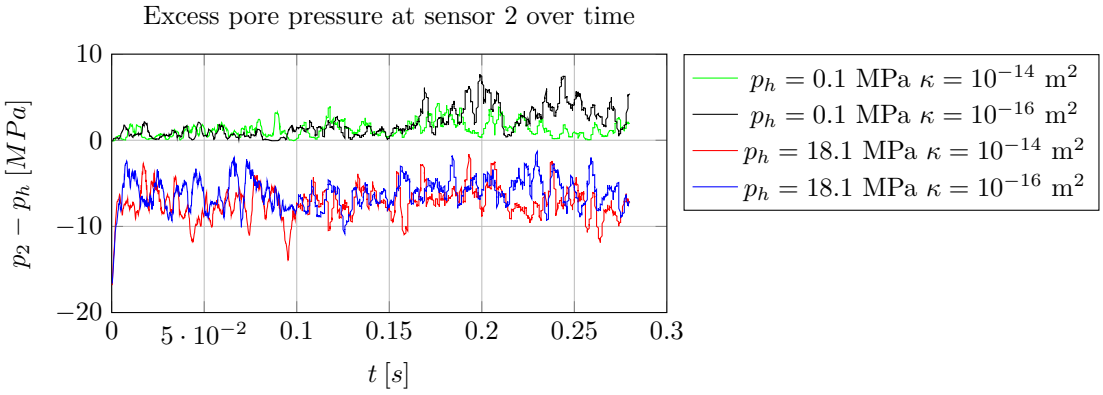

Figure 6.21: Excess pore pressure over time, measured at the front of the tip of the tool (position 2, as depicted in figure 6.19). Note that there are no particles present in the first few time steps to measure a pore pressure.

The simulations show that in the crushed zone (at pressure sensor 1, figure 6.22), the averaged pore pressure increase with respect to the hydrostatic pressure is constant. To what extent this pore pressure increase occurs, seems to depend on the permeability of the rock, i.e. a lower permeability leads to a higher pressure increase in the crushed zone. Below the tip of the tool a different trend is observable (see figure 6.23). At low hydrostatic pressures an increase in pore pressure is measured while at large hydrostatic pressures, the average pore pressure below the tool seems to decrease. It is not yet fully understood why this happens.

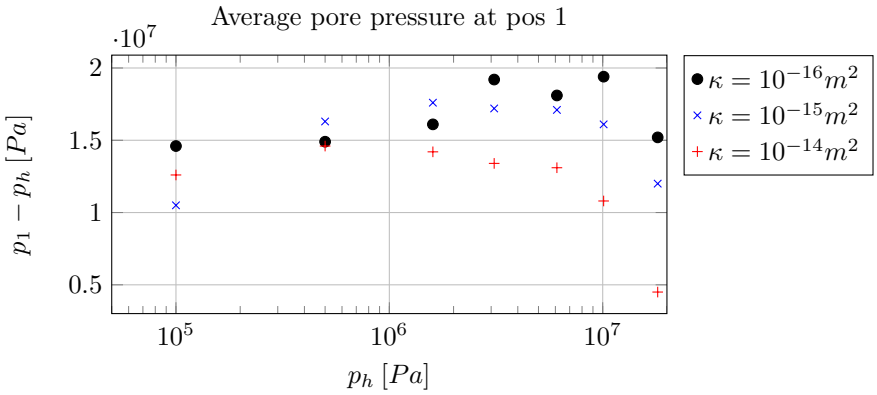

Figure 6.22: Averaged pore pressure with respect to hydrostatic pressure, measured at the front of the tip of the tool (position 1, as depicted in figure 6.19).

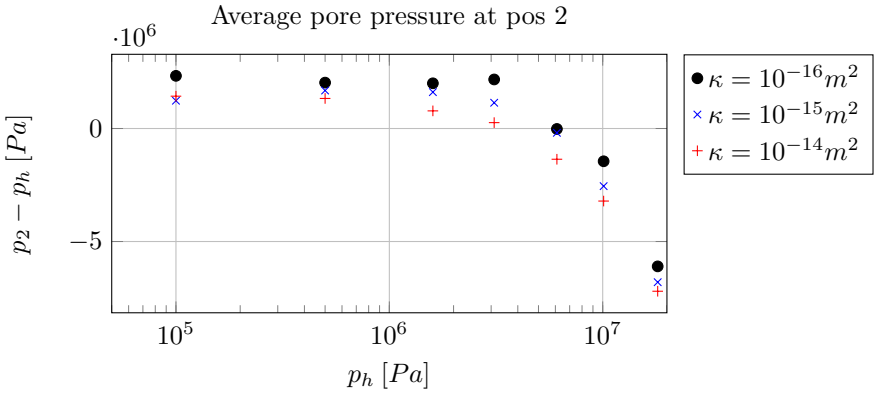

Figure 6.23: Averaged pore pressure with respect to hydrostatic pressure, measured at bottom of the tip of the tool (position 2, as depicted in figure 6.19).

A possible explanation for the decrease in pore pressure below the tool might be that in front of the tool due to dilation in the shear zone, fluid has to flow from the surrounding regions. As depicted in figure 6.24, a lower pore pressure region is present directly beneath the tip of the tool. Due to differences in the maximum

achievable pressure gradient (limited by p_h), the amount of fluid flow from this region can differ. Interesting to mention as well, even at $p_h = 18$ MPa, the simulations show that the rapid deformations applied to the rock still might result in cavitation of the pore fluid, as is depicted in figure 6.24.

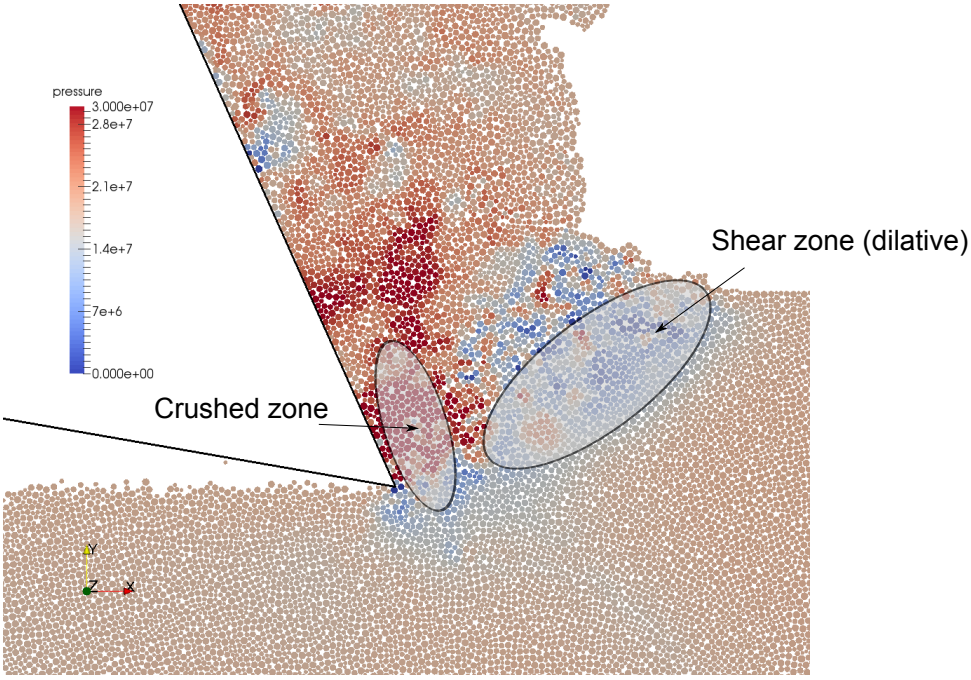

Figure 6.24: Pore pressure distribution in simulation with $p_h = 18.1$ MPa, $\kappa = 10^{-14}$ m^2 at t=0.14 s. Note that cavitation occurs (dark blue)

6.4.2. Comparison of numerical and experimental results

Although Alvarez Grima et al. (2015) have used multiple blocks with a slight deviation in the material properties, for sake of simplicity only one set of macro-parameters are used in the simulations, see table 6.10 for an overview of the compared data. The simulated macro-properties are well within the range of the measured properties in the experiments, except that the tensile strength is slightly overestimated in the simulations. In the current implementation, the maximum achievable brittleness ratio (given by $\frac{\sigma_{UCS}}{\sigma_{BTS}}$) is limited to approximately 7. Due to the wide range of hydrostatic pressures (up to $2\sigma_{UCS}$) it is assumed that a matching compressive strength is of higher importance compared to a matching tensile strength of the rock. For that reason we favored the UCS over the BTS value to match the experiments. Figure 6.25 shows a comparison for the averaged cutting forces with respect to water depth for both the experiments and simulations. Also the range of the minimum and maximum forces measured in the experiments is shown to give an impression of the fluctuations with respect to the average cutting force.

Table 6.10: Comparison of material properties and experimental setup of Alvarez Grima et al. (2015) and the simulations.

Test no.	σ_{UCS} [MPa]	E [GPa]	ν [-]	σ_{BTS} [MPa]	κ [m^2]	n [%]	v_c [ms^{-1}]	p_h [MPa]	F_{avg} [kN]
1	7.92	5.95	0.31	0.88	3.1E-13	37.86	0.188	0	7.22
2	7.92	5.95	0.31	0.88	3.1E-13	37.86	0.178	18	9.25
3	7.92	5.95	0.31	0.88	3.1E-13	37.86	0.200	1.5	10.42
4	8.75	7.53	0.25	1.09	8.5E-14	34.64	1.826	0	8.09
5	8.75	7.53	0.25	1.09	8.5E-14	34.64	1.717	1.5	11.17
6	8.75	7.53	0.25	1.09	8.5E-14	34.64	1.740	3	12.23
7	8.75	7.53	0.25	1.09	8.5E-14	34.64	1.702	6	13.19
8	9.29	5.89	0.27	1.15	1.4E-14	33.17	1.577	18	20.70
9	10.62	8.32	0.23	1.05	2.8E-14	31.66	0.618	18	22.72
10	10.64	9.01	0.27	1.13	2.2E-15	33.92	0.010	18	4.94
11	8.86	8.20	0.31	0.86	1.5E-14	35.12	0.017	0	4.72
12	8.86	8.20	0.31	0.86	1.5E-14	35.12	0.202	3	11.36
13	8.86	8.20	0.31	0.86	1.5E-14	35.12	0.207	6	11.29
14	10.54	9.98	0.33	x	3.4E-16	35.89	1.238	18	12.74
15	10.54	9.98	0.33	x	x	x	1.188	6	10.90
DEM-SP									
	9.89	8.03	0.28	1.47	varies	17.86	1.000	varies	varies

The results obtained, as shown in figure 6.25, indicate that the most dominant effects regarding pore fluid effects, hydrostatic pressure and deformation rate, are well predicted. Unfortunately, no other clear trends can be distinguished based on the data presented in Alvarez Grima et al. (2015). In the case of lower hydrostatic

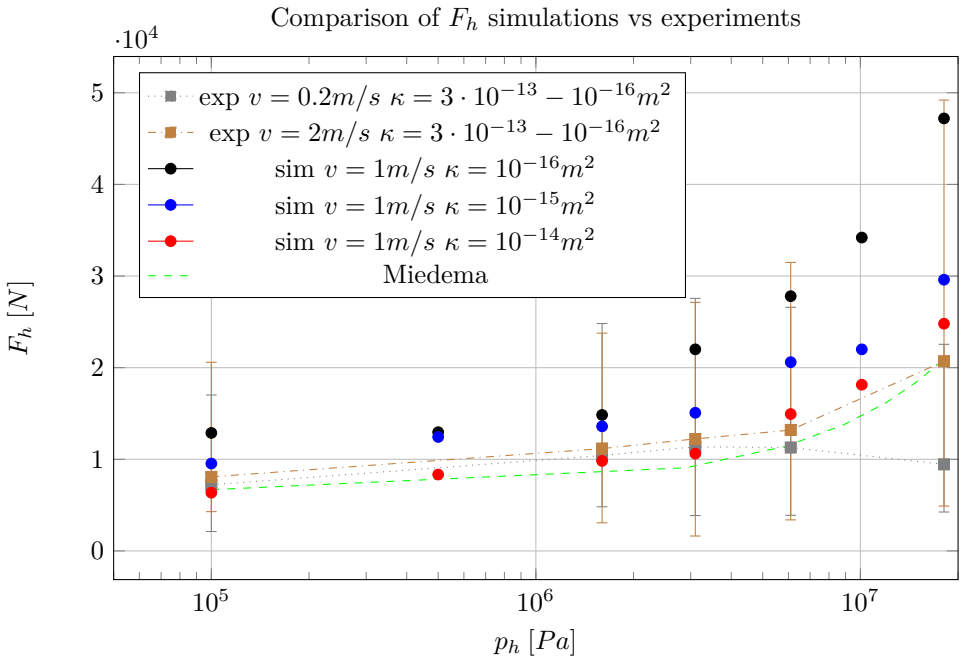

Figure 6.25: Comparison between experiments and simulations. Plot shows averaged cutting force with respect to hydrostatic pressure. The errorbars of the experiments correspond with the minimum and maximum measured cutting forces.

pressure (up to $p_h = 3.1$ MPa), the cutting force is slightly underestimated compared to the region at higher hydrostatic pressures. Most likely these phenomena are resultant to simulating a 3D process with a 2D method.

6.4.3. Discussion

At lower p_h, the side break out angle results in a larger area being cut than the width of the tool, while for higher p_h the side break out angle is almost 90° resulting in an almost perfect box cut, as observed by Alvarez Grima et al. (2015). Another effect caused by the 2D-3D conversion is where the cut material will move to. In 2D, the cutting process mimics an infinitely wide tool (tool width is used to scale the forces to practical applications), giving the debris that does not immediately move away from the tool has to move along and over the tool. A reason for the debris to 'stick' together is the fluid pressure coupling. Particles that get to distant from another will mimic dilation, resulting in a large local under pressure, which will be counteracted upon by the surrounding fluid pressure. In the current model, the permeability is assumed to be uniform and constant over time. Overestimation of dilation effects might be reduced when the permeability can change with changing porosity.

In 3D, the debris will be able to move to the side of the tool, reducing the amount of friction that the debris will exert on the tool. Another side effect of working with 2D simulations compared to 3D simulations is that most likely the normal component of the cutting force is underestimated (Rojek et al., 2011).

6.5. Testcase: rotational cutting

In this section, simulations based on the geometry and motion of a real cutterhead will be discussed.

6.5.1. Simulation setup

The input and output parameters of the simulated rock are shown in table 6.11. In this study, the parameters were chosen to represent a tight sandstone. On this rock, several cutting simulations are performed with a circular cutting motion, in which the cutter head moves with both an angular and a swing velocity, respectively with 1.62 $rads^{-1}$ and 0.2 ms^{-1}. The combination of the angular and swing velocities result in a cutting velocity of 1 ms^{-1}. The tool is modeled as a rigid body and its movement is prescribed. The water depth has been varied between 0 and 30 m and therefore the initial pore and hydrostatic pressures are respectively set to 0.1 and 0.4 MPa. In these simulations, a pick point positioned at a 26° angle (with respect to the radial direction) is used. In the circular cutting motion, the layer thickness starts at 0 m and will gradually increase to to 0.20 m. The geometry of the rock cutting experiment is shown in figure 6.26. No displacement boundaries are placed at the bottom and east side of the rock specimen by fully restricting the movement of the particles at these boundaries. Although the cutting velocity is lower than in common practice and the initial rock geometry is intact, these conditions are chosen for academic purposes.

Table 6.11: Input, output and geometrical parameters of simulated cutting experiment

Input parameters		Simulation	
K_n	20 GPa	σ_{UCS}	20 MPa
K_s	4 GPa	σ_{BTS}	3 MPa
T_n	100 kNm^{-1}	E	5 GPa
T_s	100 kNm^{-1}	v_c	0.2 ms^{-1}
μ_{grain}	0.8	ω	1.62 $rads^{-1}$
R	1 - 1.5 mm	Tool angle	64 °
α	0.5	Water depth	0-30 m
κ	$1 \cdot 10^{-17}$ m^{-2}	Tool width	0.02 cm
n	0.18		
ρ_{grain}	2800 kgm^{-3}		
h	0.005 m		
M	2 GPa		
μ_{fluid}	0.001 Pas		
$\mu_{tool-rock}$	0.5		

6.5.2. Simulated results

To give an impression of the cutting process, an image sequence of the simulation with water depth of 30 m is given in figure 6.27. This image sequence depicts

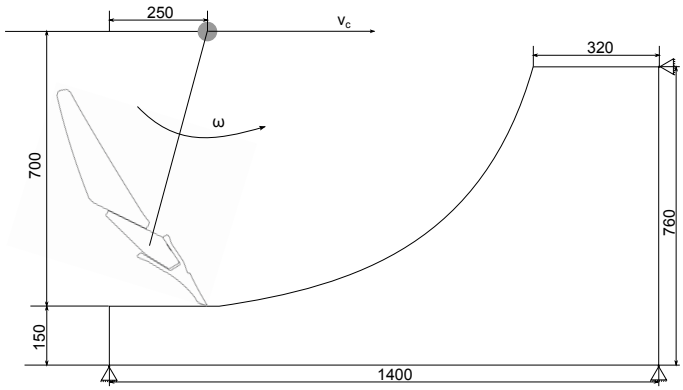

Figure 6.26: Model geometry for simulation of rock cutting with one pick of a dredge cutter head

the damage that is applied to the rock over time, with damage defined as $D = 1 - \frac{\#_{intact\ \ bonds}}{\#_{initial\ \ bonds}}$, where $D = 0$ corresponds with perfectly intact rock and $D = 1$ with fully disintegrated rock, all the bonds at that particle are broken. The pore pressure distribution during cutting is shown in figure 6.28. Note that in this figure a cavitating zone occurs deeper inside the rock, which is caused by the opening of tensile crack. At the same instance in time, an impression of the solid stresses, depicted as the Von Mises stress, is shown in figure 6.29.

In 2D, the simulations automatically adopt a unit thickness of the rock specimen. The thickness of the specimen has been scaled to the width of the tool (in this case 0.02 m), all forces and energies are scaled accordingly. In the simulations, a sampling frequency of 1 kHz is used. To allow for a better analysis, a moving average filter of 25 samples wide is used.

The total cutting force is calculated by integrating all resultant tool-grain contact forces over the whole area of the cutter tool, in both x- and y-components. The magnitude of the total cutting force is shown in figure 6.30. For each tool-grain interaction, the work delivered by the tool can be estimated by

$$E = \int m_i |\vec{v}_{lt}| dt = m_i |\vec{v}_{lt}| \Delta t \tag{6.2}$$

with particle mass m_i, local tool velocity v_{lt} and timestep Δt. Note that the work delivered by the tool in the interaction is corrected for the reversible energies of the grain (i.e. kinetic, normal strain and shear strain potential energy). The cumulative total work delivered by the tool is calculated by integrating all tool-grain interactions over the tool surface and in time. Figure 6.31 shows the cumulative total energy and its decomposition in local normal and shear directions.

The tip of the tool is especially of interest, since most of the work is done by this area. The tip has been analyzed for two small sections, the wear flat and the front of the tip. Both sections are 4 mm in length. These areas are shown in figure 6.32. Figure 6.33 shows the total forces that are applied by the tooltip regions. The direction of the force applied by the tooltip regions with respect to the tooltip

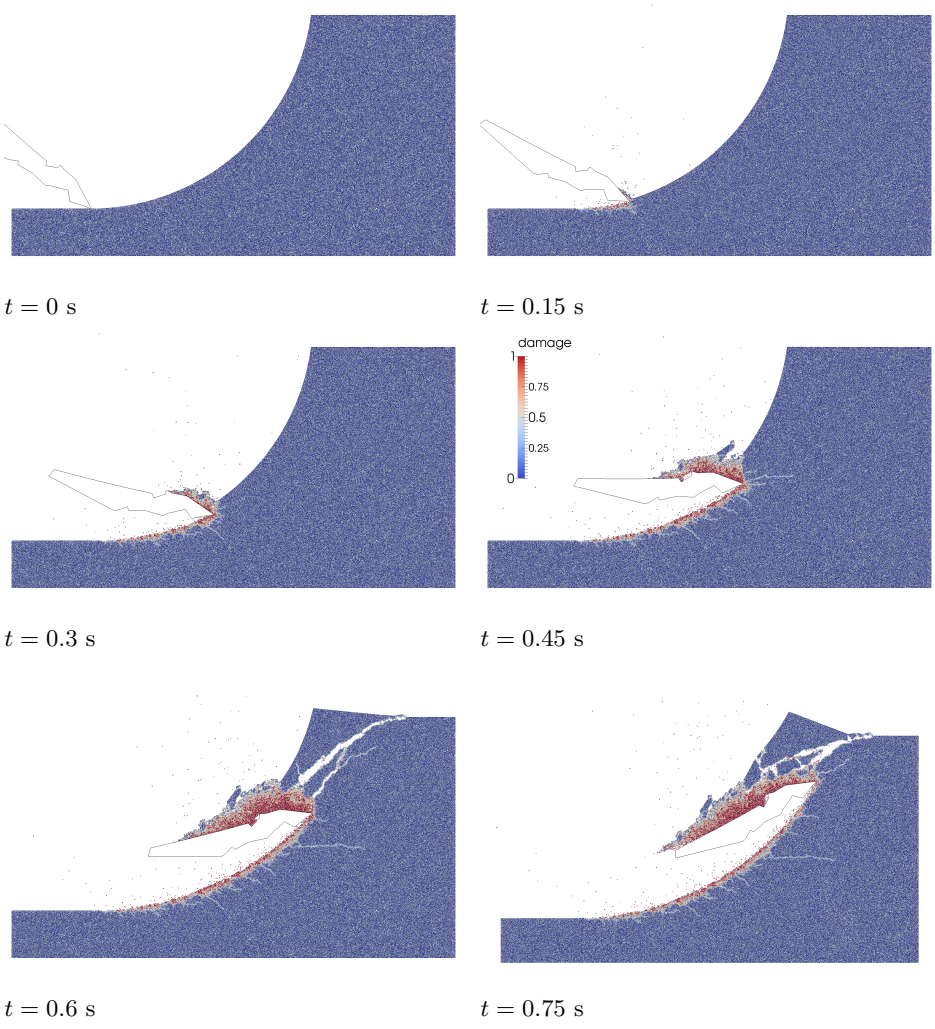

Figure 6.27: Damage occuring in simulation at 0 meter water depth (but still fully submerged, $p_h = 0.1$ MPa). Red corresponds with fully damaged particles (of which all bonds are broken) and blue with intact particles.

surface area is shown in figure 6.34 (0° corresponds with pure shear and thus 90° is perpendicular to the surface). Beneath and in front of the cutting tool, pore pressures tend to increase due to the compression of the rock (crushed zone). The averaged pore pressures directly below the tool are shown in figures 6.35 and 6.36, note that it only shows the pore pressure under the tip of the tool and not in front, most of the time there are too few particles in front of the tool to measure this. The total acoustic emissions (AE) in the simulation are shown in figure 6.37. The

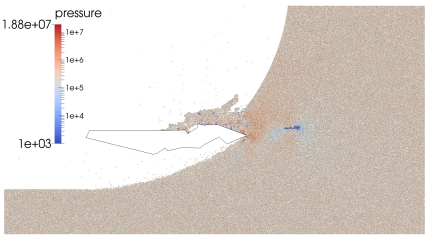

Figure 6.28: Pore pressures in simulation at $p_h = 0.1$ MPa at 0.45 s

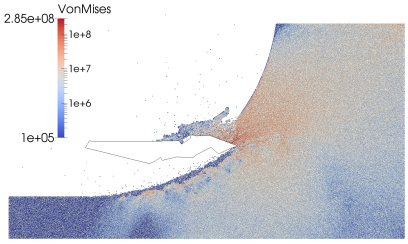

Figure 6.29: Von Mises stress contributions of the solids at $p_h = 0.1$ MPa at 0.45 s

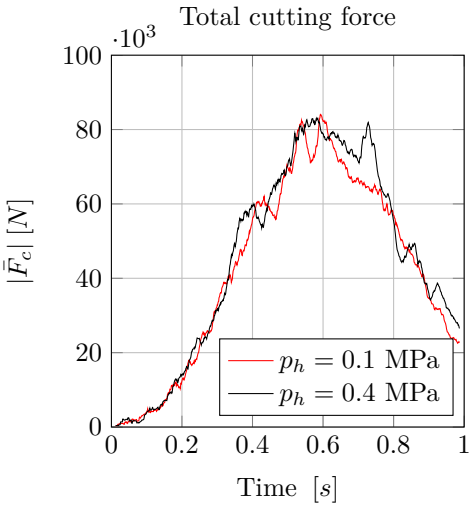

Figure 6.30: Magnitude of the cutting force integrated over the complete tool

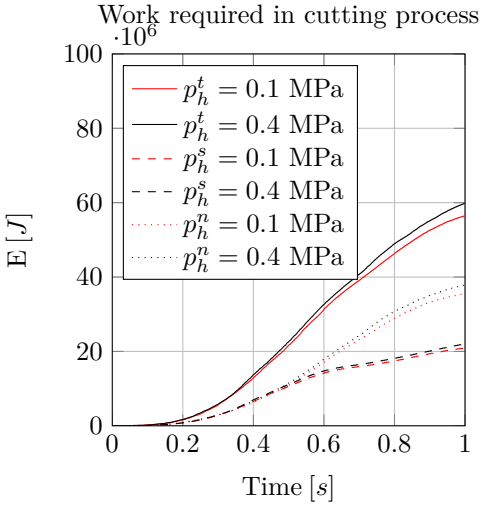

Figure 6.31: Total work required in cutting process. Superscripts ^{t},^{s},^{n} respectively give total work spent and it decomposition in shear and normal directions.

cumulative AE can be used as a means of estimating and comparing the amount of damage that has been induced to the simulated rock.

6.5.3. Discussion

Based on the total force applied by the cutting tool as in figure 6.30, three regimes can be distinguished:

1. Pseudo-ductile cutting ($0 < t < 0.15$): Here defined as the cutting process is dominated by complete fragmentation of the bonded particles into a granular

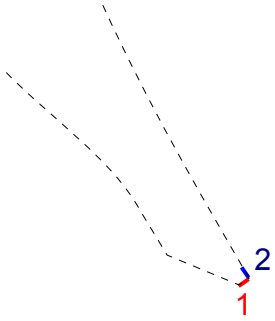

Figure 6.32: Detail of the tool tip. Area 1 corresponds with the wear flat and area 2 with the front of the tool tip.

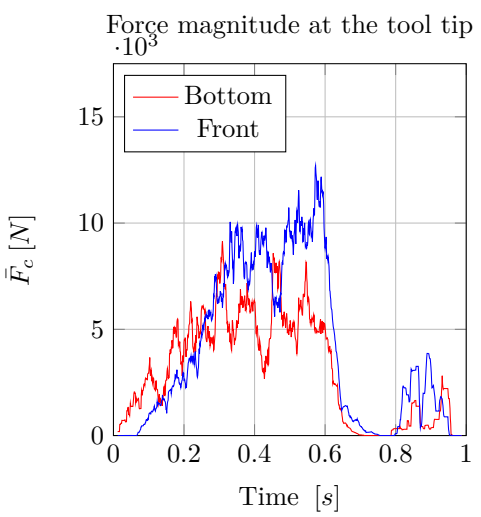

Figure 6.33: Magnitude of the cutting forces integrated over tool tip area, as shown in figure 6.32

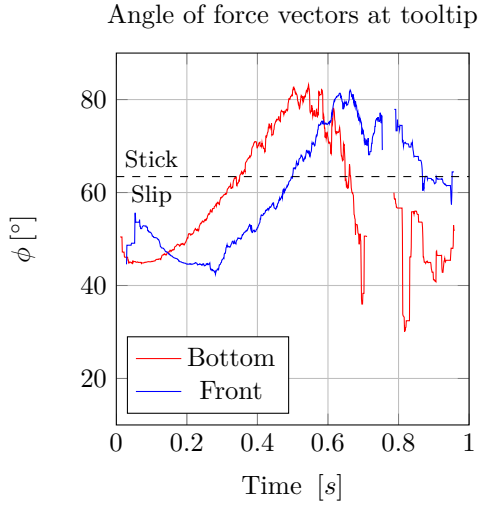

Figure 6.34: Angle of the cutting force with respect to the faces of the tip of the tool, as shown in figure 6.32. The dashed line corresponds with the stick-slip criterion

material, figure 6.27b shows no chips.

2. Brittle cutting ($0.15 < t < 0.6$): Within this range, chips can break close to the surface of the rock. It is noticed that the size of the chips increases with increasing cutting depth, as can be seen in figures 6.27c and 6.27d.

3. Edge chipping: The overburden of the intact rock is not sufficiently strong to further constrain the cutting process and a large chunk of material will be cut loose. This boundary effect causes a significant reduction in the cutting force.

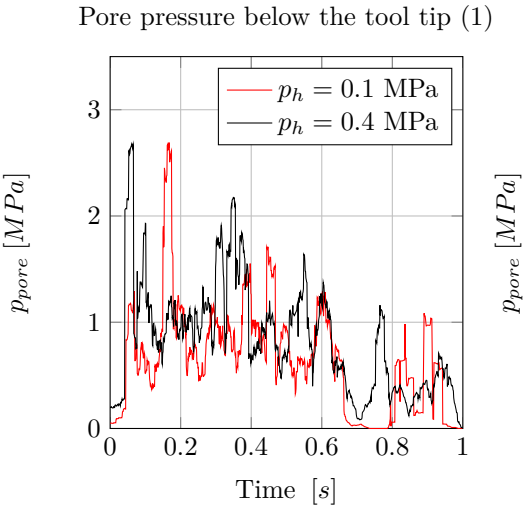

Figure 6.35: Averaged pore pressure distribution below the tip of the tool, measurement area is moving along with the tool

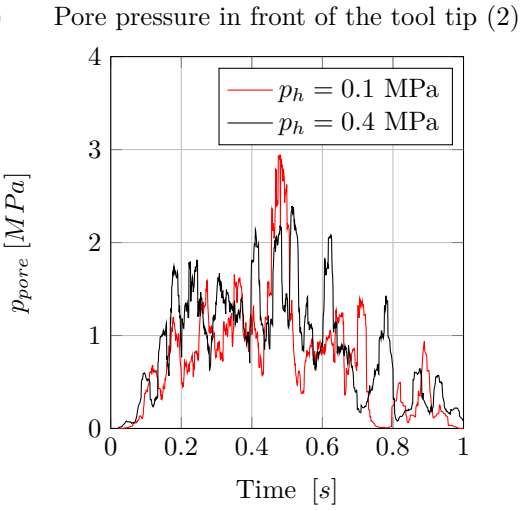

Figure 6.36: Averaged pore pressure distribution in front of the tip of the tool, measurement area is moving along with the tool

6

The cutting force does not drop to 0 due to the presence of a thin layer of rock that still has to be cut.

It is worth mentioning that the forces (and thus work delivered) in the various regimes have a different scaling effect when considering a 3D cutting process. In the pseudo-ductile cutting regime, the volume of rock that is affected grows spherically with respect to the layer thickness. Because of the complete destruction of the structure of the rock in this region, the energy and thus the force required to cut the material will scale with t_c^3. On the other hand, in the chipping regime with increasing volume, the surface of the cracks will scale with surface area and thus the required energy to cut the rock will scale with crack area (although fragmentation might occur), so the required energy will scale approximately with t_c^2. In practice it will be slightly higher, because for larger t_c fragmentation of the chip might occur.

When comparing the total energy required to cut through the rock, an increase of 30 meter of water depth compared to atmospheric pressure results in a 5 % increase of required energy. To allow for an objective comparison based on the same amount of rock removal and thus the contribution of the edge chipping effect is not considered (this would only be valid when many simulations are considered so that an averaged excavated production can be used). Based on the tensile strength of the simulated rock, a maximum energy increase of 10% could be expected (30 meter water depth difference is equal to 10% of the tensile strength) in the regime where tensile failure dominates the cutting process. However, that is based on the limiting situation that the process is sufficiently fast that the cracks instantaneously open,

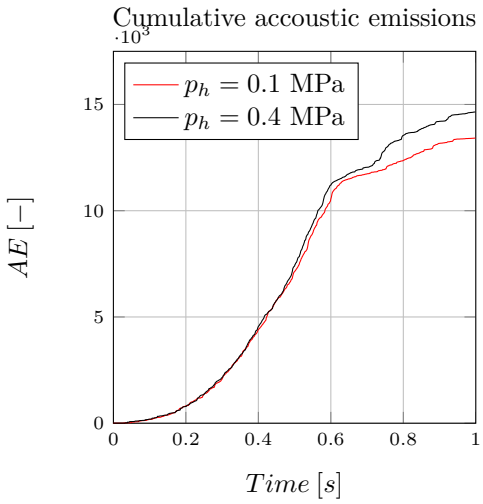

Figure 6.37: Accoustic emissions during cutting simulation at various water depths.

causing the lack of fluid in the cracks, resulting in a local underpressure which acts as an extra toughness for tensile failure. A similar analysis for the shear strength cannot be done without more detailed knowledge of the micro-structure. The effect of pore volume change in shear failure depends strongly on the micro-structure of the rock, in shear failure, rock can behave dilatant, compactant or no net change at all. The cutting regimes and the difference in required energy are also noted when comparing the amount of damage that is induced by the cutting process, as is shown in figure 6.37.

Based on the complete cutting tool, approximately half of the energy that is applied by the cutting tool is spent on friction in the scratching and brittle cutting regimes. When the edge chipping effect starts to dominate the cutting process, the cumulative energy spent on tool-grain friction will reduce to 30-35 % of the total energy spent in the cutting process. The highest intensity of the energy spent in the cutting process occurs at the tip of the tool (approximately 25 %). In figure 6.33 a saw-tooth cycle is clearly shown (it is also observed in the pore pressure near the tool tip, see figure 6.28). This corresponds with the stress build up, creating a crushed zone. The drops in the force correspond with the growing of macro-cracks. The occurrence of these cracks and the resulting chips is less clear in the image sequence in figure 6.27, most of the chips that occur are broken down into smaller pieces because these chips seem to get stuck between the tool and the still remaining rock body. The graph also shows a range where no angle was determined, in that range that area of the tool is not touching any rock, and thus no force is exerted. The sudden drop in the angle for the bottom of the tool tip is caused by the start of the edge chipping regime and in that range the front of the tool dominates the cutting process.

The friction factor of the tool-grain interactions gives a critical friction angle of 26.6°. This implies that for any angle of the cutting force in figure 6.34 larger than $90 - 26.6 = 63.4°$, the shear force at the tool surface is not large enough to generate slip with the given normal force. This occurs at the tip of the tool in the period of 0.4-0.6 sec. During this period, the interacting grains actually stick to the tool, causing the grains to roll along the surface of the tool. Note that the effect of rolling might be overestimated, because in the simulations perfect discs are used as particles and these have a lower rolling resistance compared to real grains. It could well be possible that due to the rolling effect, wear of the tool mainly occurs in the scratching regime.

As is shown in figure 6.29, the solid stresses near the tip of the tool can easily exceed 200 MPa. With these high stresses, the individual grains might fail themselves (which is not considered as a failure mechanism in the simulations). One needs to be careful with interpreting this phenomena, because this might as well be a scaling size effect of the simulation. In these simulations, particle diameters are in the range of 2-3 mm, while in real sedimentary rock (e.g. sandstone, limestone) the typical grain sizes are smaller than that. Complementary to that, smaller grains can withstand a higher stress before they will fail. For example, the critical nominal stress that sand particles can withstand scales $\sigma_{c,nom} \propto d_p^{-0.25}$ (Brzesowsky et al. (2011)).

The pore pressure build-up beneath the pick point in the range of 0-30 meter water depth does not differ significantly. A linear increasing trend can be noticed in the scratching regime, in the brittle chipping regime a saw tooth like behavior is observed. The peaks in pressure build up do not differ significantly with varying water depth. However, the total time averaged pore pressure below and in front of the tip of the tool are respectively 9.5% and 4.5% more at 30 meter water depth compared to the slightly submerged case (atmospheric pressure).

One needs to be careful when interpreting the results of these simulations. The results presented in this dissertation are based on a fully two-dimensional simulation, while in practice the rock cutting process is a fully three-dimensional problem. In 3D, chips are expected to show a different breakout pattern and shape compared to 2D. Besides that, the effect of friction of the rock along the cutting tool will be more realistic. That is, in 2D, the cut material cannot move in any other direction than along the movement of the tool (the 2D process can be compared with an infinite wide cutting tool), while in 3D the cut material may fall next to the equipment, which will significantly reduce the total force applied by the tool. In the near future, the simulation software will be extended into 3D to improve on those issues. Besides the estimation of friction along the tool, the force scaling effects in the brittle and pseudo-ductile regimes will be improved.

6.6. Conclusions

The tile cutting simulations show that if sufficient detail is applied, the DEM is capable of properly simulating the chip forming process. Furthermore, simulations of rock cutting processes like drilling and dredging show good resemblance with experiments. The effect of a hydrostatic pressure is properly included.

Simulations of rock cutting for both drilling and deep sea mining applications show that the cutting force increases with increasing hydrostatic pressure. This observation is similar to what is observed in experiments. The amount of damage applied to the rock increases as well and the size of the crushed zone increases. In drilling the chip balling and the presence of a filter cake are noted at high pressure. Furthermore, the trend of an increase of the cutting velocity on the cutting process for deep sea mining applications corresponds with the theory as well.

The results obtained with DEM-SP show better resemblance with the deep sea mining cutting experiments than the model described in Alvarez Grima et al. (2015). The results obtained in DEM-SP are based on the average cutting forces, as are the experimental results that they presented. However, the model that they present is based on peak forces and is compared with time averaged forces.

Research on equipment with cutting tools mounted on an axis not perpendicular to the rock surface, can be improved by simulating the cutting process based on a rotating cutter, instead of linear cutting. Obviously the assumption of a constant cutting depth is not valid in such experiments, but more assumptions do not hold as well, i.e. movement of the cutting tool is no longer parallel to the rock bed, a wear flat might induce a secondary cutting process and a stick-slip transition of the cut material along the tool is observed.

Recommendations

Although the 2D simulations show that the current methodology works well, significant improvements are expected when the method is extended towards 3D. Especially improvements on the effective width of the tool (breakout angle), increased resistance of the overburden to withhold the crushed zone and the flow of the cut material no longer has to move over the tool are expected.

All simulations show results based on a single cut in intact rock. After a tool has passed by, it still leaves some damaged rock behind. It will be interesting to see to what extend the specific energy will decrease due to the pre-damage that is applied by the previous tool.

The data that is (publicly) available to validate the rock cutting simulations is rather limited. The experiments that are available are often limited in the level of detail to properly model the macro-scopic mechanical properties of the rock, e.g. Kaitkay and Lei (2005).

Furthermore, the rock cutting simulations and the validation through experiments are all based on sharp tools. For industrial practice it would be more of interest to see how the rock cutting process is affected when wear of the tool is taken into consideration as well.

7

Conclusions and Recommendations

"If we knew what it was we were doing, it would not be called research, would it?"

Albert Einstein

In this chapter the overall conclusions and recommendations of this project are presented.

To recap, in the introduction, the aim of this study was defined as

- *To describe the physical phenomena that occur during the cutting of saturated rock, with an emphasis on the fluid pressure effects.*
- *To develop and implement a physical and mathematical model to predict the rock cutting process, in which the hydrostatic and pore pressure effects are incorporated.*

7.1. Conclusions

Based on a literature survey, it is found that this is the first time the DEM and SP are combined to model saturated rock. Mechanics of the solids (rock) is modeled with DEM, with elastic perfect brittle contact bond models for intact bonds and Coulomb friction model as collision model. Fluid is modeled as a pore pressure diffusion process and is solved with a smoothed particle method. The smoothed particle technique is also used to interpolate the discrete nature of DEM towards a continuum field. Coupling between the rock and fluid phase is achieved by calculating the volumetric strain of the rock, which acts as a source term in the pore pressure diffusion process. The resultant fluid pressure gradient is again applied as a particle force in DEM.

Mechanics of Saturated Rock

The presence of a pore fluid can have significant influence on the rock mechanics, through either

- Physico-chemical effects
- Drainage related effects

Within the scope of this thesis, only drainage related effects are considered. The most profound drainage related mechanisms are:

- Dilation hardening
- Compaction weakening

Both mechanisms can occur and the behavior depends on the local conditions. Furthermore, the effect of dilation hardening can be limited by either cavitation of the pore fluid or failure of the grains.

DEM-SP

The extension of DEM with the smoothed particle approach to model pore pressure effects works properly. Thus far, it is the first approach that allows for simulation of saturated rock. Simulated results match well with strain rate effects on saturated rock (shale).

The smoothed particle approach can be used to apply adaptive boundary conditions on a particle assembly, independently of the shape and orientation of the

boundary.

The effect of a high hydrostatic pressure is well captured in simulations of drilling experiments.

Both effects of cutting velocity and hydrostatic pressure are simulated properly. In the case of hyperbaric rock cutting experiments with positive rake angle, the DEM-SP shows better correspondence than the presented analytical models.

Rock Cutting Process

Rock cutting simulations for tile cutting, drilling, deep sea mining and dredging have been performed successfully. They show a good comparison with experiment data found in literature.

Simulations with DEM-SP of rock cutting with a positive rake angle show that with increasing hydrostatic pressure a transition occurs from tensile dominated towards shear dominated cutting. The transition seems to correlate with the tensile strength of the rock sample.

The size of the crushed zone, the total applied damage and the total required energy to cut the rock all increase with water depth.

The use of linear rock cutting models is a too strong simplification compared to the cutting motion of a tooth on a cutter head. Especially when tool wear is of interest.

Both the set of experiments cited in this dissertation as well as the simulated results of DEM-SP show that the use of the compressive strength of the rock only is insufficient to properly model the rock cutting process.

7.2. Recommendations

Mechanics of Saturated Rock

The rock cutting process covers the transition of an intact rock, through fragmentation towards a granular medium. In rock mechanics, and especially in the case of saturated rock, most of the research is concerned up to failure of the rock. More research is needed to cover the transition from intact rock towards a granular medium.

DEM-SP

Although the methodology works well for 2D cases, the rock cutting process in itself is a full 3D process, which cannot be fully captured in 2D (plain stress). Extension towards 3D should improve the simulated results.

The Smoothed Particle method can be used to interpolate DEM properties towards a continuum and solve a range of a continuum equations as well. This property should be used to model other physical processes that might be of interest on a continuum level, such as heat generation and dissipation (conduction), tool wear rate, etc.

The results of the DEM-SP depend on the particle assembly that is used. Thus far it is assumed that time averaging is sufficient to compare with experiments. Running similar simulations but with a new particle assembly might give different results. Similar to experiments, it will increase the confidence in the simulated results when multiple simulations are performed at the same settings with different particle assemblies.

In this thesis, the contact bond model and circular particles are used. Due to the simplicity of these models, the range of practical rocks that can be simulated is limited, especially with respect to high strength rock (> 100 MPa) and high ratios of compressive over tensile strength (> 8). Various methods could be used to extend the applicability of the DEM-SP for a wider range of mechanical rock properties. Several suggestions to improve the methodology are presented in chapter 4.

Rock Cutting Process

In the current model, the rock cutting process is considered as a 2D process. As a result, most of the debris generated moves over the tool surface, effectively mimicking an infinitely wide tool. In 3D, the debris can move sideways as well and thus the material cut does not have to move along the tool surface. Furthermore, it is expected that the accuracy of the vertical cutting force will increase as well. Other effects that cannot be properly simulated in 2D can be investigated as well, e.g. tool spacing, worn tools (wear flat).

Thus far, particle crushing is neglected in the simulations. Incorporating particle crushing can aid to improve the simulations where heterogeneities become significant, e.g. deep drilling, arctic clay (ice lenses).

The simulations that are described in this thesis all consider intact rock as a starting material, while in practice this will not be the case. Consecutive tool passages can give insight on interaction between multiple tools.

Thus far, the publicly available rock cutting tests as well as most of the rock cutting theories assume that the cutting motion is parallel to the rock surface and that the cutting velocity is constant. If the inertia and stiffness of the tool is low compared to the stiffness and strength of the rock, the load on the tool prescribes whether the tool can cut through the rock or not. Furthermore, experiments have been performed in which an oscillation is added to the cutting motion.

Further validation of the simulations is desired. Thus far the experimental data that is (publicly) available is rather limited. Especially concerning experiments on saturated rock. Special interest in new experiments would be on cutting velocity, non-constant cutting depth and hydrostatic pressure.

In the current implementation the rock cutting process is modeled as rigid body movement of the tool. Modeling the movement of the tool with oscillations in the velocity, or based on a prescribed load will allow to do research into e.g. cutting in tougher rock, percussive drilling.

Practical Implications

In this dissertation it is shown that the cutting of saturated rock can be significantly influenced by the cutting velocity and the hydrostatic pressure. Based on results obtained from both literature and this research, several key aspects for rock cutting in the industrial practice are noted. These aspects mostly concern the design and operation of the excavation equipment.

The equipment should be designed in such a way that it can easily deliver the required normal force with respect to the designed cutting depth. If the equipment cannot deliver the desired normal force, the tool will not penetrate deep enough. The loss of penetration depth can also result in a loss of interaction between consecutive teeth, leading to a dramatic loss in excavation rate. Design parameters like cutting velocity and tool spacing can help to extend the applicability of the equipment.

Both compressive and tensile strength are required to estimate dominant failure mode of the cutting process.

It is shown that for lower cutting velocities, the cutting force is lower as well. This is caused by a reduction of the pressure drop when dilation occurs in the cutting process. It might be possible to take advantage of this phenomenon by lowering the viscosity of the fluid, e.g. using a drilling fluid with lower viscosity can be beneficial for the drilling process.

A

Practical Rock Properties

For basically all industrial applications of cutting of saturated rock, the information that the engineers have at hand to design and estimate the production, cutting forces, etc. is limited. Most often only the type of rock (sandstone, limestone, etc.) and the UCS value of the rock are given. Furthermore, on a larger scale some information about the RQD of the rock may be available. Here the rules of thumb that are used in this thesis to estimate the rock properties when these are not provided in the cited publication. These are the classification of rocks based on their compressive strength, as in table A.1. Typical values for Young's modulus, Poisson's ratio and the strength ratio m are respectively given in tables A.2, A.3 and A.4.

Table A.1: Classification of rocks on the basis of UCS, after Attewell and Farmer (1976).

Strength classification	Strength range [MPa]	Typical rock types
Very weak	10-20	Weathered and weakly compacted sedimentary rocks
Weak	20-40	Weakly cemented sedimentary rocks
Medium	40-80	Competent sedimentary rocks, coarse igneous rocks
Strong	80-160	Fine-grained sandstones, competent igneous rocks
Very strong	160-320	Quartzites, fine-grained igneous rocks

Table A.2: Typical values of Young's modulus of intact rocks, based on Officials and Transportation (1989), in (Zhang et al., 2005)

Rock type	No of samples	Max	Minimum	Mean	Std
Granite	26	100	6.41	52.7	24.5
Marble	14	73.8	4.00	42.6	17.2
Sandstone	27	39.2	0.62	14.7	8.21
Shale	30	38.6	0.007	9.79	10.0
Limestone	30	89.6	4.48	39.3	25.7

Table A.3: Typical values of Poisson's ratio of intact rocks, based on Officials and Transportation (1989), in (Zhang et al., 2005)

Rock type	No of samples	Max	Minimum	Mean	Std
Granite	22	0.39	0.09	0.20	0.08
Marble	5	0.40	0.17	0.28	0.08
Sandstone	12	0.46	0.08	0.20	0.11
Shale	3	0.18	0.03	0.09	0.06
Limestone	19	0.33	0.12	0.23	0.06

Table A.4: Typical values of strength ratio m for different rocks, based on Hoek and Brown (1997), in (Zhang et al., 2005)

Rock type	Texture	Mean [MPa]	Std [MPa]
Granite	Coarse	32	3
Marble	Coarse	9	3
Sandstone	Medium	17	4
Shale	Very fine	6	2
Limestone	Coarse	12	3
Limestone	Medium	10	2
Limestone	Fine	9	2

Bibliography

Adachi, J., Detournay, E., and Drescher, A. (1996). Determination of rock strength parameters from cutting tests. In *Proceedings of the 2nd North American Rock Mechanics Symposium (NARMS 1996)*, Rotterdam, the Netherlands.

Alvarez Grima, M., Heeren, J., Verichev, S. N., and Wijk, J. M. V. (2011). Into the deep: a risk based approach for research to deepsea mining. In *CEDA Dredging Days 2011*, Rotterdam,the Netherlands.

Alvarez Grima, M., Miedema, S., van de Ketterij, R., Yenigül, N., and van Rhee, C. (2015). Effect of high hyperbaric pressure on rock cutting process. *Engineering Geology*, 196:24–36.

Andersen, E. and Azar, J. (1993). PDC-Bit performance under simulated borehole conditions. In *SPE Drilling and Completion*, number September, pages 184–188.

Atkinson, B. K. (1984). Subcritical crack growth in geological materials. *Journal of Geophysical Research*, 89(B6):4077.

Attewell, P. and Farmer, I. (1976). *Principles of engineering geology*. Chapman and Hall, London, UK.

Bagi, K. (2005). An algorithm to generate random dense arrangements for discrete element simulations of granular assemblies. *Granular Matter*, 7(1):31–43.

Benabbou, a., Borouchaki, H., Laug, P., and Lu, J. (2009). Geometrical modeling of granular structures in two and three dimensions. Application to nanostructures. *International Journal for Numerical Methods in Engineering*, 80(4):425–454.

Bernabe, Y. (1987). The effective pressure law for permeability during pore pressure and confining pressure cycling of several crystalline rocks. *Journal of Geophysical Research*, 92(B1):649–657.

Bilgin, N. (1977). *Investigations into the mechanical cutting characteristics of some medium and high strength rocks*. Phd thesis, University of Newcastle upon Tyne.

Black, A. D., Bland, R. G., Hughes, B., Curry, D. A., Iii, L. W. L., Christensen, H., Robertson, H. A., Judzis, A., Prasad, U., and Grant, T. (2008). Optimization of deep drilling performance with improvements in drill bit and drilling fluid design. In *2008 IADC/SPE Drilling Conference*, page 112731.

Brace, W. and Martin III, R. (1968). A test of the law of effective stress for crystalline rocks of low porosity. *International Journal of Rock Mechanics and Mining Sciences*, 5:415–426.

Brady, B. and Brown, E. (2005). *Rock mechanics for underground mining*. Springer Science Business Media, Inc, Dordrecht.

Brzesowsky, R. H., Spiers, C. J., Peach, C. J., and Hangx, S. J. T. (2011). Failure behavior of single sand grains: Theory versus experiment. *Journal of Geophysical Research*, 116(B6):B06205.

Buchi, E. (1984). *Einfluss geologischer parameter auf die Vortriebsleistung einer Tunnelbohrmachine. (Influence of geolocial parameters on the performance of a tunnel boring machine*. Doctoral, University of Bern, Switzerland.

Byerlee, J. (1978). Friction of rocks. *Pure and Applied Geophysics*, 116(4).

Carmona, H., Wittel, F., Kun, F., and Herrmann, H. (2008). Fragmentation Processes in Impact of Spheres. *Physical Review E*, 77:051302.

Carrapatoso, C., Inoue, N., and Curry, D. (2014). New Developments for Single-Cutter Modeling of Evaporites using Discrete Element Method. In *Rock mechanics for Natural Resources and Infrastructure*.

Chaput, E. (1991). Observations and analysis of hard rocks cutting failure mechanisms using PDC cutters. Technical report, Imperial College of Science, Technology and Medicine, London, UK.

Chen, J., Beraun, J., and Carney, T. (1999). A corrective smoothed particle method for boundary value problems in heat conduction. *International Journal for Numerical Methods in Engineering*, 252(June 1998):231–252.

Chiaia, B. (2001). Fracture mechanisms induced in a brittle material by a hard cutting indenter. *International Journal of Solids and Structures*, 38(44-45):7747–7768.

Cho, J. W., Jeon, S., Yu, S. H., and Chang, S. H. (2010). Optimum spacing of TBM disc cutters: A numerical simulation using the three-dimensional dynamic fracturing method. *Tunnelling and Underground Space Technology*, 25(3):230–244.

Cho, N., Martin, C., and Sego, D. (2007). A clumped particle model for rock. *International Journal of Rock Mechanics and Mining Sciences*, 44(7):997–1010.

Chung, J. S. (1996). Deep-ocean mining: Technologies for manganese nodules and crusts. *International Journal of Offshore and Polar Engineering*, 6(4).

Cleary, P. and Monaghan, J. (1999). Conduction modelling using smoothed particle hydrodynamics. *Journal of Computational Physics*, 148(1):227–264.

Cleary, P., Sinnott, M., and Morrison, R. (2006). Prediction of slurry transport in SAG mills using SPH fluid flow in a dynamic DEM based porous media. *Minerals Engineering*, 19(15):1517–1527.

Colagrossi, A. and Landrini, M. (2003). Numerical simulation of interfacial flows by smoothed particle hydrodynamics. *Journal of Computational Physics*, 191(2):448–475.

Colback, P. and Wild, B. (1965). The influence of moisture content on the compressive strength of rock. In *Proceedings of the 3rd Canadian Rock Mechanics Symposium*, pages 65–83.

Combinatie Speurwerk Baggertechniek (1984). Het snijden van gesteente.

Cook, J. (1999). The effects of pore pressure on the mechanical and physical properties of shales. *Oil & Gas Science and Technology*, 54(6):695–701.

Cook, J. M., Sheppard, M. C., Houwen, O. H., and Forex, S. (1991). Effects of strain rate and confining pressure on the deformation and failure of shale. In *SPE Drilling Engineering*, number June, pages 100–104.

Cools, P. (1984). Determination of the changes in saturation of a porous rock sample when varying the porewater pressure. Technical report, Delft.

Cools, P. (1993). Temperature measurements upon the chisel surface during rock cutting. *International Journal of Rock Mechanics and Mining Sciences and*, 30(1):25–35.

Coussy, O. (2004). *Poromechanics*. John Wiley & Sons Ltd, West Sussex.

Cundall, P. and Strack, O. (1979). A discrete numerical method for granular assemblies. *International Journal for Rock Mechanics, Mining Sciences and Geomechanics Abstracts*, 29:47–65.

Cunningham, R. A. and Eenink, J. G. (1959). Laboratory study of effect of overburden , formation and mud column pressures on drilling rate of permeable formations. In *33rd Annual Fall Meeting of Society of Petroleum Engineers*, volume 217, pages SPE 1094–G, Houston, Texas, USA.

Dagrain, F. and Richard, T. (2006). On the influence of PDC wear and rock type on friction coefficient and cutting efficiency. *Eurock 2006: Multiphysics Coupling and Long Term Behaviour in Rock Mechanics*, (MAY 2006):577–584.

de Wit, L. (2015). *3D CFD modelling of overflow dredging plumes*. Phd thesis, Delft University of Technology.

Deketh, H. J. R. (1995). *Wear of rock cutting tools. Laboratory experiments on the abrasivity of rock*. Phd thesis, Delft University of Technology.

Detournay, E. and Atkinson, C. (2000). Influence of pore pressure on the drilling response in low-permeability shear-dilatant rocks. *International Journal of Rock Mechanics and Mining Sciences*, 37(7):1091–1101.

Detournay, E. and Defourny, P. (1992). A Phenomenological Model for the Drilling Action of Drag Bits. *International Journal of Rock Mechanics and Mining Sciences*, 29(I):13–23.

Detournay, E. and Tan, C. (2002). Dependence of drilling specific energy on bottomhole pressure in shales. In *SPE/ISRM Rock Mechanics Conference*, number 2, pages 1–10, Irving, Texas, USA.

Duda, M. and Renner, J. (2013). The weakening effect of water on the brittle failure strength of sandstone. *Geophysical Journal International*, 192(3):1091–1108.

Dyke, C. G. and Dobereiner, L. (1991). Evaluating the strength and deformability of sandstones. *Quarterly Journal of Engineering Geology and Hydrogeology*, 24(1):123–134.

Edelsbrunner, H. and Mücke, E. (1994). Three-dimensional alpha shapes. *ACM Trans Graph*, 13(1):43–72.

Edmond, J. and Paterson, M. (1972). Volume changes during the deformation of rocks at high pressures. *International Journal of Rock Mechanics and Mining Sciences & Geomechanics Abstracts*, 9(2):161–182.

Eggleston, D., Herzog, R., and Thomsen, E. (1959). Observations on the angle relationships in metal cutting. *ASME Journal of Engineering for Industry*, 81:263–279.

Egholm, D. L. (2007). A new strategy for discrete element numerical models: 1. Theory. *Journal of Geophysical Research*, 112(B5):1–16.

Egholm, D. L., Sandiford, M., Clausen, O. R., and Nielsen, S. B. (2007). A new strategy for discrete element numerical models: 2. Sandbox applications. *Journal of Geophysical Research*, 112:B05204: 1–12.

EU Commission (2015). Report on critical raw materials for the EU. Technical Report Retrieved April, 30.

Evans, I. (1965). The force required to cut coal with blunt wedges. *International Journal of Rock Mechanics and Mining Sciences & Geomechanics Abstracts*, 2(1):1–12.

Evans, I. (1972). Line spacing of picks for effective cutting. *International Journal of Rock Mechanics and Mining Sciences and*, 9(3):355–361.

Evans, I. (1984). A theory of the cutting force for point-attack picks. *International Journal of Mining Engineering*, 2(1):63–71.

Fakhimi, A. and Lanari, M. (2014). DEM–SPH simulation of rock blasting. *Computers and Geotechnics*, 55:158–164.

Fakhimi, a. and Villegas, T. (2007). Application of Dimensional Analysis in Calibration of a Discrete Element Model for Rock Deformation and Fracture. *Rock Mechanics and Rock Engineering*, 40(2):193–211.

Farmer, I. (1983). *Engineering Behaviour of Rocks*. Chapman and Hall, 2nd edition.

Fatehi, R., Fayazbakhsh, M. A., and Manzari, M. T. (2009). On discretization of second-order derivatives in smoothed particle hydrodynamics. *International Journal of Aerospace and Mechanical Engineering*, 3(1):41–44.

Feenstra, R. (1988). Status of polycrystalline-diamond- compact bits: part 1-development. *Journal of Petroleum Technology*, 40(06):675–684.

Feenstra, R. and van Leeuwen, J. (1964). Full-scale experiments on jets in impermeable rock drilling. *Journal of Petroleum Technology*, 16(3):329–336.

Feng, Y. T., Han, K., and Owen, D. R. J. (2003). Filling domains with disks: an advancing front approach. *International Journal for Numerical Methods in Engineering*, 56(5):699–713.

Francois, D. and Wilshaw, T. (1964). The effect of hydrostatic pressure on the cleavage fracture of polycrystalline materials. *Journal of Applied Physics*, 39:4170–4177.

Gangi, A. F. (1978). Variation of whole and fractured porous rock permeability with confining pressure. *International Journal of Rock Mechanics and Mining Sciences and*, 15(5):249–257.

Garnier, A. and van Lingen, N. (1958). Phenomena affecting drilling rates at depth. In *33rd Annual Fall Meeting of Society of Petroleum Engineers*, pages 232–239.

Gehring, K. (1987). Rock testing procedures at VA's geotechnical laboratory in Zeltweg. Technical report, Voest Alpine Zeltweg, Austria.

Goktan, R. (1997). A suggested improvement on Evans' cutting theory for conical bits. In *Proc. of the 4th Int. Symp. on mine mechanization and automation*, pages A4–57/A4–61, Brisbane, Queensland, Australia.

Goktan, R. M. and Gunes, N. (2005). A semi-empirical approach to cutting force prediction for point-attack picks. *Journal of the South African Institute of Mining and Metallurgy*, 105(April):257–264.

Gowd, T. and Rummel, F. (1980). Effect of Confining Pressure on the Fracture Behaviour of a Porous. *International Journal of Rock Mechanics and Mining Sciences*, 17:225–229.

Gray-Stephens, D., Cook, J., and Sheppard, M. (1994). Influence of pore pressure on drilling response in hard shales. In *SPE Drilling & Completion*, number December, page SPE 23414.

Griffith, A. (1921). The phenomena of rupture and flow in solids. *Philosophical Transactions of the Royal Society of London. Series A, Containing Papers of a Mathematical or Physical Character*, 221:163–198.

Guo, Y. and Curtis, J. S. (2015). Discrete element method simulations for complex granular flows. *Annu. Rev. Fluid Mech*, 47:21–46.

Hatamura, Y. and Chijiiwa, K. (1975). Analysis of the mechanism of soil cutting (1st report cutting patterns of soils). *Bulletin of the JSME*, 18(120):619–626.

He, J. and Vlasblom, W. (1998). Modelling of saturated sand cutting with large rake angles. In *WODCON XV*, Las Vegas, USA. WODA.

He, X. and Xu, C. (2015). Discrete element modelling of rock cutting: from ductile to brittle transition. *International Journal for Numerical and Analytical Methods in Geomechanics*, pages n/a–n/a.

Helmons, R. and Miedema, S. (2013). Cutting through hard rock-like materials, a review of the process. In *WODCON XX: The art of dredging*, Brussels, Belgium.

Helmons, R., Miedema, S., Alvarez Grima, M., and van Rhee, C. (2016a). Modeling fluid pressure effects in cutting of saturated rock. *Engineering Geology*.

Helmons, R., Miedema, S., and Rhee, C. V. (2016b). Simulating hydro mechanical effects in rock deformation by combination of the discrete element method and the smoothed particle method. *International Journal of Rock Mechanics and Mining Sciences*, 86:224–234.

Helmons, R., Miedema, S., and van Rhee, C. (2015). Inclusion of pore pressure effects in discrete element modeling of rock cutting. In *IV International Conference on Particle-based Methods - Fundamentals and Applications, PARTICLES 2015*, pages 1–12.

Helmons, R., Miedema, S., and van Rhee, C. (2016c). Discrete element modeling of circular rock cutting with evaluation of pore pressure effects. In *WODCON XXI: Innovations in dredging*, Miami, Florida, USA.

Hemami, B. and Fakhimi, A. (2014). Numerical simulation of rock-loading machine interaction. In *48th US Rock Mechanics/Geomechanics Symposium*.

Hettiaratchi, D. and Reece, A. (1967). Symmetrical three-dimensional soil failure. *Journal of Terramechanics*, 4(3):45–67.

Hoek, E. and Brown, E. (1980). *Underground excavation in rock*. Institution of Mining and Metallurgy, London, UK.

Hoek, E. and Brown, E. T. (1997). Practical estimates of rock mass strength. *International Journal of Rock Mechanics and Mining Sciences*, 34(8):1165–1186.

Hoover, W. G., Pierce, T. G., Hoover, C. G., Shugart, J. O., Stein, C. M., and Edwards, a. L. (1994). Molecular-dynamics, smoothed-particle applied mechanics, and irreversibility. 28(19):155–174.

Huang, H. (1999). *Discrete element modeling of tool-rock interaction*. Phd thesis, University of Minnesota.

Huang, H. and Detournay, E. (2013). Discrete element modeling of tool-rock interaction II : rock indentation. *International Journal for Numerical and Analytical Methods in Geomechanics*, 37(13):1930–1947.

Huang, H., Lecampion, B., and Detournay, E. (2013). Discrete element modeling of tool-rock interaction I : rock cutting. *International Journal for Numerical and Analytical Methods in Geomechanics*, 37(13):1913–1929.

Hurt, K. (1980). Rock cutting experiments with point attack tools. *Colliery Guardian Coal Int*, 228:47–50.

Hurt, K. and MacAndrew, K. (1985). Cutting efficiency and life of rock cutting picks. *Min. Sci. Tech.*, 2:139–151.

Judzis, A., Bland, R. G., Curry, D. A., Black, A. D., Robertson, H. A., Meiners, M. J., and Grant, T. C. (2009). Optimization of deep-drilling performance — benchmark testing drives ROP improvements for bits and drilling fluids. In *SPE/IADC Drilling Conference 2007*, volume 2008, page SPE 105885, Amsterdam, the Netherlands.

Kaitkay, P. and Lei, S. (2005). Experimental study of rock cutting under external hydrostatic pressure. *Journal of Materials Processing Technology*, 159(2):206–213.

Kenney, P. and Johnson, S. (1976). The effect of wear on then performance of mineral cutting tools. *Colliery Guardian*, 224:246–252.

Kolle, J. (1996). The effects of pressure and rotary speed on the drag bit drilling strength of deep formations. In *SPE Annual Technical Conference and Exhibition*, page SPE 36434, Denver, Colorado, USA.

Komoróczi, A., Abe, S., and Urai, J. L. (2013). Meshless numerical modeling of brittle–viscous deformation: first results on boudinage and hydrofracturing using a coupling of discrete element method (DEM) and smoothed particle hydrodynamics (SPH). *Computational Geosciences*, 17(2):373–390.

Kuhne, I. (1952). Die Wirkungsweise von Rotarymeiseln und anderen drehenden Gesteinsbohren. *Sonderdruck aus der Zeitschrift, Bohrtechnik-Brunnenbau*, pages 1–5.

Lashkaripour, G. R. and Ghafoori, M. (2002). The engineering geology of the Tabarak Abad Dam. *Engineering Geology*, 66(3-4):233–239.

Lawn, B. (1993). *Fracture of Brittle Solids*. Cambridge university press.

Ledgerwood III, L. W. (2007). PFC modeling of rock cutting under high pressure conditions. In *1st Canada -U.S. Rock Mechanics Symposium*, volume 2, pages ARMA–07–063, Vancouver, Canada.

Lei, S. and Kaitkay, P. (2003). Distinct element modeling of rock cutting under hydrostatic pressure. *Key Engineering Materials*, 250:110–117.

Li, H., Li, J., Liu, B., Li, J., Li, S., and Xia, X. (2013). Direct tension test for rock material under different strain rates at quasi-static loads. *Rock Mechanics and Rock Engineering*, 46(5):1247–1254.

Li, X., Li, H., Liu, Y., Zhou, Q., and Xia, X. (2016). Numerical simulation of rock fragmentation mechanisms subject to wedge penetration for TBMs. *Tunnelling and Underground Space Technology*, 53:96–108.

Liefferink, D. (2013). *Failure mechanism of cutting submerged frozen clay in an arctic rrenching process*. Master thesis, Delft University of Technology.

Liu, H. Y., Kou, S. Q., and Lindqvist, P.-A. (2002). Numerical simulation of the fracture process in cutting heterogeneous brittle material. *International Journal for Numerical and Analytical Methods in Geomechanics*, 26(13):1253–1278.

Liu, J., Cao, P., and Han, D. (2015). Sequential indentation tests to investigate the influence of confining stress on rock breakage by tunnel boring machine cutter in a biaxial state. *Rock Mechanics and Rock Engineering*, 49(4):1479–1495.

Lohner, R., Baqui, M., Haug, E., and Muhamad, B. (2016). Real-time micro modelling of a million pedestrians. *Engineering Computations*, 33(1):217–237.

Louis, C., Dessenne, J.-L., and Feuga, B. (1977). Interaction between water flow phenomena and the mechanical behavior of soil or rock masses. In Gudehus, G., editor, *Finite Elements in Geomechanics*, pages 479–511. Wiley, New York.

Lucy, L. (1977). A numerical approach to the testing of the fission hypothesis. *Astronomical Journal*, 82:1013–1024.

Luding, S. (2008). Cohesive Frictional Powders: Contact Models for Tension. *Granular Matter*, 10:235–246.

Luding, S. (2011). From discrete particles to solids - about sintering and self-healing (review). *Computer Methods in Material Science*, 11:53–63.

Luger, H. (1981). Invloed van wateroverspanning en vervormingssnelheid bij indringproeven op St. Leu (in Dutch). Technical report, Delft Soil Mechanics Laboratory.

Mahabadi, O. K., Lisjak, A., Grasselli, G., Lukas, T., and Munjiza, A. (2004). Numerical modelling of a triaxial test of homogeneous rocks using the combined finite-discrete element method.

Majidi, R., Miska, S., and Tammineni, S. (2011). PDC single cutter: the effects of depth of cut and rpm under simulated borehole conditions. *Wiertnictwo Nafta Gaz*, 28(1-2):283–295.

Martin III, R. (1980). Pore pressure stabilization of failure in westerly granite. *Geophysical Research Letters*, 7(5):404–406.

Masuda, K., Mizutani, H., and Yamada, I. (1987). Experimental study of strain-rate dependence and pressure dependence of failure properties of granite. *J. Phys. Earth*, 35:37–66.

Medhurst, T. and Brown, E. (1996). Large scale laboratory testing of coal. In *Proc. 7th Australian-New Zeland Conf. on Geomech.*, pages 203–208, Canberra, Australia.

Meijer, K. (1972). Eerste serie rotssnijproeven op tegels (in Dutch). Technical report, Delft Hydraulics, Delft, Netherlands.

Meijer, K. (1973a). Brokvorm bij tweedimensionaal snijden (in Dutch). Technical report, Delft Hydraulics, Delft, Netherlands.

Meijer, K. (1973b). Het snijden van rots: tweede serie rotssnijproeven op tegels (in Dutch). Technical report, Delft Hydraulics, Delft, Netherlands.

Mendoza Rizo, J. (2013). *Considerations for discrete element modeling of rock cutting*. Phd thesis, University of Pittsburgh.

Merchant, M. (1945). Mechanics of the metal cutting process. II. plasticity conditions in orthogonal cutting. *Journal of Applied Physics*, 16(6):318.

Miedema, S. (1987). *Calcuation of the cutting forces when cutting water saturated sand*. Phd thesis, Delft University of Technology.

Miedema, S. (2014). *The Delft sand, clay and rock cutting model*. IOS Press, Delft, Netherlands.

Miedema, S. and Frijters, D. (2003). The mechanism of kinematic wedges at large cutting angles - velocity and friction measurements. In *23rd WEDA Technical Conference & 35th TAMU Dredging Seminar*.

Miedema, S. and Zijsling, D. (2012). Hyperbaric rock cutting. In *OMAE 2012: 31st International Conference on Ocean, Offshore and Arctic Engineering*, Rio de Janeiro, Brazil.

Mishnaevsky Jr, L. (1995). Physical mechanisms of hard rock fragmentation under mechanical loading : a review. *International Journal of Rock Mechanics and Mining Sciences*, 32(8):763–766.

Monaghan, J. (1994). Simulating free surface flows with SPH. *Journal of Computational Physics*, 110:399–406.

Monaghan, J. (2012). Smoothed particle hydrodynamics and its diverse applications. *Annual Review of Fluid Mechanics*, 44(1):323–346.

Moon, T. and Oh, J. (2011). A study of optimal rock-cutting conditions for hard rock TBM using the discrete element method. *Rock Mechanics and Rock Engineering*, pages 837–849.

Morrow, C., Moore, D., and Lockner, D. (2000). The effect of mineral bond strength and adsorbed water on fault gouge frictional strength. *Geophysical Research Letters*, 27(6):815–818.

Motzheim, R. (2016). *Vibration-impact cutting of submerged forzen clay in arctic trenching process*. Master thesis, Delft University of Technology.

Muhammad, N., Rogers, B., and Li, L. (2013). Understanding the behaviour of pulsed laser dry and wet micromachining processes by multi-phase smoothed particle hydrodynamics (SPH) modelling. *Journal of Physics D: Applied Physics*, 46(9):095101.

Muirhead, I. and Glossop, L. (1968). Hard rock tunnelling machines. *Trans. Inst. Min. Metall. Sect A*, 77:1–21.

Natau, O., Mutschler, T., and Lempp, C. (1991). Estimation of the cutting rate and the bit wear of partial-face tunnelling machines. In *7th ISRM Congress*, page 289, Aachen, Germany.

Nishimatsu, Y. (1972). The mechanics of rock cutting. *International Journal of Rock Mechanics and Mining Sciences*, 9:261–270.

Nur, A. and Byerlee, J. (1971). An exact effective stress law for elastic deformation of rocks with fluids. *Journal of Geophysical Research*, 76(26):6414–6419.

Oñate, E. and Rojek, J. (2004). Combination of discrete element and finite element methods for dynamic analysis of geomechanics problems. *Computer Methods in Applied Mechanics and Engineering*, 193(27-29):3087–3128.

Obreimoff, J. W. (1930). The splitting strength of mica. *Proceedings of the Royal Society of London. Series A, Containing Papers of a Mathematical and Physical Character*, 127(805):290–297.

O'Dogherty, M. and Burney, A. (1963). A laboratory study of the effect of cutting speed on the performance of two coal cutter picks. *Colliery Eng. (London)*, 40:51–54.

Officials, A. A. o. S. H. and Transportation (1989). *Standard specifications for highway bridges*. Washington DC, USA, 14th editi edition.

Onodera, T. and Kamura, A. (1980). Relation between texture and mechanical properties of crystalline rocks. *Bulletin International Association Engineering Geology*, 22:173–177.

Ortega, A. (2014). Towards zero impact of deep sea offshore projects. Technical report.

Paterson, M. and Wong, T.-f. (2005). *Experimental Rock Deformation - The Brittle Field*. Springer Berlin Heidelberg, 2nd edition.

Pittino, G., Galler, R., Mikl-resch, M., Tichy, R., Ecker, W., Gimpel, M., and Kargl, H. (2015). The rock cutting process of road headers – Overview of laboratory tests and numerical simulation. In *ISRM Regional Symposium EUROCK 2015 - Future Development of Rock Mechanics*, pages 243–248.

Pomeroy, C. (1963). The breakage of coal by wedge action. *Colliery Guardian1*, 207(5354):672–677.

Population Division of the Department of Economic and Social Affairs of the United Nations Secretariat (2015). World population prospects: the 2015 revision. Technical report, New York.

Potapov, A. V., Hunt, M. L., and Campbell, C. S. (2001). Liquid-solid flows using smoothed particle hydrodynamics and the discrete element method. *Powder Technology*, 116(2-3):204–213.

Potts, E. and Shuttleworth, P. (1958). A study on the ploughability of coal, with special reference to the effects of blade shape, direction of planing to the cleat, planing speed and the influence of water infusion. *Trans. Inst. Min. Eng.*, 117:519–553.

Potyondy, D. O. (2015). The bonded-particle model as a tool for rock mechanics research and application: current trends and future directions. *Geosystem Engineering*, 18(1):1–28.

Potyondy, D. O. and Cundall, P. a. (2004). A bonded-particle model for rock. *International Journal of Rock Mechanics and Mining Sciences*, 41(8 SPEC.ISS.):1329–1364.

Ranman, K. (1985). A model describing rock cutting with conical picks. *Rock Mechanics and Rock Engineering*, 18(2):131–140.

Reviron, N., Reuschlé, T., and Bernard, J.-D. (2009). The brittle deformation regime of water-saturated siliceous sandstones. *Geophysical Journal International*, 178(3):1766–1778.

Rice, J. R. and Cleary, M. P. (1976). Some basic stress diffusion solutions for fluid saturated elastic porous media with compressible constituents. *Reviews of Geophysics and Space Physics*, 14(2):227–241.

Richard, T., Dagrain, F., Poyol, E., and Detournay, E. (2012). Rock strength determination from scratch tests. *Engineering Geology*, 147-148:91–100.

Richard, T., Detournay, E., Drescher, A., Nicodeme, P., and Fourmaintraux, D. (1998). The scratch test as a means to measure strength of sedimentary rocks. In *SPE/ISRM Eurock '98*, Trondheim, Norway.

Robinson, M., Ramaioli, M., and Luding, S. (2014). Fluid-particle flow simulations using two-way-coupled mesoscale SPH-DEM and validation. *International journal of multiphase flow*, 59:121–134.

Rojek, J. (2014). Discrete element thermomechanical modelling of rock cutting with valuation of tool wear. *Computational Particle Mechanics*, 1(1):71–84.

Rojek, J., Nosewicz, S., Mazdziarz, M., Kowalczyk, P., Wawrzyk, K., and Lumelskyj, D. (2017). Modeling of a Sintering Process at Various Scales. *Procedia Engineering*, 177:263–270.

Rojek, J., Oñate, E., Labra, C., and Kargl, H. (2011). Discrete element simulation of rock cutting. *International Journal of Rock Mechanics and Mining Sciences*, 48(6):996–1010.

Rostami, J. and Ozdemir, L. (1993). A new model for performance prediction of hard rock TBMs. In *Proceedings of the Rapid Excavation and Tunneling Conference*. Society for mining, metallogy and exploration inc.

Roxborough, F. (1973). Cutting rock with picks. *Trans. Inst. Min. Eng.*, 132:445–454.

Roxborough, F. and Phillips, H. (1975). Rock excavation by disc cutter. *International Journal of Rock Mechanics and Mining Sciences*, 12:361–366.

Roxborough, F. and Sen, G. (1986). Breaking coal and rock. In Martin, C., editor, *Australian coal mining practice*, pages 130–147. Aimm monog edition.

Rudnicki, J. W. and Chen, C.-H. (1988). Stabilization of rapid frictional slip on a weakening fault by dilatant hardening. *Journal of Geophysical Research*, 93(B5):4745.

Rutter, E. (1972). The effects of strain-rate changes on the strength and ductility of Solenhofen limestone at low temperatures and confining pressures. *International Journal of Rock Mechanics and Mining Sciences & Geomechanics Abstracts*, 9(2):183–189.

Scholtès, L. and Donzé, F.-V. (2013). A DEM model for soft and hard rocks: Role of grain interlocking on strength. *Journal of the Mechanics and Physics of Solids*, 61(2):352–369.

Schön, J. (1996). *Physical properties of rocks - fundamentals and principles of petrophysics*. Pergamon, Oxford, UK.

Shimizu, H., Murata, S., and Ishida, T. (2011). The distinct element analysis for hydraulic fracturing in hard rock considering fluid viscosity and particle size distribution. *International Journal of Rock Mechanics and Mining Sciences*, 48(5):712–727.

Singh, A. and Luding, S. (2010). Flow behavior at different shear rates for dry powders. In *Proceedings of World Congress on Particle Technology WCPT6*. Nürnberg Messe GmbH.

Skempton, A. (1960). Effective stress in soils, concrete and rocks. In *Pore pressure and suction in soils*, pages 4–16.

Snowdon, R. a., Ryley, M. D., and Temporal, J. (1982). A study of disc cutting in selected British rocks. *International Journal of Rock Mechanics and Mining Sciences and*, 19(3):107–121.

Stahl, M. and Konietzky, H. (2010). Discrete element simulation of ballast and gravel under special consideration of grain-shape, grain-size and relative density. *Granular Matter*, 13(4):417–428.

Su, O. and Akcin, N. A. (2011). Numerical simulation of rock cutting using the discrete element method. *International Journal of Rock Mechanics and Mining Sciences*, 48(3):434–442.

Sun, X., Sakai, M., and Yamada, Y. (2013). Three-dimensional simulation of a solid-liquid flow by the DEM-SPH method. *Journal of Computational Physics*, 248:147–176.

Swan, G., Cook, J., Bruce, S., and Meehan, R. (1989). Strain rate effects in Kimmeridge bay shale. *International Journal of Rock Mechanics and Mining Sciences & Geomechanics Abstracts*, 26(2):135–149.

Swolfs, H. (1972). Chemical effects of pore fluids on rock properties. In *Underground Waste Management and Evironmental Implications*, chapter 18, pages 224–234.

Terzaghi, K. (1943). *Theoretical Soil Mechanics*. John Wiley & Sons Ltd.

Thomas, P. and Bray, J. (1999). Capturing nonspherical shape of granular media with disk clusters. *Journal of Geotechnical and Geoenvironmental Engineering*, 1235(3):169–178.

Tiller, F. (1953). *Chem. Engrg. Prog*, 49:467.

Tropin, N., Manakov, V., and Bocharov, O. (2014). Implementation of boundary conditions in discrete element modeling of rock cutting under pressure. *Applied Mechanics and Materials*, 598:114–118.

Uittenbogaard, R. (1980). Indringproeven op WL-II met grote indringdiepte: Meetverslag en analyse (in Dutch). Technical report, Delft Hydraulics Laboratory.

van Grunsven, F., Keetels, G., and van Rhee, C. (2016). Modeling offshore mining turbidity sources. In *WODCON XXI: Innovations in dredging*, Miami, Florida, USA.

van Kesteren, W. (1995). Numerical simulations of crack bifurcation in the chip forming cutting process in rock. *Fracture of Brittle Disordered Materials: concrete, Rock and Ceramics*, pages 505–524.

van Opstal, T. (2015). cutter head for removing material from a water bed patent IHC Holland.pdf.

van Wijk, J. (2016). *Vertical hydraulic transport for deep sea mining.* Phd thesis, Delft University of Technology.

van Wyk, G., Els, D., Akdogan, G., Bradshaw, S., and Sacks, N. (2014). Discrete element simulation of tribological interactions in rock cutting. *International Journal of Rock Mechanics and Mining Sciences*, 65:8–19.

Vasarhelyi, B. (2003). Some observations regarding the strength and deformability of sandstones in dry and saturated conditions. *Bulletin of Engineering Geology and the Environment*, 62(3):245–249.

Vasarhelyi, B. (2005). Statistical analysis of the influence of water content on the strength of the miocene limestone. *Rock Mechanics and Rock Engineering*, 38(1):69–76.

Verhoef, P. (1997). *Wear of rock cutting tools implications for the site investigation of rock dredging projects.* Phd thesis, Delft University of Technology, Delft.

von den Driesch, S. (1994). Schneidtechnische und verfahrentechnische Weiterentwicklungen fur den maschinellen Vortrieb (Operational and cutting technical developments for tunneling machines). *Gluckauf-Forschunshefte*, 55:156–160.

Vutukuri, V. (1974). The effect of liquids on the tensile strength of limestone. *International Journal of Rock Mechanics and Mining Sciences*, 11:27–29.

Wang, Y., Lau, Y., and Gao, Y. (2014). Examining the mechanisms of sand creep using DEM simulations. *Granular Matter*, 16(5):733–750.

Wawersik, W. and Fairhurst, C. (1970). A study of brittle rock fracture in laboratory compression experiments. *International Journal of Rock Mechanics and Mining Sciences*, 7:561–575.

Wendland, H. (1995). Piecewise polynomial positive definite and compactly supported radial functions of minimal degree by wendland. *Advances in Computational Mathematics*, 4:389–396.

Winterwerp, J. and van Kesteren, W. (2004). *Introduction to the physics of cohesive sediment in the marine environment.* Elsevier, Amsterdam, the Netherlands.

Wong, T.-f., David, C., and Menendez, B. (2004). Mechanical compaction. In Gueguen, Y. and Bouteca, M., editors, *Mechanics of fluid saturated rocks*, pages 55–114. Elsevier Acadamic Press, Amsterdam, the Netherlands.

World Ocean Review (2014). Marine resources - opportunities and risks. Technical report.

Yamazaki, T. and Park, S. (2003). Relationships between geotechnical engineering properties and assay of seafloor massive sulfides. In *13th International Offshore and Polar Engineering Conference*, volume 5, pages 310–316, Honolulu, Hawaii, USA.

Yang, B., Jiao, Y., and Lei, S. (2006). A study on the effects of microparameters on macroproperties for specimens created by bonded particles. *Engineering Computations*, 23(6):607–631.

Yenigül, N. B. and Alvarez Grima, M. (2010). Discrete element modeling of low strength rock. *Numerical Methods in Geotechnical Engineering*, pages 207–212.

Yu, B. (2005). *Numerical simulation of continuous miner rock cutting process numerical aimulation of continuous miner rock cutting process*. Phd thesis, West Virginia University.

Zárate, F. and Oñate, E. (2015). A simple FEM–DEM technique for fracture prediction in materials and structures. *Computational Particle Mechanics*, 2(3):301–314.

Zhang, J., Ong, S., All-Bazali, T., Chenevert, M., Sharma, M., and Yi, X. (2005). Effects of Strain Rate on Failure Characteristics of Shales. In *The 40th U.S. Symposium on Rock Mechanics (USRMS): Rock Mechanics for Energy, Mineral and Infrastructure Development in the Northern regions*, number 1958, pages ARMA/USRMS 05–673.

Zhang, J., Wong, T.-F., and Davis, D. M. (1990). Micromechanics of pressure-induced grain crushing in porous rocks. *Journal of Geophysical Research*, 95(B1):341.

Zhang, X. and Wong, L. (2013). Loading Rate Effects on Cracking Behavior of Flaw-contained Specimens under Uniaxial Compression. *International Journal of Fracture*, 180:93–110.

Zhang, X. and Wong, L. (2014). Choosing a Proper Loading Rate for Bonded-Particle Model of Intact Rock. *International Journal of Fracture*, 189:163–179.

Zhao, T., Crosta, G., Utili, S., and De Blasio, F. (2017). Investigation of Rock Fragmentation during Rockfalls and Rock Avalanches via 3D Discrete Element Analyses. *Journal of Geophysical Research: Earth Surface*.

Zijsling, D. (1984). Analysis of temperature distribution and performance of polycrystalline diamond compact bits under field drilling conditions. In *SPE Annual Technical Conference and Exhibition*, Dallax, Texas, USA. Society of Petroleum Engineers.

Zijsling, D. (1987). Single cutter testing - A key for PDC bit development. In *Offshore Europe 87*, page SPE16529/1, Aberdeen, UK.

Zijsling, D. (2013). Personal communication.

Zsaki, a. M. (2009). An efficient method for packing polygonal domains with disks for 2D discrete element simulation. *Computers and Geotechnics*, 36(4):568–576.

List of Publications

Journal Publications

2. **R.L.J. Helmons, S.A. Miedema, M. Alvarez Grima, C. van Rhee**, *Modeling fluid pressure effects in cutting of saturated rock*, Engineering Geology 250 (2016), 50-60.

1. **R.L.J. Helmons, S.A. Miedema, C. van Rhee**, *Simulating hydro mechanical effects in rock deformation by combination of the discrete element method and the smoothed particle method*, International Journal of Rock Mechanics and Mining Sciences 86 (2016), 224-234.

Conferences

6. **R.L.J. Helmons, S.A. Miedema, C. van Rhee**, *Discrete element modeling of circular rock cutting with evaluation of pore pressure effects*, WODCON XXI World Dredging Conference, Innovations in Dredging, 13-17 June 2016, Miami, USA.

5. **R.L.J. Helmons, S.A. Miedema, C. van Rhee**, *Modeling the effect of water depth on rock cutting processes with the use of discrete element method*, CEDA Dredging Days 2015, 5-6 November 2015, Rotterdam, Netherlands.

4. **R.L.J. Helmons, S.A. Miedema, C. van Rhee**, *Inclusion of pore pressure effects in discrete element modeling of rock cutting*, IV International Conference on Particle-based Methods - Fundamentals and Applications, PARTICLES 2015, 28-30 september 2015, Barcelona, Spain

3. **R.L.J. Helmons, S.A. Miedema, C. van Rhee**, *A new approach to model hyperbaric rock cutting processes*, ASME 2014 International Conference on Ocean, Offshore and Arctic Engineering, OMAE 2014, 8-13 June 2014, San Francisco, USA

2. **R.L.J. Helmons, S.A. Miedema**, *Rock cutting for deep sea mining: an extension into poromechanics*, Poromechanics V: Fifth Biot Conference on Poromechancis, 10-12 July 2013, Vienna, Austria

1. **R.L.J. Helmons, S.A. Miedema**, *Cutting through hard rock-like materials, a review of the process*, WODCON XX: The art of dredging, 3-7 June 2013, Brussels, Belgium

Magazines

1. **R.L.J. Helmons, S.A. Miedema, C. van Rhee**, *Modeling the effect of water depth on rock cutting processes with the use of discrete element method*, Terra and Aqua 142, March 2016.

Awards

1. IADC Young Authors Award 2015

Curriculum Vitæ

Rudolfus Lambertus Jacobus Helmons

27-04-1987	Born in Halsteren, the Netherlands.

Education

1998-2005	Secondary School Regionale Scholengemeenschap RSG 't Rijks, Bergen op Zoom
2005-2010	BSc, Mechanical Engineering
2009-2011	MSc, Mechanical Engineering Track: Thermo-Fluids Engineering *with great appreciation* Eindhoven University of Technology
2012-2017	PhD, Offshore and Dredging Engineering Delft University of Technology
Thesis:	Excavation of Hard Deposits and Rocks - on the cutting of saturated rock
Promotor:	Prof. dr. ir. C. van Rhee
Co-promotor:	Dr. ir. S. A. Miedema

Work Experience

2011-2017	Research Engineer, IHC MTI (Royal IHC)
2017	Researcher, Delft University of Technology

Acknowledgements

Ben je net lekker op dreef met je afstuderen, beginnen je begeleiders ineens (onafhankelijk van elkaar) of promoveren niet iets is voor na het afstuderen. Dit terwijl bij mij altijd het idee leefde om na de studie direct de industrie in te gaan. Het feit dat je dit proefschrift nu al in de hand hebt laat zien dat het toch anders is gelopen dan vooraf gedacht.

De grens tussen (academisch) onderzoek en de industrie heeft me altijd blijven boeien. In de tijd dat ik afstudeerde ging het erg goed met de baggersector, waardoor vrijwel direct bij mijn aanstelling als R&D Engineer bij toen nog MTI Holland (nu IHC MTI) zich de kans voor deed om voor IHC een promotieonderzoek uit te voeren. Ik ben dan ook Henk van Muijen en Robert van de Ketterij dankbaar dat zij dit vanuit IHC zo snel mogelijk maakten.

Een van de projecten waar IHC aan deel nam was het onderzoek naar het snijden van gesteente op grote waterdieptes. Een project dat vooral mijn aandacht trok door zijn toepassing voor o.a. diepzeemijnbouw en zijn combinatie in zowel de bagger, olie en gasindustrie.

Veel dank gaat uit naar mijn begeleiders Cees van Rhee en Sape Miedema. Cees, als prof heb je het altijd druk, maar de deur stond altijd open. Wanneer ik ergens op vast liep kon ik altijd bij even aankloppen om mij op weg te helpen, soms waren enkele suggesties voldoende, soms met uitgebreidere discussies. Sape, ook bij jou kon ik altijd langslopen om even wat te vragen, vaak waren enkele suggesties voldoende, maar liep het toch uit op een uitgebreidere discussie, al dan niet vakinhoudelijk. Ik ben ook erg blij dat ik samen met jou les heb mogen geven in Vietnam. Naast de unieke ervaring heb ik je op een heel andere manier leren kennen. Het was een erg leuke tijd.

Joep, ik leerde je kennen tijdens mijn afstuderen, toen als begeleider. Niet wetende dat we later als collega's en de laatste jaren ook als kamergenoot verder zouden gaan. Door de jaren heen heb ik veel gehad aan de vele discussies, zowel voor het onderzoek, andere werkzaamheden als alle heerlijk onzinnige onderwerpen. Xiuhan, both our projects were on the same topic. It really helped me a lot to be able to discuss up to every little detail in our projects. Zeker ook de andere collega's in de vakgroep hebben erg veel geholpen bij het gemotiveerd blijven voor het onderzoek. Met name de goede sfeer, wat zeker ook is terug te zien in de vele (on)zinnige discussies bij de koffie-automaat. Ik heb ook veel genoten van de gezamenlijke congresbezoeken en de aansluitende reizen. Kortom, ook Arno, Bas, Dave, Ershad, Frans, Geert, Jort, Rik en Thijs en de inmiddels voormalige collega-promovendi Lynyrd en Ralph, bedankt allemaal.

Verder wil ik de collega's vanuit de industrie bedanken. Met name Ronald, Michel, Djurre, Rihard, Mario, Robert, Rick, Roeland en alle anderen die namens de deelnemende bedrijven hebben bijgedragen aan het tot stand komen van dit onderzoek en het sturen naar de gekozen aanpak.

Naast de vakinhoudelijke steun heb ik ook veel medeleven ervaren van familie en vrienden. Mannen van 't 51e, ik heb alle jaren enorm genoten van de chill-weekenden. Het is een heerlijke traditie geworden, ik hoop dat we die nog vele jaren door kunnen zetten.

Ik wil vooral ook Corine bedanken. Ik weet dat ik het je de afgelopen jaren niet altijd gemakkelijk heb gemaakt. Maar je hebt me in al die jaren altijd gesteund. Tot slot, dit

alles zou niet mogelijk geweest zijn door de steun van mijn ouders om te gaan studeren en tegelijkertijd iets te doen wat ik leuk vind. Helaas hebben zij dit niet meer mee kunnen maken, maar ik ben er enorm trots op, hoewel het niet altijd makkelijk is geweest, dat zij mij tijdens mijn eerste 18/19 levensjaren hebben geholpen te worden tot wie ik nu ben.